Colourful Depth

Adaptive Optics and Spectral Unmixing for Single-Molecule Localization Microscopy

Marijn Siemons

Colourful Depth

Adaptive Optics and Spectral Unmixing for Single-Molecule Localization Microscopy

Keywords: Single-molecule localization microscope, adaptive optics, multi-colour imaging

Printed by: Print Service Ede

Front & Back: "Colordepth at a single-molecule level" by Marijn Siemons

This work originates as part of the research programme of the Foundation for Fundamental Research on Matter (FOM), and falls as of 1 April 2017, under the responsibility of Foundation for Nederlandse Wetenschappelijk Onderzoek Instituten (NWO-I), which is part of the Dutch Research Council (NWO).

ISBN/EAN 978-90-832301-8-4

Colourful Depth

Adaptive Optics and Spectral Unmixing for
Single-Molecule Localization Microscopy

Kleurrijke Diepte

Adaptieve Optica en Spectrale Ontmenging voor
Lokalisatiemicroscopie
(met een samenvatting in het Nederlands)

Proefschrift

ter verkrijging van de graad van doctor
aan de Universiteit Utrecht
op gezag van de rector magnificus, prof. dr. H.R.B.M. Kummeling,
ingevolge het besluit van het college voor promoties
in het openbaar te verdedigen op

woensdag 1 juni 2022
des middags te 16:15 uur

door

Marijn Ewout Siemons

geboren op 15 november 1992
te Enschede

Dit proefschrift is goedgekeurd door de

promotor: prof. dr. L.C. Kapitein
copromotor: prof. dr. M.H.P. Kole

Dit proefschrift werd mede mogelijk gemaakt met financiële steun van Nederlandse Organisatie voor Wetenschappelijk Onderzoek (NWO).

I am among those who think that science has great beauty.

Marie Curie

Contents

1

Introduction

1

1.1 The quest for resolving smaller structures

The cell is the fundamental unit of life. Its structure and organization shape the functionality of the tissue or the organism comprised by cells. This organization is in turn defined by the biological interactions inside the cell. While these interaction, in principle, originate from chemistry, and ultimately from the physical rules of our universe, the complex molecular pathways are emergent phenomena that cannot be derived from first principles. Therefore, research in cell biology uses an array of molecular tools combined with microscopy to unravel and understand cellular organization and function.

1.1.1 The size of the cell

In order to appreciate the scale modern microscopes can resolve, it is useful to relate the sizes of various cellular components. A typical cell is about 10 to 100 μm large [1], which is about the size of the width of a hair (roughly the smallest feature you can see with the naked eye). Inside a cell, there is a nucleus that contains the genetic material, which has a size of about 5 μm. Large organelles, such as the Golgi apparatus, Endoplasmic Reticulum (ER) and mitochondria can range from 500 nm to 5 μm and smaller organelles such as lysosomes and endosomes can range from 50 nm to 500 nm. Proteins, the main machinery of the cell, range from sizes of a few nanometres to hundreds of nanometres, often in complexes where these proteins function together, such as the motor dimer kinesin [2].

A cellular structure that will often be featured in this thesis is the microtubule network. Microtubules are a component of the cytoskeleton and provide the structure and shape of eukaryotic cells [1]. These hollow tubular polymers have a width of 25 nm [3] and play a critical part in many cellular processes, such as cell division, and provide the platform for intracellular transport by kinesins and other transport proteins [2].

1.1.2 Fluorescence microscopy

An important tool to visualize and label these proteins is fluorescence light microscopy [4]. In fluorescence microscopy specific proteins are tagged with a fluorescent molecule. Fluorescent molecules are molecules that can be excited using light. Due to energy losses these molecules re-emit the light with a lower energy, resulting in a colour shift. Because of this colour shift, the emission can be filtered from the excitation using dichroic mirrors and colour filters and imaged onto a camera (see Figure 1.2). The most famous of fluorophores is the well-named Green Fluorescent Protein (GFP) [5]. This fluorophore can be excited using blue light and emits green light that can be seen by eye.

Most cellular components are not fluorescent and need to be labelled. For live-cell imaging, a fluorescent protein (such as GFP) can be fused to the protein of interest using genetical tools. Another staining strategy is to use immunostaining with primary and secondary antibodies. This allows the target protein to be stained with chemical fluorophores such as AlexaFluor-647. These chemical (non-protein) fluorophores are brighter, more stable and can be spectrally tuned resulting in a large family of fluorophores with different excitation and emission spectra [6].

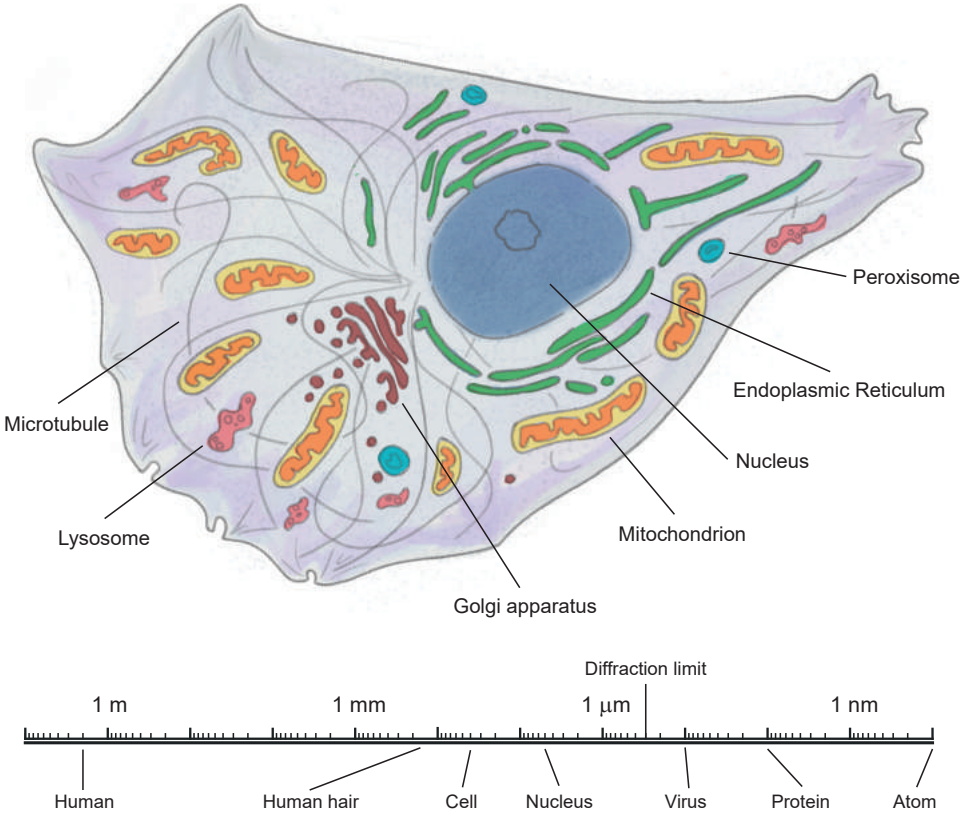

Figure 1.1: Illustration of a cellular architecture of an animal cell and an overview of characteristic size of several biological components and other relatable objects. Credit: Merle Koertshuis.

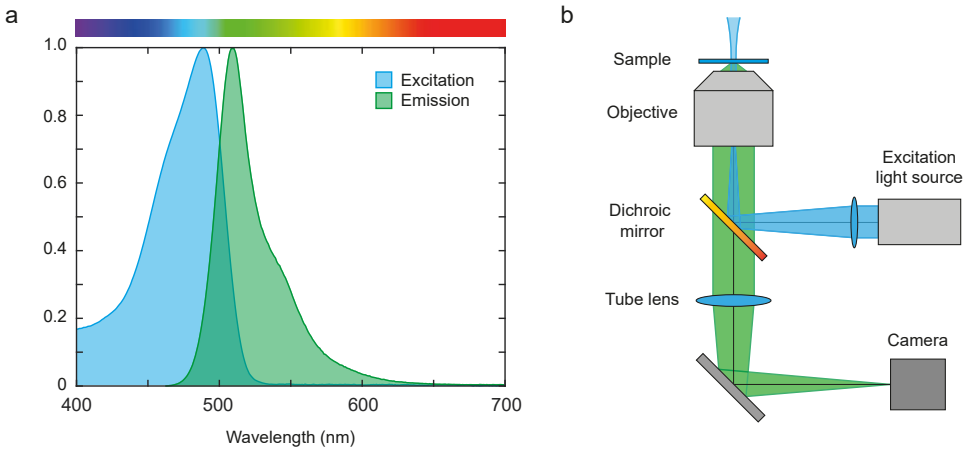

Figure 1.2: a) Normalized excitation and emission spectra of GFP. The colourbar indicates the colour of the associated wavelength. b) Illustration of a regular fluorescent microscope. The sample is illuminated by a light source. The collected fluorescence is filtered from the excitation light via a dichroic mirror and imaged on a camera.

There are two main advantages of using fluorescence microscopy over electron microscopy (EM). Firstly, live-cell imaging is only possible with light microscopy because EM requires a vacuum to image. Secondly, EM visualizes (mainly) electron density and therefore lacks contrast specificity, especially for weakly contrasting molecules such as microtubules or actin filaments. The cell is densely-packed with organelles, other sub-cellular compartments and freely diffusing proteins [1]. Image interpretation is therefore more challenging in EM because everything is visualized [7]. Fluorescence labelling allows researchers to look just at the proteins of interest and is therefore molecule-specific. Although the invention of fluorescence microscopy has brought cellular research to new levels, the main draw-back of light microscopy compared to EM is its resolution, the ability to identify closely spaced objects as separate entities.

1.1.3 Image formation and the diffraction limit

When light interacts with an object, the electromagnetic wave diffracts in all directions. Smaller structures diffract in larger angles, while coarse structures diffract only in a narrow cone, see Figure 1.3. The complex diffraction pattern collected by the microscope corresponds to the features present in the sample. If the diffracted light is not collected with a sufficiently large angle by the objective, the spatial information of the corresponding feature size is lost. This is reflected in the Point Spread Function (PSF). This function describes what the image of an infinitesimal small point source would be on the camera or eye and has a finite size [8]. The Optical Transfer Function (OTF) is the Fourier counterpart of the PSF and describes how each spatial frequency is attenuated by the optical system (see Figure 1.4b).

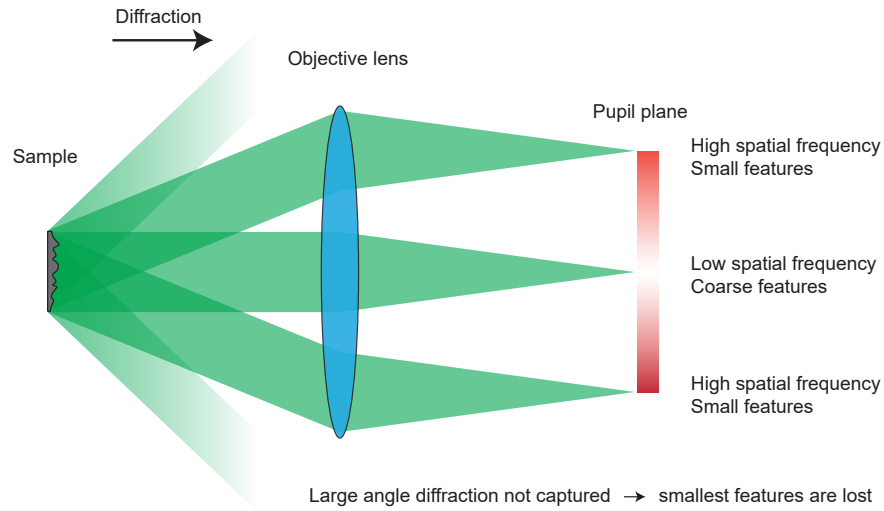

Figure 1.3: The light emitted, reflected or transmitted by a sample diffracts when travelling towards the objective lens. Coarse features diffract the light into small angles and small features diffract the light into large angles. If the objective has a sufficiently large collection angle, determined by the NA of the objective, the features can be imaged on a camera (not shown here). If not, the information on these (smaller) sized features is lost. This directly limits the feature size that can be resolved by the microscope and thereby determines the resolution of the microscope. A non-periodic sample will diffract the light in a continuous range of angles (not shown here).

This directly limits the spatial information that can be collected from a sample to

$$d = \frac{\lambda}{2n\sin(\theta)} = \frac{\lambda}{2\mathrm{NA}} \tag{1.1}$$

with d the smallest feature that can be resolved by the microscope, λ the wavelength of the light, n the refractive index of the sample, θ the largest collection angle of the objective and $\mathrm{NA} = n\sin(\theta)$ the Numerical Aperture of the objective. This limit, called the diffraction limit, was originally proposed by Ernst Abbé and has been the foundation of optical imaging theory, governing the performance of optical instrumentation [8]. An alternative resolution measure is the resolving power of the microscope; its ability to separate points of an object as distinct, called the Rayleigh criterion. When two points are too close to each other, the PSFs will overlap and cannot be disentangled anymore (see Figure 1.4a). The PSF is a central concept in single-molecule localization microscopy and in this thesis.

1.2 Single-molecule localization microscopy

The diffraction limit holds when all objects emit light of the same wavelengths at the same time. Controlling the activity of the fluorophores in time, space and wavelength provides ways to circumvent the diffraction limit and improve resolution. In the early years of this century a variety of techniques were developed

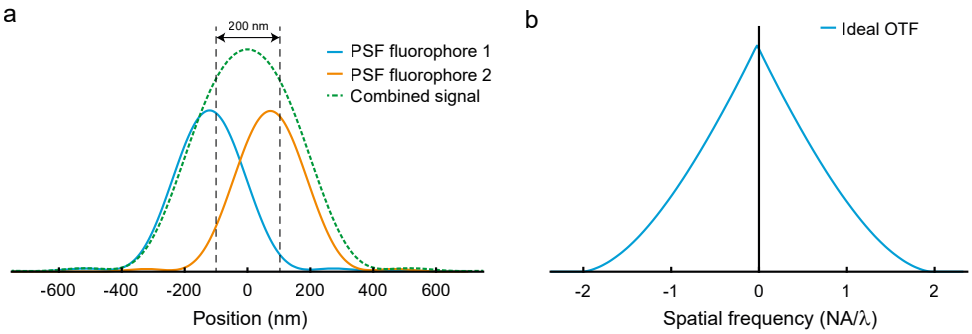

Figure 1.4: a) The Point Spread Function (PSF) describes how a single point source is imaged by the optical system. If two point sources are placed too close, the PSFs overlap and cannot be disentangled anymore. b) The Optical Transfer Function describes how the spatial frequency content of the sample is attenuated. In fluorescence microscopy the largest transmitted spatial frequency is 2 NA/λ, which corresponds to a feature size of $\lambda/2$ NA.

that achieve this by controlling how the fluorophores are activated, excited and deactivated. These techniques include Structured Illumination Microscopy (SIM) [9], Stimulated Excitation Depletion (STED) [10] and a range of techniques collectively called Single-Molecule Localization Microscopy (SMLM)[11–14]. Here, we focus on the latter.

Single-molecule localization microscopy circumvents the diffraction limit by collecting multiple acquisitions, where each frame only a sub-set of fluorophores is emitting photons (see Figure 1.5b). The location of the fluorophores can be estimated from its spot on the camera with a precision Δx of approximately

$$\Delta x \approx \frac{\lambda}{2\mathrm{NA}\sqrt{N_{\mathrm{ph}}}} \tag{1.2}$$

with N_{ph} the number of photons the fluorophore emitted. This typically results in a localization precision between 5 and 20 nm. After localizing thousands or millions of emitters it is possible to reconstruct a so-called super-resolution image where each localization is rendered as a small spot, typically the size of the estimated localization precision.

SMLM is able to circumvent the diffraction limit by creating sparsity: the signal of each blinking event originates from a single molecule and does not overlap with the signal from other emitting molecules. There are a variety of ways (with exciting acronyms) to create this required sparsity such as (f)PALM, STORM, *d*STORM and DNA-PAINT [11–15]. Interestingly, Dickson et al. had already shown in 1997 that GFP undergoes repeated cycles of fluorescent emission, called 'blinking' [16]. The current most widely used technique is *d*STORM (direct STOchastic Reconstruction Microscopy). In *d*STORM the fluorophores, typically Alexa-647, are actively 'pumped' to a so-called 'off-state' by a laser with a power of around 5 kW/cm^2. Some fluorophores will then randomly transition to the 'on-state'. Once in the 'on-state', the fluorophore is repeatedly excited and emits about a 1000 photons

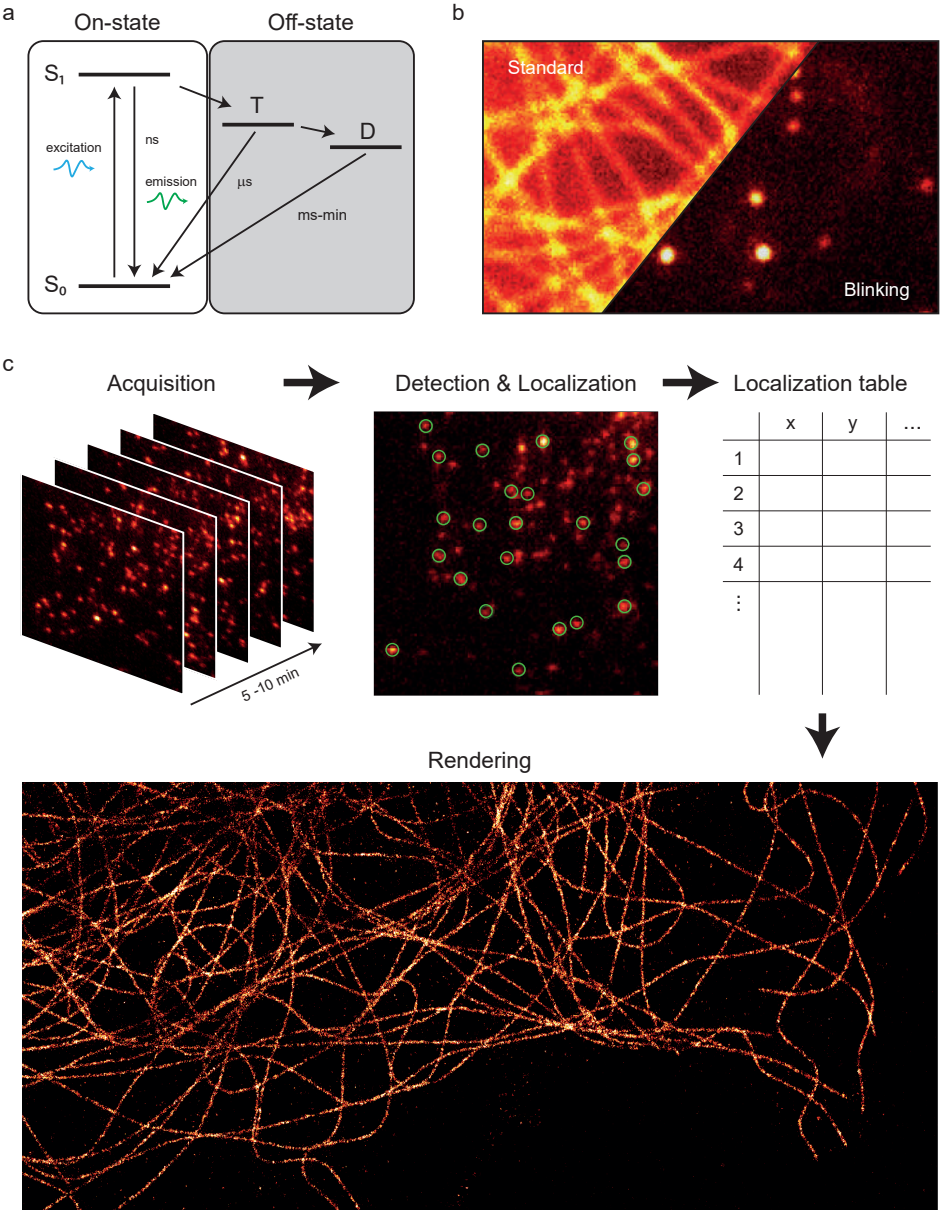

Figure 1.5: Principle of single-molecule localization microscopy. a) Simplified Jablonski diagram showing molecular states essential to *d*STORM. S_0 and S_1 are the ground and excited singlet state of a fluorophore . From the excited state the molecule can transition to the ground state by emitting a photon or transition to the triplet state (T) and a prolonged dark-state (D) induced by a reducing agent in the imaging buffer. Adapted from [17]. b) Example acquisition of a standard widefield image and an acquisition with blinking molecules. c) Workflow of single-molecule localization microscopy. A series of frame are acquired where different subsets of fluorophores are emitting. These spots can then be localized by a fitting procedure. The positions of these spots are used to reconstruct an image that contains more detail than the diffraction limited image.

in roughly 30 ms, see Figure 1.5a. The fluorophore will then again transition to the 'off-state' and either be photo-damaged (bleached) or again transition to the 'on-state'. By introducing a reducing agent in the imaging buffer, the time a fluoropore spends in the 'off-state' can be prolonged, which creates the necessary sparsity. The bleaching can be reduced by removing oxygen from the imaging buffer [17]. In this way, many fluorophores can be separately imaged and localized. In order to detect and localize sufficient fluorophores typically around 10.000 frames are acquired, containing about 1 million blinking events in total.

The rapid adaption of these super-resolution microscope techniques resulted in the inventors Eric Betzig, Stefan W. Hell and W.E. Moerner to be awarded the Nobel prize in Chemistry "for the development of super-resolved fluorescence microscopy" only 14 years (STED) and 7 years (SMLM) after their invention. An important biological discovery that was made using these techniques in cell biological research is the discovery of actin rings inside neurons (now called the membrane periodic scaffold or MPS) [18, 19]. This scaffolding structure has a periodicity of 180 nm, just below the diffraction limit, and had not been observed before.

Although these advances greatly impacted the type of questions that could be answered with light microscopy, these techniques are mostly limited to image cultured cells. Here cells are seeded on thin coverslips, where they flatten to only a few μm thick. While such a model system allows for a large range of complex assays, it fails to capture the surrounding context that is present in real tissue or organisms, which contain other supporting cell types and infer different mechanical stresses. In order to understand complex organs such as the brain all levels of complexity, ranging from macro cellular organization to protein nanoscale organization, have to be understood. There is therefore a need for super-resolution techniques that can be used to image deep in tissue. Sample-induced optical aberrations are a major factor prohibiting SMLM in tissue [21].

1.3 Sample-induced optical aberrations

In an ideal case, the electromagnetic wave emitted by a single molecule is a spherical wave, which is in turn collected by the objective and transformed into a plane wave. This is then focussed by a second lens onto the camera. However, when light travels through an in-homogeneous medium, such as tissue, the local differences in refractive index cause the wave to locally retard, resulting in a distorted wavefront called an aberration (see Figure 1.8a). When this wave is focused onto the camera, it results in a distorted PSF. An aberrated PSF has a lower contrast than the ideal PSF (see Figure 1.8b) and therefore the performance of the microscope is reduced. In the case of SMLM, single molecules become more difficult to detect and localize due to the decrease in contrast [22].

The distortion of the wavefront can be viewed as a circular hill landscape, with coarse features like peaks and troughs, and small features like boulders and grass. Frits Zernike, inventor of the phase contrast microscopy, came up with a set of polynomial functions (now called Zernike polynomials, see Figure 1.7) that can efficiently describe optical aberrations. First, certain polynomials are associated with specific misalignment aberrations such as coma. Second, they are mathematically

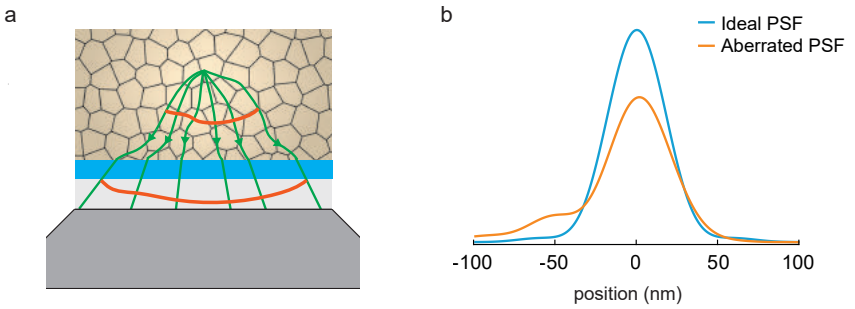

Figure 1.6: a) Local refractive index changes distort the wavefront of an emitter, called an aberration. b) When the wave-front is aberrated the PSF reduces in contrast and can become asymmetric. This aberrated PSF contains of 72 mλ of astigmatism and coma. c) The first 21 Zernike polynomials, ordered vertically by radial degree and horizontally by azimuthal degree.

orthogonal and complete over the unit circle; that is to say, an infinite set of coefficients can uniquely describe any distortion. Finally, the shape of these functions becomes increasingly complex, which allows aberrations to be effectively described with a limited number of coefficients, while still capturing the most important features of the distortion.

These distorted wave-fronts or optical aberrations can arise from the equipment itself, such as misaligned optics, or can be induced by the sample [23]. These sample-induced aberration are particularity challenging as these are sample specific. A way to overcome these aberrations is the use of adaptive optics.

1.4 Adaptive optics

Adaptive Optics (AO) is an overarching term for the technique to sense and correct wavefront distortions using optomechanical components that can actively change shape or their effect on light. This is typically a Spatial light Modulator (SLM) or Deformable Mirror (DM) [24, 25]. AO was originally developed for astronomy observatories to correct for the wave-front distortions induced by the atmosphere. The most advanced telescope currently under development is the European Extremely Large Telescope (ELT), which has two deformable mirrors. Its main mirror consist of 798 hexagonal segments that can all be individually positioned. In microscopy, AO can be used to correct the sample-induced aberrations in the excitation path for point-scanning modalities such as confocal [26] or 2-Photon microscopy [27, 28]. In the case for SMLM, a deformable mirror can be placed in the emission path of the microscope to restore the PSF (see Figure 1.8c).

The most challenging part of AO in microscopy is to unravel the precise aberration. When capturing an image with a camera the information of the phase of the light - the aberration - is lost. Wave-front detectors are specific devices that can measure the wave-front either directly using interference or by measuring the local slope with a Shack-Hartmann sensor. Both these methods require a point light source to measure the wave-front. In astronomy this is called a 'guide star', which

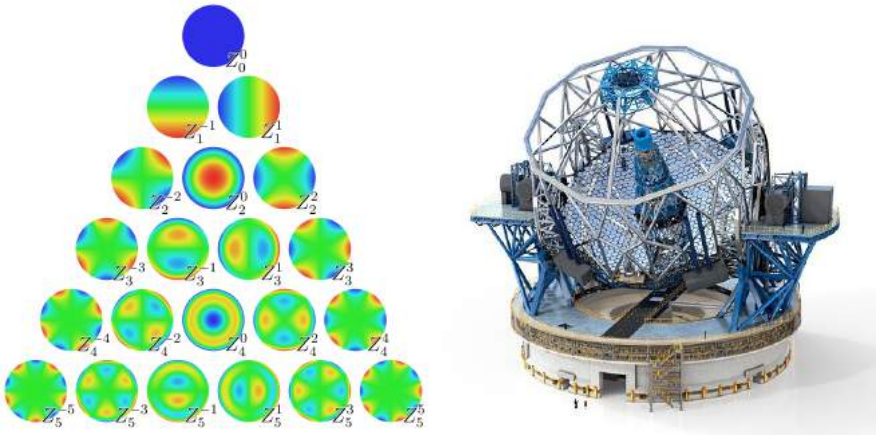

Figure 1.7: Left: The first 21 Zernike polynomials, ordered vertically by radial degree and horizontally by azimuthal degree. Right: Artist rendering of the European Extremely Large Telescope (ELT). Credit: ESO/Dorling Kindersley.

can be created by using a laser to create a plasma sphere high in the atmosphere. In microscopy one can use fiducial markers, small fluorescent beads, as guide stars, but in most cases it is impossible to position such a marker at the place of interest inside the sample. Therefore, AO in microscopy often uses intensity-based AO [25]. Here one tries to iteratively optimize the shape of the mirror based on the images captured by the camera. This is fundamentally a (smart) trial and error game. For this to work one needs a metric to optimize, a value derived from the image, and an optimization algorithm that tries to estimate the next best correction based on the previous image(s). As one might expect, this is particularly difficult in SMLM because the images change rapidly every camera frame and have a significant amount of noise.

1.5 Outline of this thesis

In this thesis I address a number of important challenges for single-molecule localization microscopy. I developed a novel methodology to image inside tissue with Adaptive Optics and an improved implementation for multi-colour imaging and I analysed axial accuracy in 3D localization.

A current major limiting aspect of SMLM is that it can only be used on thin samples while imaging close to the coverslip. When imaging deeper inside samples (>10 μm) the refractive index mismatch between the sample and the immersion oil will introduce aberrations that hampers imaging. In **Chapter 2** I demonstrate the use and benefits of using AO to correct these aberrations and compare the performance of an oil immersion objective in combination with AO with the use of a water immersion objective without AO. Importantly, I show that, when using a cylindrical lens for 3D localization in combination with oil immersion, there is a dramatic loss of ellipticity that disrupts 3D localization. Simulations reveal that this is caused

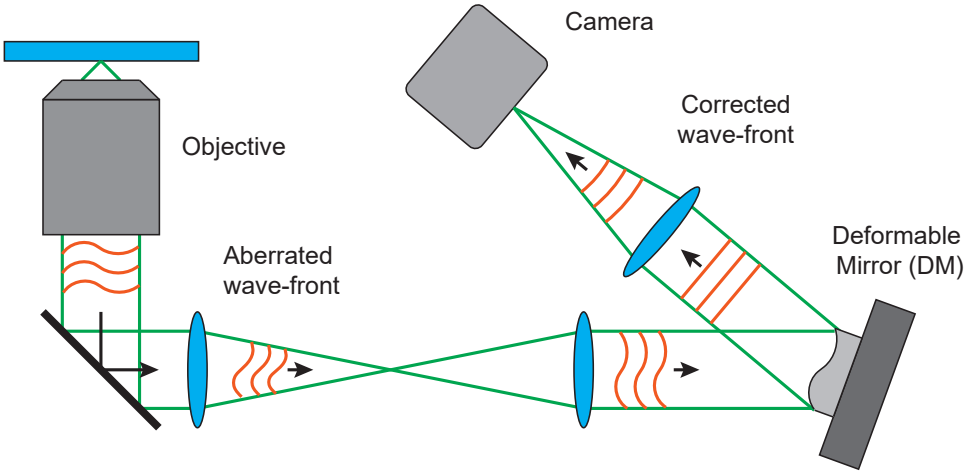

Figure 1.8: The aberrated wave-front can be corrected by placing a deformable mirror in the emission port of the microscope using Adaptive Optics. If the aberration is known, the mirror can restore the wave-front and thereby the PSF.

by higher order spherical aberration and I demonstrate that this loss in ellipticity can be overcome by adaptively change the astigmatism level.

While in Chapter 2 we use a fiducial marker to correct the wave-front distortions, this is not feasible in tissue. There is therefore a need for a robust methodology to perform AO with SMLM in tissue, without using a fiducial marker. A solution is to use the acquisitions of the blinking molecules themself. This is particularly challenging because the single-molecule acquisitions contain large amounts of noise. In **Chapter 3** I present a novel robust AO algorithm for SMLM termed REALM (Robust and Effective Adaptive optics in Localization Microscopy). I demonstrate its improvements over previously proposed methods experimentally and with simulations. Lastly, I use this method to perform SMLM in rat brain slices and resolve the membrane periodic scaffold at depths up to 50 μm.

For many biological questions the relative localization or distribution between two or more proteins is of importance, which requires a multi-colour SMLM modality. This is challenging because fluorophores that are best suitable for *d*STORM are spectrally very similar and cannot be easily disentangled. Recently a new method for multi-colour SMLM was demonstrated on a 4Pi microscope called 'Salvaged Fluoresence'. In **Chapter 4** I present an improved implementation of this method that can be implemented on conventional microscopes and is experimentally easy to setup and maintain. I furthermore propose a novel classification algorithm that uses statistical decision theory and compare the classification performance of this new method to existing classification methods.

Axial localization accuracy is an important, but understudied aspect in SMLM. In **Chapter 5** I explore the effects of Super-Critical Angle Fluorescence (SAF) on the z-accuracy when performing 3D SMLM with PSF engineering near the coverslip. I show that there is a difference between the PSF obtained with stage-movement

and the true PSF exhibited by the fluorophores. These simulations reveal that this leads to large axial biases. These differences are caused by depth-dependent pupil apodization due to SAF and the refractive mismatch between the mounting medium inside the sample and the immersion oil. In chapter 5 I explore how these effects affect the z-accuracy for a collection of engineered PSFs and I propose how these predictions can be experimentally verified and how these biases can be corrected.

Finally, **Chapter 6** concludes and summarizes the work presented in this thesis and provides closing remarks and an outlook for future research and developments.

References

[1] B. Alberts, *Essential cell biology*, 2nd ed. (Garland Science Pub., New York, NY, 2004) pp. xxi, 740, 102 p.

[2] L. C. Kapitein and C. C. Hoogenraad, *Building the neuronal microtubule cytoskeleton,* Neuron **87**, 492 (2015).

[3] A. Akhmanova and M. O. Steinmetz, *Tracking the ends: a dynamic protein network controls the fate of microtubule tips,* Nat Rev Mol Cell Biol **9**, 309 (2008).

[4] U. Kubitscheck, *Fluorescence microscopy : from principles to biological applications*, second edition. ed., p. 1 online resource (507 pages).

[5] F. G. Prendergast and K. G. Mann, *Chemical and physical properties of aequorin and the green fluorescent protein isolated from aequorea forskalea,* Biochemistry **17**, 3448 (1978).

[6] N. Panchuk-Voloshina, R. P. Haugland, J. Bishop-Stewart, M. K. Bhalgat, P. J. Millard, F. Mao, W. Y. Leung, and R. P. Haugland, *Alexa dyes, a series of new fluorescent dyes that yield exceptionally bright, photostable conjugates,* J Histochem Cytochem **47**, 1179 (1999).

[7] L. Heinrich, D. Bennett, D. Ackerman, W. Park, J. Bogovic, N. Eckstein, A. Petruncio, J. Clements, S. Pang, C. S. Xu, J. Funke, W. Korff, H. F. Hess, J. Lippincott-Schwartz, S. Saalfeld, A. V. Weigel, and C. P. Team, *Whole-cell organelle segmentation in volume electron microscopy,* Nature **599**, 141 (2021).

[8] J. W. Goodman, *Introduction to Fourier optics*, 3rd ed. (Roberts & Co., Englewood, Colo., 2005) pp. xviii, 491 p.

[9] M. G. Gustafsson, *Nonlinear structured-illumination microscopy: wide-field fluorescence imaging with theoretically unlimited resolution,* Proc Natl Acad Sci U S A **102**, 13081 (2005).

[10] S. W. Hell and J. Wichmann, *Breaking the diffraction resolution limit by stimulated emission: stimulated-emission-depletion fluorescence microscopy,* Opt Lett **19**, 780 (1994).

[11] E. Betzig, G. H. Patterson, R. Sougrat, O. W. Lindwasser, S. Olenych, J. S. Bonifacino, M. W. Davidson, J. Lippincott-Schwartz, and H. F. Hess, *Imaging intracellular fluorescent proteins at nanometer resolution,* Science **313**, 1642 (2006).

[12] S. T. Hess, T. P. Girirajan, and M. D. Mason, *Ultra-high resolution imaging by fluorescence photoactivation localization microscopy,* Biophys J **91**, 4258 (2006).

[13] M. J. Rust, M. Bates, and X. Zhuang, *Sub-diffraction-limit imaging by stochastic optical reconstruction microscopy (storm),* Nat Methods **3**, 793 (2006).

[14] R. Jungmann, M. S. Avendano, J. B. Woehrstein, M. Dai, W. M. Shih, and P. Yin, *Multiplexed 3d cellular super-resolution imaging with dna-paint and exchange-paint,* Nat Methods **11**, 313 (2014).

[15] U. Endesfelder and M. Heilemann, *Direct stochastic optical reconstruction microscopy (dstorm),* Methods Mol Biol **1251**, 263 (2015).

[16] R. M. Dickson, A. B. Cubitt, R. Y. Tsien, and W. E. Moerner, *On/off blinking and switching behaviour of single molecules of green fluorescent protein,* Nature **388**, 355 (1997).

[17] L. Nahidiazar, A. V. Agronskaia, J. Broertjes, B. van den Broek, and K. Jalink, *Optimizing imaging conditions for demanding multi-color super resolution localization microscopy,* PLoS One **11**, e0158884 (2016).

[18] K. Xu, G. Zhong, and X. Zhuang, *Actin, spectrin, and associated proteins form a periodic cytoskeletal structure in axons,* Science **339**, 452 (2013).

[19] C. Leterrier, J. Potier, G. Caillol, C. Debarnot, F. Rueda Boroni, and B. Dargent, *Nanoscale architecture of the axon initial segment reveals an organized and robust scaffold,* Cell Rep **13**, 2781 (2015).

[20] D. E. Koser, A. J. Thompson, S. K. Foster, A. Dwivedy, E. K. Pillai, G. K. Sheridan, H. Svoboda, M. Viana, L. D. Costa, J. Guck, C. E. Holt, and K. Franze, *Mechanosensing is critical for axon growth in the developing brain,* Nat Neurosci **19**, 1592 (2016).

[21] S. Liu, H. Huh, S. H. Lee, and F. Huang, *Three-dimensional single-molecule localization microscopy in whole-cell and tissue specimens,* Annu Rev Biomed Eng **22**, 155 (2020).

[22] B. C. Coles, S. E. Webb, N. Schwartz, D. J. Rolfe, M. Martin-Fernandez, and V. Lo Schiavo, *Characterisation of the effects of optical aberrations in single molecule techniques,* Biomed Opt Express **7**, 1755 (2016).

[23] M. Schwertner, M. Booth, and T. Wilson, *Characterizing specimen induced aberrations for high na adaptive optical microscopy,* Opt Express **12**, 6540 (2004).

[24] R. K. Tyson, *Principles of adaptive optics* (Academic Press, Boston, 1991) pp. xii, 298 p.

[25] M. Booth, D. Andrade, D. Burke, B. Patton, and M. Zurauskas, *Aberrations and adaptive optics in super-resolution microscopy,* Microscopy (Oxf) **64**, 251 (2015).

[26] M. J. Booth, M. A. Neil, R. Juskaitis, and T. Wilson, *Adaptive aberration correction in a confocal microscope,* Proc Natl Acad Sci U S A **99**, 5788 (2002).

[27] M. A. Neil, R. Juskaitis, M. J. Booth, T. Wilson, T. Tanaka, and S. Kawata, *Adaptive aberration correction in a two-photon microscope,* J Microsc **200 (Pt 2)**, 105 (2000).

[28] P. Marsh, D. Burns, and J. Girkin, *Practical implementation of adaptive optics in multiphoton microscopy,* Opt Express **11**, 1123 (2003).

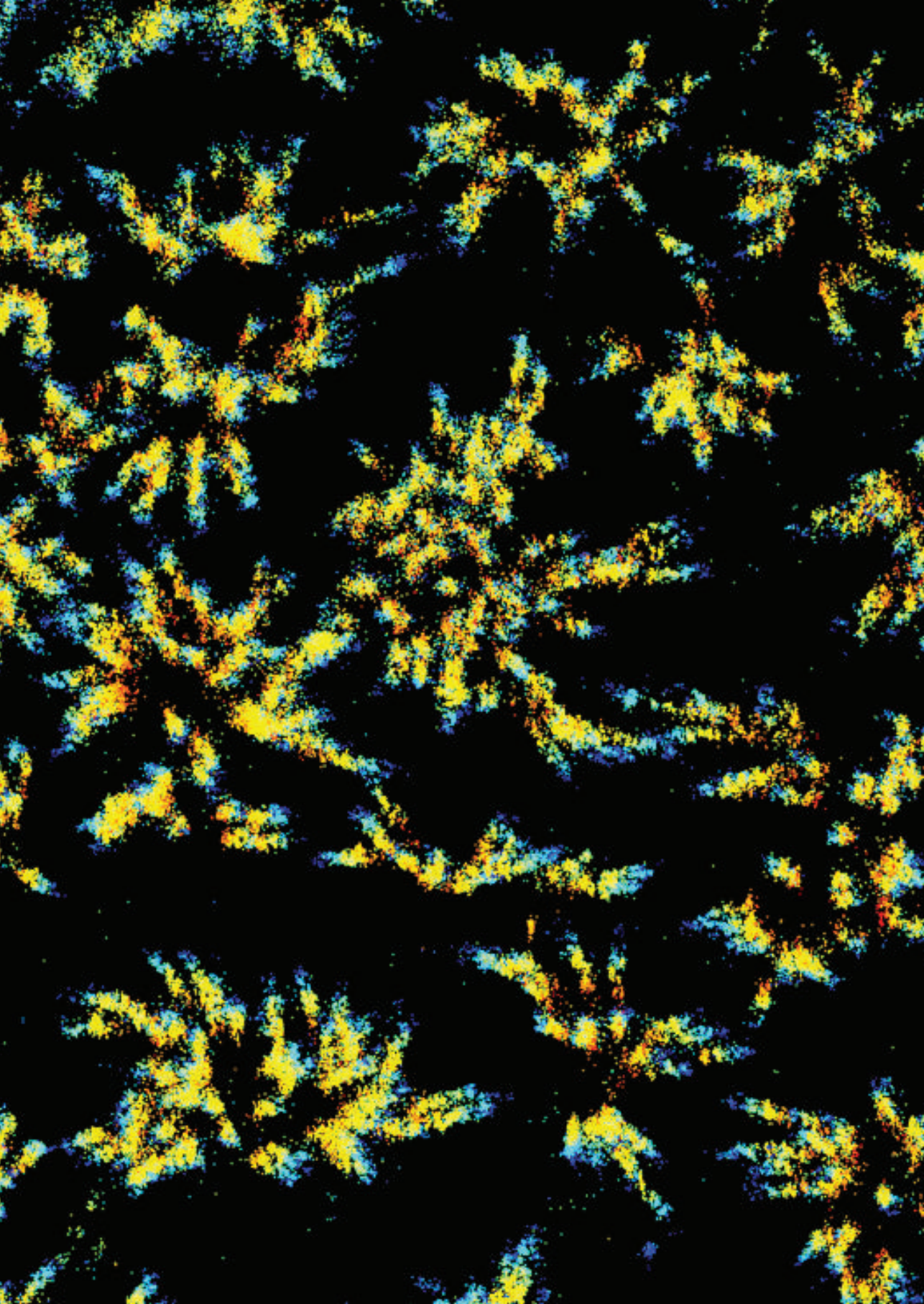

2

Comparing strategies for deep astigmatism-based single-molecule localization microscopy

Single-molecule localization microscopy enables fluorescent microscopy with nanometric resolution. While localizing molecules close to the coverslip is relatively straightforward using high numerical aperture (NA) oil immersion (OI) objectives, optical aberrations impede SMLM deeper in watery samples. Adaptive optics (AO) with a deformable mirror (DM) can be used to correct such aberrations and to induce precise levels of astigmatism to encode the z-position of molecules. Alternatively, the use of water immersion (WI) objectives might be sufficient to limit the most dominant aberrations. Here we compare SMLM at various depths using either WI or OI with or without AO. In addition, we compare the performance of a cylindrical lens and a DM for astigmatism-based z-encoding. We find that OI combined with adaptive optics improves localization precision beyond the performance of WI-based imaging and enables deep (>10 μm) 3D localization.

This chapter has been published in Biomed. Opt. Express **11**, 735-751 (2020) [1].

2.1 Introduction

In Single-Molecule Localization Microscopy (SMLM) the diffraction limit is circumvented by analyzing the Point Spread-Function (PSF) of single fluorescent molecules to obtain precise information about the molecule's position in x and y [2, 3]. Subsequent localization of large numbers of fluorophores provides structural information with a resolution in the order of nanometers [4]. A common way to determine the z-position of fluorophores is by inducing astigmatism in the detection path, either by introducing a cylindrical lens (CL) [5] or an adaptive optical element [6]. Inducing astigmatism creates slightly separate focal planes for the x- and y-direction, with the average focal plane (AFP) situated halfway in between them. The PSF of a fluorophore positioned in the AFP appears round, while the PSFs of fluorophores outside AFP appear elliptical. The orientation of the major and minor axis of an elliptical PSF indicates whether a fluorophore is positioned above or below the AFP and the distance to the AFP can be determined from the amount of ellipticity.

When imaging deeper into a sample, aberrations induced by both the optical setup and the sample distort the PSF and will decrease the localization precision [7, 8]. Sources of setup-induced aberrations are for instance imperfections in the objective, other lenses and dichroic mirrors. High NA oil immersion (OI) objectives, often used for SMLM, provide optimal imaging close to the coverslip, but focusing deeper into a water-based sample results in large, mainly spherical aberrations because of the mismatch in refractive index between the immersion oil ($\sim$1.52) and the sample ($\sim$1.33). The use of water immersion (WI) objectives limits this mismatch at the expense of a lower NA and, as a result, lower photon counts and a decreased resolution [9]. Deeper imaging also increases the distance light has to travel through the sample, increasing scattering and refraction of the fluorescence emission due to inhomogeneities in the sample [8].

Aberrations induced by both setup and sample can be corrected using an adaptive optical element, such as a liquid crystal-based spatial light modulator (SLM) or a deformable mirror (DM) [10]. In SMLM applications, DMs are preferred because they reflect >95% of the incoming light and are not sensitive to the polarization of the light, implying less photon loss compared to SLMs. Since in SMLM the excitation pattern is not critical, implementing a DM in the detection path only is sufficient. In addition, a DM can also be used to induce a tunable amount of astigmatism for 3D-SMLM [6]. Previous work has shown that correction of system-induced aberrations and the simultaneous induction of astigmatism using a DM can result in high-quality 3D-SMLM images of structures close to the coverslip [6]. Additionally, it was shown that the amount of induced astigmatism influences the x-, y- and z-precision [11], but the settings for optimal x-, y-, and z-resolution have not been systematically explored.

Correction of setup- and sample-induced aberrations becomes more important when imaging deeper into a sample, especially when using an OI objective. At a depth of 6 μm in cultured COS-7 cells, correction of aberrations resulted in improved 2D and 3D-SMLM as measured in amount of localizations and degree of structure reconstruction [10]. Despite this evidence that DM-based adaptive optics

can improve 2D- and 3D-SMLM when imaging deeper into a biological sample, a thorough investigation of the effect of aberration correction on SMLM performance as function of imaging depth is lacking. Furthermore it has been reported that with OI the astigmatic z-encoding is impaired due to the refractive index mismatch [12–14]. It is unclear whether the use of an OI objective in combination with AO outperforms a WI objective where there is very little or no refractive index mismatch. Lastly, a comparison of astigmatism-based 3D-SMLM using either AO or a CL as function of imaging depth has not been reported. Here we first explored how localization precision as a function of imaging depth in 2D-SMLM is affected by DM-based aberration correction in combination with an OI objective. These results were compared with the performance of a 60x WI objective without active aberration correction. Secondly, astigmatism-based PSF z-encoding as a function of imaging depth was compared between a CL and a DM and the field distortion and astigmatic field dependency were assessed for both techniques. Thirdly, we experimentally addressed the optimal value of induced astigmatism to achieve the highest x-, y- and z-localization precisions and compared this to the theoretical optimum. Finally, we performed 3D-SMLM using a DM to correct aberrations and induce astigmatism and succeeded in super-resolved imaging at high imaging depth in a biological sample.

2.2 Materials and methods

2.2.1 Setup

SMLM microscopy was performed on a Nikon Ti-E microscope equipped with a 100x Apo TIRF OI objective (NA. 1.49), a 60x Plan Apo IR WI objective (NA 1.27), and Perfect Focus System 3, shown in Figure 2.1a. Excitation was achieved with a mercury lamp or via a custom illumination pathway with a Lighthub-6 (Omicron) containing a 638 nm laser (BrixX 500 mW multimode, Omicron), a 488nm laser (Luxx 200 mW, Omicron), and a 405 nm laser (Luxx 60 mW, Omicron). Emission light was separated from excitation light with a quad-band polychroic mirror (ZT405/488/561/640rpc, Chroma), a quad-band emission filter (ZET405/488/561 /640m, Chroma), and an additional single-band emission filter (ET525/50m for green emission and ET655lp for far-red emission, Chroma). Fluorescence was detected via either a pathway containing a removable Nikon CL (left port), or a pathway containing the MicAO™ 3D adaptive optics system (right port, Imagine Optic, France, www.imagine-optic.com). The latter pathway uses a relay system of two lenses with equal focal length the front focal plane onto the sCMOS camera (Hamamatsu Flash 4.0v2). A third lens (L1) was placed in the intermediate image plane, which together with the tube lens and L2, conjugate the back focal plane of the objective to a DM (MIRAO 52-e, Imagine Optic). A removable mirror was used to optionally deflect the light to a Shack-Hartmann wave-front sensor (HASO3, Imagine Optic). The camera had an effective pixel size of 65 nm (100x objective) or 108 nm (60x objective) and the camera output was converted to photons using the calibration factor supplied by the manufacturer. Samples were positioned in the x- and y-direction with an M-687 PILine stage (PI) and in the z-direction with either the

Perfect Focus System or a P-736 PInano stage (PI). The DM and wave-front sensor were controlled by Imagine Optic software, all other components by Micromanager [15].

Aberrations were corrected using the image-based 3N algorithm [16] as implemented in the Imagine Optic software, with maximum contrast as optimization metric. In short, per Zernike mode three images of a 100 nm fluorescent bead were acquired with a zero, negative, and positive amplitude bias of that Zernike mode applied to the DM. The optimization metric is measured in the three images and a second-order polynomial fit is used to determine the amount of applied Zernike mode corresponding to the maximum of the metric. This is done per Zernike mode, and the sum of Zernike modes with corresponding amplitudes is subsequently applied to the mirror to correct aberrations. The amplitude of the Zernike coefficients are reported in nm RMS. This RMS unit describes the RMS displacement of the mirror surface with respect to a flat surface, integrated over the whole mirror.

For SMLM, the sample was continuously illuminated with 638 nm light. In addition, the sample was illuminated with 405 nm light at increasing intensity to keep the number of fluorophores in the fluorescent state constant. Typically 5,000 frames for in vitro microtubules and 10,000 frames for Caco2-cells were recorded per acquisition with exposure times of 30-40 ms.

2.2.2 Collection efficiency correction for comparing objectives

The WI and OI objectives have different magnifications, a different NA and a different transmission efficiency. This results in different excitation intensities as well as different collection efficiencies, which both affect the localization precision. In order to compensate for these differences, we aimed to compare the localization precisions of both objectives given a similar number of emitted photons. First, we calculated a transmission correction for the collected number of photons, which included the transmission of the objectives, the reflectance at the cover glass, and the transmission/reflection efficiencies of the CL or AO-module. First, we address the transmission at the cover glass, for which two factors are important: The Fresnel coefficients at the medium/coverslip interface and the coverslip/immersion interface and the NA of the objective lens. The energy transmission for randomly polarized light at an interface 1→2 is given by [17]

$$T_{1\to 2} = \frac{1}{2}\frac{n_2\cos(\theta_2)}{n_1\cos(\theta_1)} \times \left[\left(\frac{2n_1\cos(\theta_1)}{n_2\cos(\theta_2)+n_1\cos(\theta_1)}\right)^2 + \left(\frac{2n_2\cos(\theta_1)}{n_1\cos(\theta_2)+n_2\cos(\theta_1)}\right)^2\right] \quad (2.1)$$

with n_1 and n_2 the refractive indices on either side of the interface and θ_1 and θ_2 the respective angles of the light with respect to the interface. The first term is due to wave-front compression and the second term contains the Fresnel coefficients for S- and P-polarized light. From this equation, the ratio of the collection efficiency for a

point emitter of the OI and WI objective can be calculated as

$$\frac{\mathrm{CE_{OI}}}{\mathrm{CE_{WI}}} = \frac{\int_{\phi=0}^{2\pi}\int_{\theta=0}^{1.329} T_{\mathrm{w}\to\mathrm{g}}\sin(\theta)d\theta d\phi)}{\int_{\phi=0}^{2\pi}\int_{\theta=0}^{1.27} T_{\mathrm{w}\to\mathrm{g}}T_{\mathrm{g}\to\mathrm{w}}\sin(\theta)d\theta d\phi)} \tag{2.2}$$

with $\theta_{1.329}$ and $\theta_{1.27}$ the angles corresponding a NA of 1.329 (88°) and 1.27 (73°) and where we assumed there is no refractive index mismatch between the glass and oil. The largest angle the OI objective collects light is 1.33, as deeper than 1 μm the super-critical angle fluorescence (SAF) can be ignored. In practice this effective NA is slightly reduced as the 90° collection angle can only be achieved at the coverslip. We estimated from the working distance and the size of the front lens that at a depth of 30 μm the largest collection angle is 88°, corresponding to a NA of 1.329. This calculation revealed that the CE of the OI objective lens is 139% the efficiency of the WI objective. This is slightly more than if one would only consider the solid angle and ignore the Fresnel coefficients: $(1-\cos(\theta_{1.329}))/(1-\cos(\theta_{1.27})) = 137\%$.

The transmission efficiencies of the objectives itself are listed as 83% (WI) and 78% (OI) in their specifications for light with a wavelength of 690 nm. Lastly, we estimate the transmission of the CL and AO-module, where we assumed all optics have the appropriate coating (99.5% transmission/reflection per interface) and are not damaged. Based on two interfaces, the CL-module has an estimated transmission of 99% when in bypass mode. The AO-module consists of 3 lenses and 4 broadband mirrors. The DM itself has a silver coating with a reflectance of 98% at 15 degree incidence. These results in a total transmission of 93% for the AO-module.

All these efficiencies add up to a total efficiency of 78% for WI + CL and 95% for OI + AO compared to OI + CL. As expected OI collects significantly more light compared to WI, but the loss in the AO-module should be taken into account as well. These efficiency factors enabled us to compare the achieved localization precision between the different strategies, OI + CL, WI + CL and OI + AO, in a consistent manner.

2.2.3 In vitro imaging of fluorescent beads and microtubules

HiLyte™ Fluor 647 labeled microtubules (MTs) were prepared from stabilized seeds as described earlier [18] and stored at -80°C. HiLyte™ Fluor 647 (HF647)-tubulin was purchased from Cytoskeleton. Before sample preparation seeds were kept at 37°C for 2-4 h and stabilized by 1% glutaraldehyde. Agarose gel was prepared by adding 4% agarose (A9539, Sigma Aldrich) to 100 mM Tris at pH 8. MT seeds and 100 nm green fluorescent beads (final dilution 1/2000; F8803, ThermoFisher) were added to heated agarose, gently mixed, and put on a microscope slide between two pieces of double sided tape. For SMLM, mercaptoethylamine and an oxygen scavenging system consisting of glucose, glucose oxidase and catalase were additionally added to the heated agarose (final concentrations: 50 mM MEA, 5% w/v glucose, 560 μg/ml glucose oxidase, 40 μg/ml catalase). A coverslip was pressed onto the tape and the sample was cooled under running water to quickly solidify the agarose.

When focusing into a water-based sample with an OI objective, the imaging

depth has to be corrected for the refractive index mismatch. The imaging depths for data obtained with the OI objective are reported as 0.93 $n_{\text{water}}/n_{\text{oil}} z_{\text{stage}}$ where the factor 0.93 is obtained from simulations with a PSF model similar to [19].

Single molecule localization precisions at z-stage positions of 0, 5, 10, 20 and 30 μm were determined using the previously described ImageJ plugin Detection of Molecules (DoM, available at) [20]. The detection size of the PSF was set to 110% of the ideal PSF ($\lambda/2$NA) and spots where the width deviated more than 30% from the detection size where disregarded as false positives. The total localization precision was calculated as $\sigma_{tot} = \sqrt{\sigma_x^2 + \sigma_y^2}$. In all cases, the reported localization precisions (or errors of other fitting parameters θ) were estimated using the covariance matrix C of the least-squared fitting

$$\sigma_{\theta_k}^2 = \frac{\chi^2}{(n-p)C_{kk}} \tag{2.3}$$

with χ^2 the chi-squared value, n the number of data points (pixels) and p the number of fit-parameters. Localizations with an uncertainty above 50 nm were discarded. Mean localization precision were calculated from three acquisitions per depth.

2.2.4 Comparison of 3D calibration curves

Calibration curves were obtained by making z-stacks with 20 nm steps of 100 nm green fluorescent beads suspended in the agarose gel. For each z-step, the x-width and y-width of the PSF (as determined from a Gaussian fit using DoM) were subtracted and plotted against the z-position. PSF x- and y-width was taken as the full width half maximum (FWHM) value, equal to $2\sqrt{2\ln 2}$ of the Gaussian's standard deviation (spread). Calibration curves were measured at imaging depths of 0.0, 0.8, 3.2, 8.1, and 16.2 μm (OI) and 0.0, 5.0, 10, 15, and 20 μm (WI). Astigmatism was induced with the CL or the DM. The amount of astigmatism induced with the DM was increased with increasing imaging depth, from 60 nm RMS at the coverslip to 120 nm RMS at a depth of 16.2 μm, to obtain similar calibration curves.

2.2.5 Comparison of field-of-view distortion

A small sample volume was created by attaching a coverslip to a microscope slide using double-sided tape. 100 nm green fluorescent beads were diluted in PBS (1/100,000) and incubated for 10 minutes in the sample volume to allow non-specific adsorption. Free beads were then washed away with PBS and the volume sealed with vacuum grease.

An image was made of beads within the field of view of the camera with and without astigmatism using the CL, and at another position using AO (0 and 60 nm RMS astigmatism). To assess the distortion of the field-of-view, a custom MATLAB-script was used that for each particle in the image without astigmatism finds the highest-intensity particle in the image with astigmatism within a certain area around the first. Based on a first assessment of positional shift, this area was set to be an ellipse with longer y-axis to account for the mostly y-shifted positions. Ellipse radii

of 0.67 pixels in x and 6.7 pixels in y were used for CL images, and of 1.0 pixels in x and 3.2 pixels in y for AO images. First, the global translation was determined and subtracted from the individual shifts to account for non-ideal alignment. Then, the leftover positional shifts were decomposed in the x- and the y-direction. To produce the graph in Figure 2.4d, shifts in the y-direction were averaged over particles with positions within a 50 pixel windows in the y-direction in the images without astigmatism. After removal of shifts more than 2 times the standard deviation from the mean, the mean and standard deviation were recalculated to produce the graph in Figure 2.4d. In total 522 and 501 shifts were used for CL and AO, respectively.

2.2.6 Comparison of field-dependent aberrations

The field-dependency of the aberrations and induced astigmatism (Figure 2.5) was assessed by taking a through focus scan (TFS) of a bead and performing a phase-retrieval algorithm on this TFS [21]. The bead was then moved in a 11x11 grid over a 32x32 μm field of view, taking a TFS at each point. The phase retrieval algorithm fits Zernike coefficients up the sixth radial order $Z_6^{\pm 6}$ (23 orders in total). This was performed for the OI lens either on the left port with and without CL and for the right port with AO (0 and 100 nm RMS astigmatism).

2.2.7 Tuning of astigmatism

For Figure 2.6, samples with green fluorescent beads on a coverslip were prepared as described above, with a bead dilution of 1/50,000. z-stacks were made with 50 nm steps with an astigmatism that varied between 10 and 100 nm RMS with steps of 10 nm, induced with the DM. PSF widths were determined using DoM. The offset between the x-focal plane and the y-focal plane was determined from 3rd order polynomial fits to the bottom part (x- and y-width < 8 pixels) of the curves of x- and y-width as function of the z-position of the stage. The focal plane offset was calculated by dividing the difference in z-position between the minima of the two fits by two. The focal plane offset was determined for different amounts of induced astigmatism and for each setting a linear fit to the z-position of the stage versus the difference between x-width and y-width resulted in a slope α, which was used to calculate the z-position of localized particles based on their PSF widths. The uncertainties in the z-position were calculated using error propagation:

$$\sigma_z = \sqrt{\alpha^2(\sigma^2_{x-\text{width}} + \sigma^2_{y-\text{width}})} \tag{2.4}$$

where α is the slope of the calibration curve and $\sigma_{x/y}$-width the error in determining the x- and y-widths, as determined from the Gaussian fits.

2.2.8 Experimental localization precision and CRLB calculation

The experimental localization precision was measured by acquiring 25 frames of a fluorescent bead at a certain z-position. The standard deviation of the estimated position is a measure of the achieved localization precision, assuming there is no drift during the 25 frames. To achieve a signal to noise ratio representative for a single molecule the camera integration time and the bright-field illumination were

tuned to achieve around 50 background photons per pixel and 8000 signal photons.

The Cramér-Rao Lower Bound (CRLB) was obtained from a vectorial PSF model [22]. This model implements the effect of the high NA and includes the NA, pixel size, wavelength, refractive indices of the immersion oil, the cover glass and the surrounding medium of the bead and the size of the bead. Lastly the read noise from the camera was implemented as well.

The required background photon levels for the CRLB computation were estimated from the estimated background level by DoM. To estimate the signal photon count, we used a through-focus scan with 100 ms exposure time, followed by phase retrieval. The relevant signal photon count was then calculated as the ratio of the experimental (3 ms) and through-focus exposure time (100 ms).

2.2.9 SMLM imaging of Caco2-BBE cells

Caco2-BBE cells (a gift from S.C.D. van IJzendoorn, University Medical Center Groningen, The Netherlands) were maintained in DMEM supplemented with 9% FBS, 50 μg/μl penicillin/streptomycin and 2 mM L-glutamine. For immunofluorescent imaging, cells were seeded on 18 mm coverslips at a density of 1 x 105/cm2 and cultured for 10-12 days to allow for spontaneous polarization and brush border formation. Cells were fixed with 4% paraformaldehyde in PBS for 10 min, washed with PBS, permeabilized with 0.5% Triton x-100 in PBS for 15 min and blocked with 3% BSA in PBS for at least 1 h. Cells were incubated with primary antibodies, either Mouse-anti-Ezrin (610602; BD Biosciences; 1 μg/ml) or Mouse-anti-Villin (610358; BD Biosciences; 1 μg/ml), for 6 h at room temperature, washed with PBS, incubated with secondary antibodies, Goat-anti-mouse Alexa 647 (A21236; Life Technologies; 6.7 μg/ml), for an additional hour at room temperature and washed with PBS. SMLM imaging was performed in the same buffer as the SMLM imaging of *in-vitro* MTs.

2.3 Results and discussions

2.3.1 Comparison of localization precision

To examine the effect of a DM on localization precision in OI-based single-molecule localization microscopy, we embedded HF647-labeled microtubules and fluorescent beads in an agarose gel. After optimizing the DM shape using the fluorescent beads before each acquisition, we compared localization precision with and without adaptive optics at imaging depth between 0-30 μm. In addition, we used a WI objective to measure localization precision in the absence of a refractive index mismatch.

When using WI, we found that the histogram of localization precisions did not change when imaging deeper into the sample, indicating that the imaging quality was not degraded (Figure 2.1b). In contrast, with OI the localization precision gradually degraded when imaging deeper (Figure 2.1c). Close to the cover slip, localization precision was better than with WI, likely due to the super-critical angle fluorescence which is captured by the high NA objective. When we used AO, the loss in localization precision at greater depth was prevented to a high degree (Figure

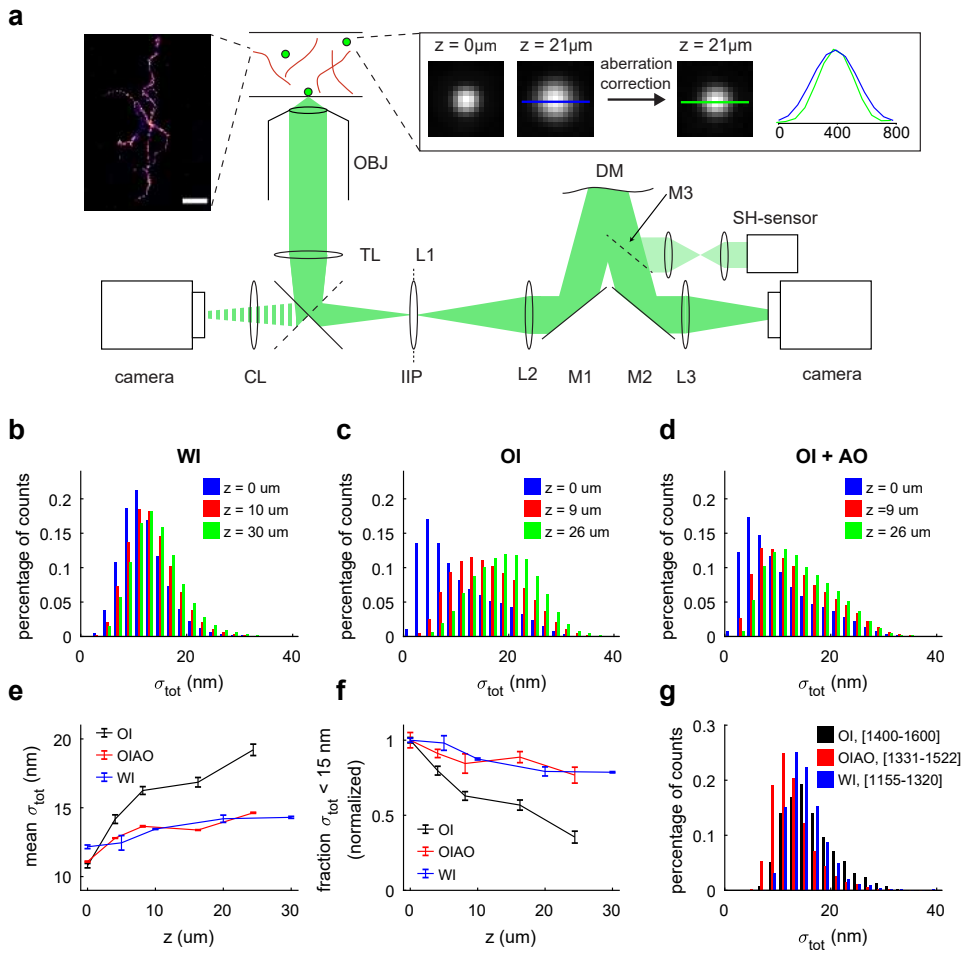

Figure 2.1: Use of Adaptive optics improves 2D SMLM away from the coverslip. (a) Schematic representation of the imaging setup. Fluorescence from the sample, consisting of green fluorescent beads and stabilized HiLyte647-conjugated microtubules suspended in agarose gel, is collected via a water immersion (WI) or oil immersion (OI) objective and projected on a camera either directly (left side; optionally through a CL) or via a DM (two mirrors in the AO-module are not shown). Left inset shows a representative SMLM reconstruction of the HiLyte647-MTs, scalebar is 1 μm. Right inset shows images and cross sections of a fluorescent bead at the coverslip (left panel) and at 25 μm depth without (middle panel) and with aberration correction (right panel). Cross sections at the drawn lines are shown on the right. (b,c,d) Localization distribution for different imaging depths for the WI objective lens (b), OI (c) and OI with adaptive optics (d). (e) The normalized fraction of estimated localization precisions below 15 nm as function of depth. (f) The average estimated localization precision as function of depth for WI and OI with and without adaptive optics. (g) Histogram of localization precision for integrated photons counts between 1400 and 1600. This interval is corrected for transmission efficiencies of the WI objective and the AO-module. Data collection parameters are indicated in Table 1.

Table 2.1: . Number of experimental repeats and molecules used in Figure 2.1

OI without AO		
depth(μm)	N	n (sum of N acquisitions)
0	3	32497
4.4	3	118441
8.8	3	37805
17.6	3	65834
25.5	3	22870
OI with AO		
depth(μm)	N	n (sum of N acquisitions)
0	3	41294
4.4	3	74233
8.8	3	48012
17.6	2	61730
25.5	3	91253
WI		
depth(μm)	N	n (sum of N acquisitions)
0	1	29809
5	3	43961
10	3	45739
20	3	42408
30	3	41546

2.1d). Often in reconstructing SMLM images localizations with a precision above a certain threshold are discarded, which makes the fraction of localizations below this threshold an important parameter for achieving proper reconstructions. Figure 2.1e shows that the fraction of localizations with a precision below 15 nm does not decreases significantly for the WI or OI with adaptive optics, but decreases rapidly without correction for the OI. Moreover, AO improves the average localization precision by a factor of 1.3 at a depth of 26 μm and doubles the fraction of localizations below 15 nm (Figure 2.1f). This increase in localization precision is mostly due to the differences in PSF shape, rather than a strong increase in detected photons, because even for events with the same amount of estimated photons the localization precision with correction is highly improved (Figure 2.1g).

Because WI has a lower collection efficiency than OI+AO (see methods), we compared the localization precision for fluorophores for which the emitted photons were estimated to be similar. That is, fluorophores detected with OI with photon counts between 1400-1600 per frame were compared with fluorophores in the range of 1331-1522 and 1088-1244 for OI+AO and WI, respectively (Figure 2.1g). This analysis revealed that WI outperformed OI, while OI + AO outperformed WI in achieved localization precision for the same amount of estimated emitted photons. For the photon counts mentioned above, the fraction of localizations with an estimated precision below 15 nm was 63% for WI, 46% for OI and 76% for OI + AO. Moreover, the median of localization precision was improved by 14% (13.9 nm for WI and 12.0 nm for OI + AO). Thus, OI + AO outperforms WI because a larger fraction of the emitted photons can be collected.

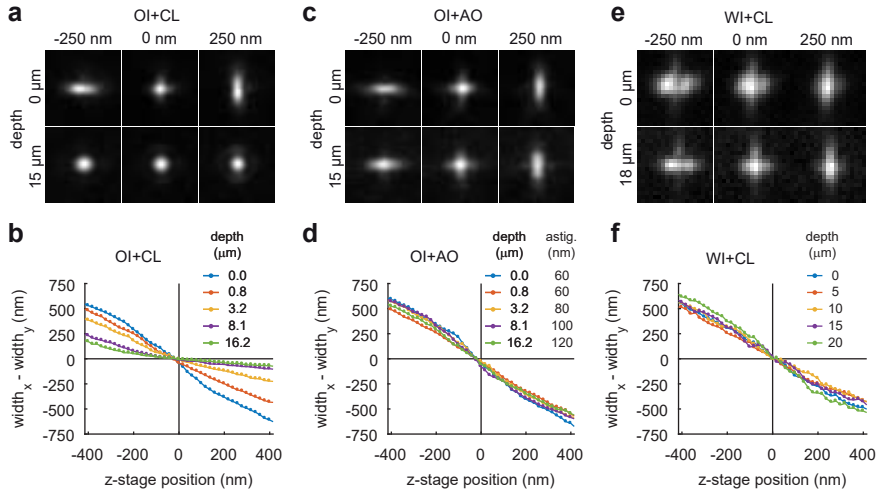

Figure 2.2: Adaptive optics allow z-encoding away from the coverslip. (a) PSF with astigmatism of a 100 nm green fluorescent bead in agarose gel on the coverslip (top panels) and at 18 μm depth (bottom panels) at stage z-positions of -250, 0 and 250 nm with respect to the focal plane of the OI objective. Astigmatism was induced with the CL. (b) Curves of the difference between PSF x-width and y-width as function of the z-stage position with respect to the objective focal plane, at increasing distance from the coverslip for the 100X OI objective. (c,d) Same as (a) and (b) but adaptive optics was used to both correct aberrations and induce astigmatism. (e,f) Same as A and B, but imaged with the 60x WI objective. The size of the ROI is 2 x 2 μm in all images.

2.3.2 The depth-depended ellipticity-loss

Next, we compared the use of either a CL or a DM to induce astigmatism for z-localization at different imaging depth. When using OI, the PSF of fluorescent beads close to the coverslip (depth < 5 μm) showed clear ellipticity after insertion of the CL. At larger imaging depth, however, the PSF remained largely symmetric and could not be used to encode the z-position (Figure 2.2a). This is reflected in the calibration curves obtained by plotting the difference in PSF width in the x and y direction as a function of z-position (Figure 2.2b).

Similarly, even after optimizing the DM to correct for the first order spherical aberration, the degree of astigmatism sufficient for z-encoding near the coverslip did not induce strong ellipticity at larger imaging depth. Nevertheless, more astigmatism could easily be added, resulting in consistent ellipticity and corresponding calibration curves at depths up to 18 μm (Figure 2.2c&d). When the WI objective was used in combination with the cylindrical length, the induced ellipticity was less pronounced (Figure 2.2c). Although the calibration curve appears similar to the ones obtained with OI and remains unaltered for depths from 0-20 μm (Figure 2.2f), the PSF for the WI with cylindrical lens was not well represented by a 2D Gaussian. This indicates that this specific cylindrical lens is not a suitable for this WI objective.

The requirement for increased levels of astigmatism for z-encoding at increased depth with OI objectives has been reported previously [13], but the origins of this

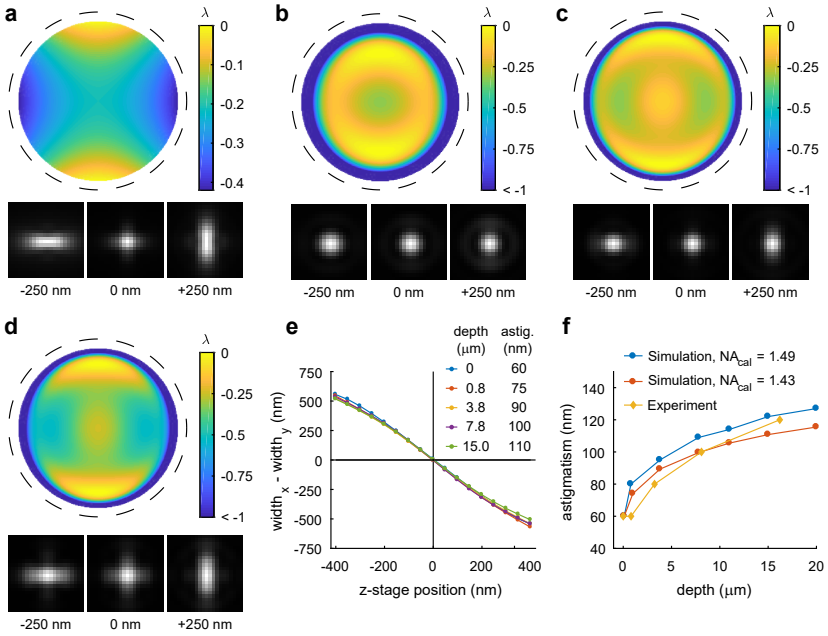

Figure 2.3: Simulation study on the depth depended loss of astigmatism. a) Aberration profile with 60 nm astigmatism at the coverslip and corresponding PSF at different z-positions. The dashed line indicates the NA of the objective (1.49). b-d) The aberration profile without AO (b) and with AO(c&d) with 60 nm (c) and 120 nm (d) astigmatism at a depth of 15 um. e) Simulated calibration curves at different depths with AO. Even with AO, more astigmatism needs to be added in order to maintain a similar curve. f) Optimal amount of astigmatism as function of depth for different calibration NAs and alongside the experimental values.

effect had remained unclear. To investigate this, we performed simulations to simulate PSFs at different depths for OI with and without AO. We placed an emitter at 15 μm from the coverslip and performed AO by simulating a 3N correction algorithm to correct primary spherical aberration (Z_4^0). As correcting spherical aberration results in a focus shift, the primary spherical aberration was corrected iteratively by 3N correction and refocusing by stage movement until convergence (similar to the experiments). After correction of the primary spherical aberration astigmatism was added and a PSF is computed. The amount of astigmatism was then optimized to regain a calibration curve with the same slope as the curve obtained at the coverslip (Figure 2.3a).

The simulated PSFs at the coverslip and at a depth of 15 μm were qualitatively strikingly similar to the experimental ones (Figure 2.3b). Inspection of the corresponding wave-fronts revealed that, at a depth of 15 μm, the applied astigmatism is 'drowned' in the spherical aberration caused by the refractive index mismatch. However, even with AO to correct the first-order spherical aberration, applying 60 nm of astigmatism did not result in the required ellipticity (Figure 2.3e). This was caused by the significant amount of higher-order spherical aberrations (Z_6^0,

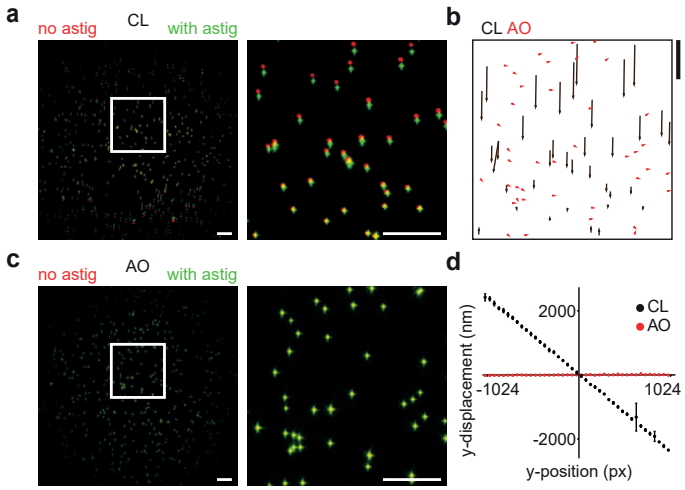

Figure 2.4: . Inducing astigmatism with AO does not distort the field of view. (a) Overlayed images of green fluorescent beads without (red) and with (green) CL inserted in the optical path (left) and a zoom of the region in the white box (right). Scalebar is 10 μm. (b) Displacement of bead locations when astigmatism is induced with the CL (black arrows) and with adaptive optics (red arrows). Scalebar for shifts is 1 μm. (c) Overlayed images of green fluorescent beads without (red) and with (green) astigmatism induced with the DM (left) and a zoom of the region in the white box (right). Scalebar is 10 μm. (d) Graph showing y-displacement when astigmatism is induced using the CL (black) and adaptive optics (red) as function of y-position with respect to the center of the field of view.

Z_8^0, etc.), as the wave-front was still significantly aberrated at the edge of the pupil. Similar to the experimental results (Figure 2.2b), we could obtain the desired calibration curve by introducing more astigmatism (Figure 2.3d&e).

The optimal amount of astigmatism obtained from the simulations deviated slightly from the amount of astigmatism that was required experimentally (Figure 2.3f). We found that the theoretical amount of astigmatism was dependent on the (calibration) NA. When calibrating the DM with a Shack-Hartman sensor it is likely that the spots at the edge of the pupil are not detected, which effectively reduces the calibration NA. We therefore repeated our simulation with an NA of 1.43 instead of 1.49, which corresponds to a calibration in which per row/column one spot is not detected by the Shack-Hartman sensor. It is worth noting that the effective NA (the maximum angle at which fluorescence is collected) is 1.33 in both cases due to the refractive index mismatch. The calibration NA only determines the pupil-size at which the Zernike modes are defined and normalized.

The predicted amount of astigmatism for a calibration NA of 1.43 matches well with the experiments (Figure 2.3f). The remaining discrepancy near the coverslip is likely due to hysteresis in the mirror or suboptimal correction of primary spherical aberration. Altogether, these results demonstrate that the remaining, non-corrected higher-order spherical aberrations are the major reason for the loss in ellipticity when imaging deeper into a watery sample with a constant amount of astigmatism applied.

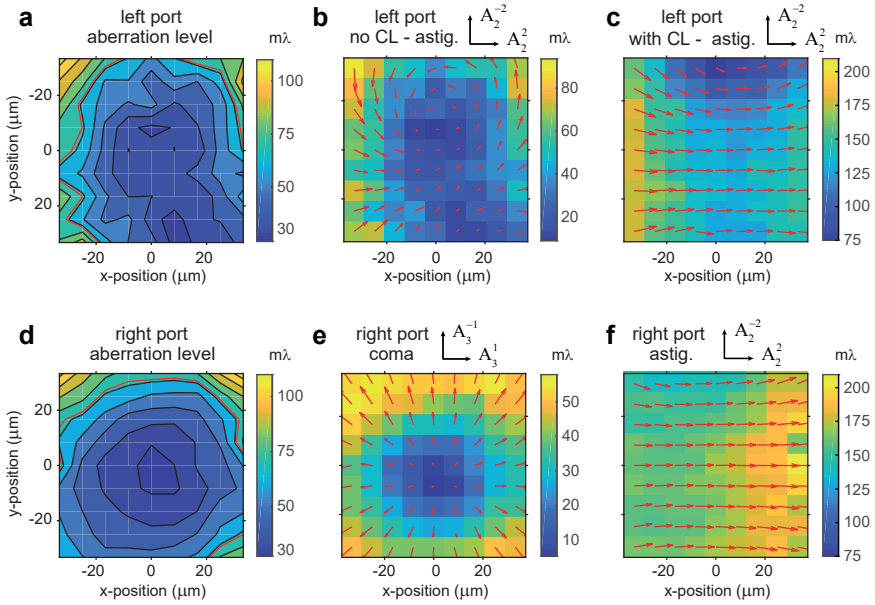

Figure 2.5: Field dependency of the aberrations for the CL-module (a-c) and AO module (d-f). (a) Aberration level in the field of view for the left camera port without CL. The red line indicates Maréchal's diffraction limit (<72 mλ) . (b) The most apparent aberration in the configuration of (a) is astigmatism. Color indicates the amount of astigmatism and the arrows the direction. (c) Induced astigmatism on the left port with CL. (d) Aberration level in the field of view for the right camera port with AO-module, corrected in the center of the FOV. The red line indicates Maréchal's diffraction limit (<72 mλ). (e) The most apparent aberration in the configuration of (d) is coma. Color indicates the amount of coma and the arrow the direction. (f) Field dependency of the induced astigmatism (100 nm rms) on the right port with DM.

2.3.3 Image deformation

When using the CL, we noted that its insertion into the optical path induced a deformation of the image in one direction (Figure 2.4a). To quantify this, we imaged fluorescent particles immobilized on the coverslip and measured how the position of their imaged altered upon insertion of the lens. This revealed a lateral displacement that increased linearly with the distance from the center of the field of view, consistent with a decrease in magnification of 3.6% (Figure 2.4b-d). In contrast, inducing astigmatism using the DM did not induce a change in magnification (Figure 2.4c&d). Although the precise optical design of the CL-module has not been published, this demagnification indicates that the CL is not inserted in the pupil plane.

2.3.4 Astigmatism field dependency

Next, we assessed the field dependency of the induced astigmatism by moving a bead in a 11x11 grid over the FOV, taking a through-focus scan at each position and using a phase-retrieval algorithm to estimate the aberrations and the level of induced astigmatism. This was performed either without CL/DM-induced astigmatism and with CL/DM-induced astigmatism. The size of the FOV where the

aberration level is below the Maréchal's limit (<72 mλ) is comparable for both configurations (Figure 2.5a&d)). Strikingly, the most dominant for the CL-module (in the absence of the CL) was astigmatism (Figure 2.5b), while first-order coma was the most predominant aberration in the AO-module (Figure 2.5e). The latter is likely due to the two additional lenses in the 4F system. In the case of induced astigmatism, the direction of astigmatism induced by the DM was more homogeneous over the FOV compared to the CL-induced astigmatism and the level of astigmatism was also more consistent (Figure 2.5c&f). Thus, when performing SMLM the AO-module is expected to provide a higher degree of 3D-accuracy across a large FOV, although for optimal usage both methods would require a field-dependent lookup table [23].

2.3.5 Optimal astigmatic encoding

Next, we wanted to explore the optimal amount of astigmatism to encode the x,y,z-location with minimal uncertainty. First, we noted that, in contrast to inducing astigmatism with a CL, deformable-mirror induced astigmatism did not alter the imaging depth at which the point spread function was symmetric. Instead, the DM shifted both the x- and y-focal points, both in opposite directions away from the initial focus (Figure 2.6a&b). This displacement away from the original focus, called the focal plane offset, increased nearly linearly from 0 to 300 nm when increasing the astigmatism from 0 to 100 nm RMS (Figure 2.6c). For all these different focal plane offsets, we created calibration curves that could be linearly approximated to yield a calibration slope α (nm/px) (Figure 2.6d&e). From this and the uncertainties in the x-width and y-width obtained from fitting, we then determined the uncertainty in z as a function of the z-stage position and compared this to the CRLB and the experimentally determined localization precision (Figure 2.6f). This revealed that the measured localization precision was optimal in the focal plane and increased away from focus. Both the least-squares standard error and the CRLB of the localization precision were below the experimentally determined localization precision, which we attributed to drift and model errors.

To examine how the z-precision depends on the amount of induced astigmatism, we determined the z-precision, averaged over a ±250 nm z-range, for increasing amounts of astigmatism both experimentally and using the CRLB (Figure 2.6g). After a strong increase in precision when increasing astigmatism from 0 to 40 nm, the experimentally determined precision did not further improve, while the CRLB improved only marginally. Since increasing astigmatism will increase the PSF width, the precision in the x and y position will decrease (Figure 2.6h). Therefore, the overall localization precision combined for x-, y- and z-direction, averaged over a ±250 nm z-range, shows an optimum of astigmatism around 60 nm, both experimentally and theoretically (Figure 2.6j).

2.3.6 Imaging proof-of-principle

Finally, we tested whether using the DM for aberration correction and astigmatism-based z-encoding would allow three-dimensional nanoscopic imaging 10 μm away from the coverslip. For this, we used the epithelial brush border of Caco2 cells,

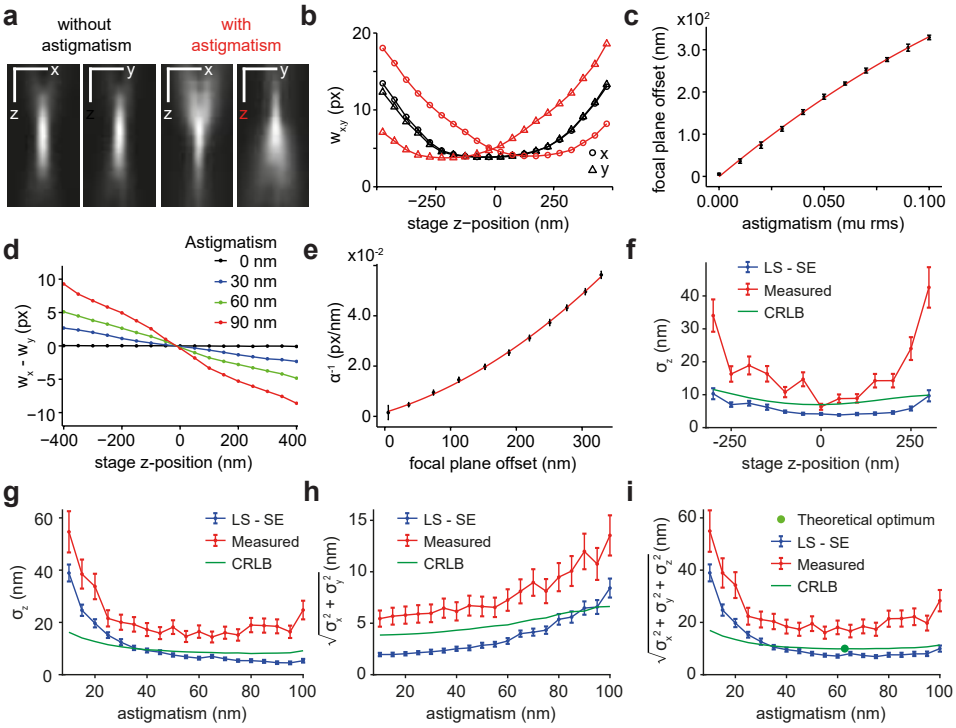

Figure 2.6: Tunability of astigmatism. (a) Cross sections in x and y of a PSF of a 100 nm green fluorescent bead without astigmatism (left panels) and with 50 nm RMS astigmatism induced with the DM (right panels). Pixel size in z is 20 nm. (b) PSF width of a 100 nm green fluorescent bead in x (circles) and y (triangles) as function of the z-position of the stage, without astigmatism (black) and with 0.05 μm RMS astigmatism induced with the DM (red). (c) Focal plane offset as function of the amount of induced astigmatism (mean ± sd, N = 5 beads). Red line represents a least squares fit with a second order polynomial. (d) Difference between PSF x-width and y-width as function of the z-stage position for astigmatism levels of 0 nm (black), 30 nm (blue), 60 nm (green) and 90 nm (red). (e) Absolute values of the inverse of calibration slope α as function of the focal plane offset (mean ± sd, N = 5). A second order polynomial was fit to the data. (f) Axial localization precision as function of z-position for the measured precision, least-squares standard error and CRLB with 60 nm of astigmatism. (g-i) Axial (g), lateral (h) and total (i) localization precision as function of induced astigmatism averaged over a ±250 nm z-range.

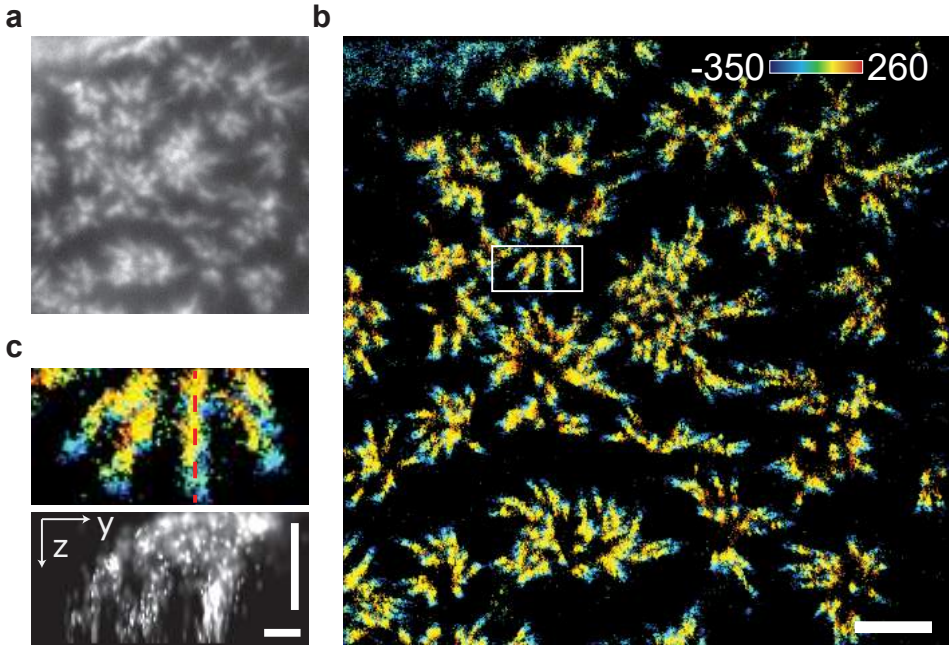

Figure 2.7: Adaptive optics improves 3D SMLM using OI in Caco2-cell monolayers. (a) Widefield image of Ezrin-AF647 in a monolayer of Caco2 cells at a depth of 12 μm. (b) 3D SMLM reconstruction of (a). Scalebars is 1 μm. (c). Zoom of the area in the white box in the right panel of (b) and cross section at the red dotted line (bottom panel). Scalebars are 500 nm.

which consists of actin-rich protrusion called microvilli. Microvilli were stained using antibodies against the actin interacting protein Ezrin (Figure 2.7). Importantly, using astigmatism-based z-detection we could clearly resolve tilted microvilli at a depth of around 12 μm (Figure 2.7c). Thus, a DM in combination with a high NA OI objective enables three-dimensional nanoscopy deep in watery samples.

2.4 Discussion

Here we have tested the 2D- and 3D-SMLM performance of an OI objective with and without AO as function of imaging depth and compared it to a WI objective without adaptive optics. For 2D-SMLM we found that when using OI at imaging depths above 5 μm, the use of a DM to correct aberrations improves localization precision, effectively doubling the amount of localizations with a precision below 15 nm at 24 μm depth. The achieved localization precision with WI does not degrade when imaging deeper, but when corrected for the collection efficiency, WI is outperformed by OI plus AO. OI plus AO results in a 14% improvement in (median) localization precision compared to WI for relevant photon levels. This improvement in localization precision does come at the expense of a more complicated and less stable optical setup that has to be optimized for every sample/acquisition.

To encode the z-position for 3D-SMLM, astigmatism was induced using either a CL or the DM. We found that using a CL in combination with an OI objective resulted in quickly deteriorating z-encoding when increasing imaging depth, which has been recently reported by others as well, but had remained unexplained [13]. Our simulations revealed that the deterioration of the z-encoding is due to left-over higher-order spherical aberration. Without the refractive index mismatch the z-encoding is maintained over large depths, as we showed using a CL in combination with WI. An advantage of the DM is that a tunable amount of astigmatism can be induced. This could be used for optimizing the amount of astigmatism for each imaging application [10]. However, we also found that there is an optimal amount of astigmatism based on the changes in x, y and z localization precisions as function of astigmatism. This suggests that a well-chosen CL combined with a WI objective could perform 3D SMLM, albeit with a reduced localization precision compared to OI with adaptive optics. Furthermore, when imaging in more inhomogeneous samples the increased importance of aberration correction might necessitate adaptive optics for optimal imaging.

Finally, we demonstrate 3D-SMLM imaging at 12 μm depth in biological samples using an OI objective with a DM. The robust DM-induced z-encoding enables discriminating microvilli lying on top of each other. Future work could explore the depth-dependent performance of other methods for achieving 3D-SMLM such as the saddle-point PSF [24] and double helix [25], which theoretically can have an isotropic localization precision. Finally, bi-plane imaging might be less sensitive to depth-induced aberration as it is less dependent on the exact shape of the PSF [26].

References

[1] M. Siemons, B. M. C. Cloin, D. M. Salas, W. Nijenhuis, E. A. Katrukha, and L. C. Kapitein, *Comparing strategies for deep astigmatism-based single-molecule localization microscopy,* Biomed Opt Express **11**, 735 (2020).

[2] E. Betzig, G. H. Patterson, R. Sougrat, O. W. Lindwasser, S. Olenych, J. S. Bonifacino, M. W. Davidson, J. Lippincott-Schwartz, and H. F. Hess, *Imaging intracellular fluorescent proteins at nanometer resolution,* Science **313**, 1642 (2006).

[3] M. J. Rust, M. Bates, and X. Zhuang, *Sub-diffraction-limit imaging by stochastic optical reconstruction microscopy (storm),* Nat Methods **3**, 793 (2006).

[4] T. J. Gould, S. T. Hess, and J. Bewersdorf, *Optical nanoscopy: from acquisition to analysis,* Annu Rev Biomed Eng **14**, 231 (2012).

[5] B. Huang, W. Wang, M. Bates, and X. Zhuang, *Three-dimensional super-resolution imaging by stochastic optical reconstruction microscopy,* Science **319**, 810 (2008).

[6] I. Izeddin, M. El Beheiry, J. Andilla, D. Ciepielewski, X. Darzacq, and M. Dahan, *Psf shaping using adaptive optics for three-dimensional single-molecule super-resolution imaging and tracking,* Opt Express **20**, 4957 (2012).

[7] B. C. Coles, S. E. Webb, N. Schwartz, D. J. Rolfe, M. Martin-Fernandez, and V. Lo Schiavo, *Characterisation of the effects of optical aberrations in single molecule techniques,* Biomed Opt Express **7**, 1755 (2016).

[8] M. Schwertner, M. J. Booth, and T. Wilson, *Specimen-induced distortions in light microscopy,* J Microsc **228**, 97 (2007).

[9] D. S. Wan, M. Rajadhyaksha, and R. H. Webb, *Analysis of spherical aberration of a water immersion objective: application to specimens with refractive indices 1.33-1.40,* J Microsc **197**, 274 (2000).

[10] D. Burke, B. Patton, F. Huang, J. Bewersdorf, and M. J. Booth, *Adaptive optics correction of specimen-induced aberrations in single-molecule switching microscopy,* Optica **2**, 177 (2015).

[11] M. J. Mlodzianoski, M. F. Juette, G. L. Beane, and J. Bewersdorf, *Experimental characterization of 3d localization techniques for particle-tracking and super-resolution microscopy,* Opt Express **17**, 8264 (2009).

[12] Y. Li, Y. L. Wu, P. Hoess, M. Mund, and J. Ries, *Depth-dependent psf calibration and aberration correction for 3d single-molecule localization,* Biomed Opt Express **10**, 2708 (2019).

[13] R. McGorty, J. Schnitzbauer, W. Zhang, and B. Huang, *Correction of depth-dependent aberrations in 3d single-molecule localization and super-resolution microscopy,* Opt Lett **39**, 275 (2014).

[14] M. J. Mlodzianoski, P. J. Cheng-Hathaway, S. M. Bemiller, T. J. McCray, S. Liu, D. A. Miller, B. T. Lamb, G. E. Landreth, and F. Huang, *Active psf shaping and adaptive optics enable volumetric localization microscopy through brain sections,* Nat Methods **15**, 583 (2018).

[15] A. Edelstein, N. Amodaj, K. Hoover, R. Vale, and N. Stuurman, *Computer control of microscopes using micromanager,* Curr Protoc Mol Biol **Chapter 14**, Unit14 20 (2010).

[16] M. J. Booth, M. A. A. Neil, R. Juškaitis, and T. Wilson, *Adaptive aberration correction in a confocal microscope,* Proceedings of the National Academy of Sciences **99**, 5788 (2002).

[17] E. Hecht, *Optics*, 4th ed. (Addison-Wesley, Reading, Mass., 2002) pp. vi, 698 p.

[18] R. P. Tas, C. Y. Chen, E. A. Katrukha, M. Vleugel, M. Kok, M. Dogterom, A. Akhmanova, and L. C. Kapitein, *Guided by light: Optical control of microtubule gliding assays,* Nano Lett **18**, 7524 (2018).

[19] B. Huang, S. A. Jones, B. Brandenburg, and X. Zhuang, *Whole-cell 3d storm reveals interactions between cellular structures with nanometer-scale resolution,* Nat Methods **5**, 1047 (2008).

[20] A. Chazeau, E. A. Katrukha, C. C. Hoogenraad, and L. C. Kapitein, *Studying neuronal microtubule organization and microtubule-associated proteins using single molecule localization microscopy,* Neuronal Cytoskeleton, Motor Proteins, and Organelle Trafficking in the Axon **131**, 127 (2016).

[21] M. Siemons, C. N. Hulleman, R. O. Thorsen, C. S. Smith, and S. Stallinga, *High precision wavefront control in point spread function engineering for single emitter localization,* Opt Express **26**, 8397 (2018).

[22] S. Stallinga and B. Rieger, *Accuracy of the gaussian point spread function model in 2d localization microscopy,* Opt Express **18**, 24461 (2010).

[23] A. von Diezmann, M. Y. Lee, M. D. Lew, and W. E. Moerner, *Correcting field-dependent aberrations with nanoscale accuracy in three-dimensional single-molecule localization microscopy,* Optica **2**, 985 (2015).

[24] Y. Shechtman, S. J. Sahl, A. S. Backer, and W. E. Moerner, *Optimal point spread function design for 3d imaging,* Phys Rev Lett **113**, 133902 (2014).

[25] S. R. Pavani, M. A. Thompson, J. S. Biteen, S. J. Lord, N. Liu, R. J. Twieg, R. Piestun, and W. E. Moerner, *Three-dimensional, single-molecule fluorescence imaging beyond the diffraction limit by using a double-helix point spread function,* Proc Natl Acad Sci U S A **106**, 2995 (2009).

[26] M. F. Juette, T. J. Gould, M. D. Lessard, M. J. Mlodzianoski, B. S. Nagpure, B. T. Bennett, S. T. Hess, and J. Bewersdorf, *Three-dimensional sub-100 nm resolution fluorescence microscopy of thick samples,* Nat Methods **5**, 527 (2008)
.

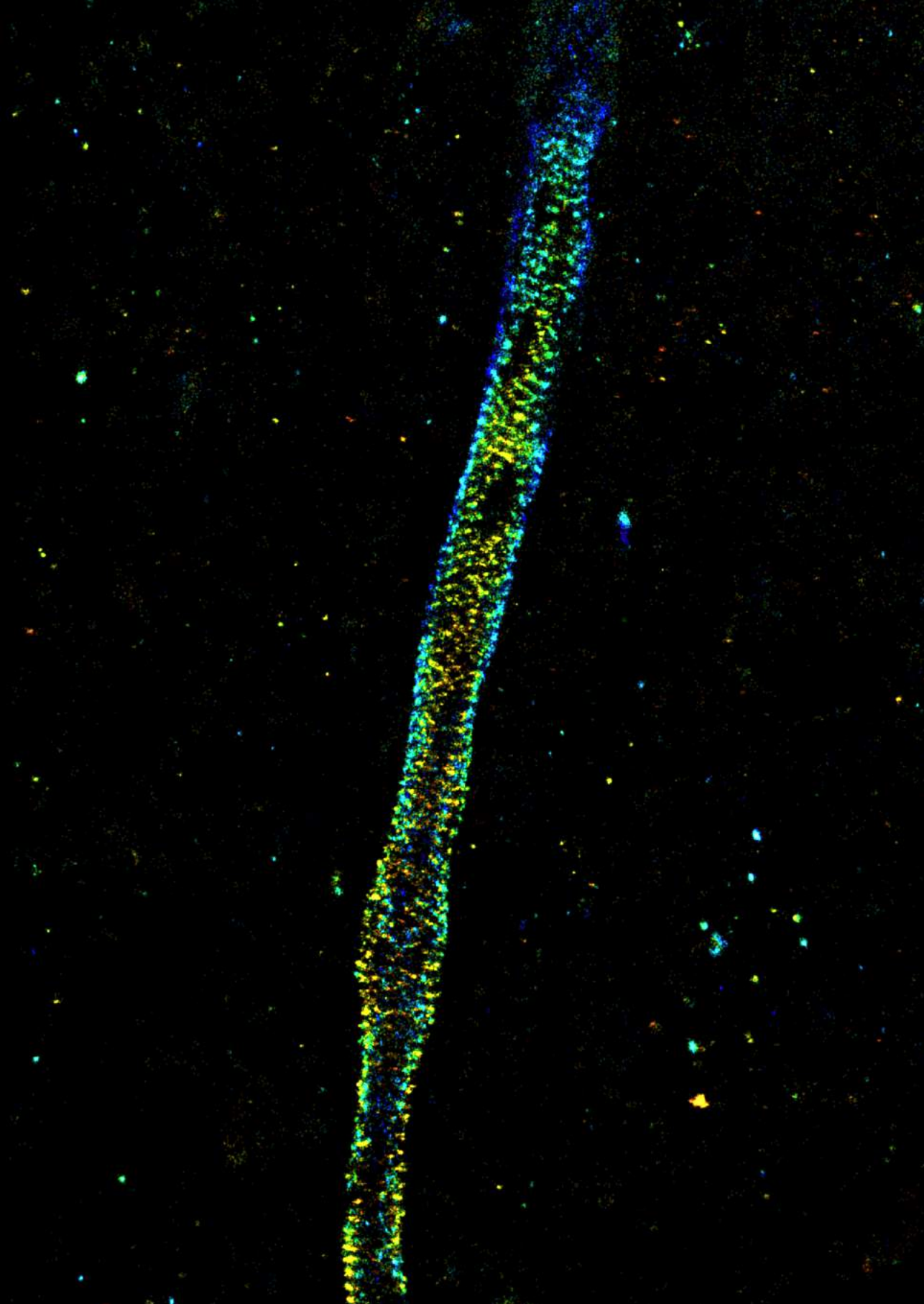

3

Robust adaptive optics for localization microscopy deep in complex tissue

Single-Molecule Localization Microscopy (SMLM) provides the ability to determine molecular organizations in cells at nanoscale resolution, but in complex biological tissues, where sample-induced aberrations hamper detection and localization, its application remains a challenge. Various adaptive optics approaches have been proposed to overcome these issues, but the exact performance of these methods has not been consistently established. Here we systematically compare the performance of existing methods using both simulations and experiments with standardized samples and find that they often provide limited correction or even introduce additional errors. Careful analysis of the reasons that underlie this limited success enabled us to develop an improved method, termed REALM (Robust and Effective Adaptive Optics in Localization Microscopy), which corrects aberrations of up to 1 rad RMS using 297 frames of blinking molecules to improve single-molecule localization. After its quantitative validation, we demonstrate that REALM enables to resolve the periodic organization of cytoskeletal spectrin of the axon initial segment even at 50 μm depth in brain tissue.

This chapter has been published in Nature Communications **12**, 3407 (2021) [1].

3.1 Introduction

Single-Molecule Localization Microscopy (SMLM) [2–4] enables the investigation of the nanoscale organization of cellular structures through repetitive localization of different sparse subsets of fluorophores. SMLM has provided key insights into the nanoscale organization of molecules in cultured cells, including the discovery of sub-membranous actin-spectrin rings in axons [5, 6]. Cultured cells, and neurons in particular, have limitations as model systems, because they lack most of the three-dimensional cellular organization and neurochemical conditions that are present in vivo, including extracellular matrix proteins and nutritional support from glial cells. On the other hand, performing SMLM deep inside tissue or organoids has remained challenging due to sample-induced aberrations. Accurate localization requires sufficient signal to noise and a non-aberrated point-spread-function (PSF) [7–9], both of which are compromised when imaging in biological tissue, in which a range of distinct cellular components cause complex light scattering [10].

One solution is to perform low-depth ($\sim$10 μm) imaging in thin sections [7–9]. However, in such experiments most cells within imaging range have been sectioned to some extent, precluding live-cell experiments in such preparations. In contrast, acutely cut >250 μm thick serial sections from the brain preserve most of the characteristics of the neuronal cytoarchitecture and allow the ex vivo study of electrophysiological properties. This brain slice preparation is one of the most widely used preparations in neuroscience and facilitates structure-function studies of intact and electrically active brain cell microcircuits. For these reasons, there is a clear need to perform optical nanoscopy deep inside these aberrating samples.

An important methodology to overcome tissue-induced aberrations is the use of intensity based Adaptive Optics (AO), which uses a deformable mirror in the emission path to compensate for wave-front distortions. The required shape of the mirror can be found by iteratively optimizing the contrast of the image (or guide star when possible) [11]. However, in SMLM the acquisitions are noisy and contain a strongly fluctuating amount of signal photons, rendering traditional approaches unusable. Various SMLM-specific AO-methods have been proposed to overcome these issues [12–14], but the exact performance of these different AO-methods has not been consistently demonstrated and it has remained unclear what level of aberrations these methods can correct and under which conditions.

Here, we systematically compare the performance of existing methods using both simulations and experiments with standardized samples. We find that for realistic total signal and background ratios these methods provide only limited correction or introduce additional errors. Careful analysis of the reasons that underlie this limited success enabled us to develop an improved method, termed REALM (Robust and Effective Adaptive Optics in Localization Microscopy), which corrects aberrations of up to 1 rad RMS using 297 frames of blinking molecules, thereby enabling robust SMLM at 50 μm depth and even up to 80 μm depth when pre-correcting spherical aberration.

3.2 Results

Aberrations alter the point spread function (PSF), decreasing contrast and the spatial frequency support (see Figure 3.1a-d). The key for intensity-based AO is to find a relevant metric, a quality measure computed from the acquisitions, in combination with an optimization algorithm to efficiently and robustly optimize the metric [15]. To reduce the effect of strongly fluctuating signal levels of the acquisitions, all existing methods propose a weighted sum of the Fourier transform of the acquisition as metric, while differing in the specific weighting of the spatial frequencies and in normalization (see insert Figure 3.1d). We termed these methods 1, 2 and 3, with metrics M1, M2 and M3, corresponding to Burke et al. [12], Tehrani et al. [13], and Mlodzianoski et al. [14], respectively. Because SMLM acquisitions are comprised of pseudo-random point sources, these methods effectively optimize the magnitude transfer function. As optimization algorithm to maximize the value of the metrics, Burke et al. use model-based optimization, Tehrani et al. use particle-swarm optimization, and Mlodzianoski et al. use downhill simplex optimization.

In order to systematically compare between different methods, we first sought to establish a standardized sample with tunable signal and background values. Therefore, we used a DNA-PAINT-based sample where molecules transiently bind to the coverslip, mimicking blinking [16] (see Figure 3.1a). This sample maintains stable signal and noise levels during the complete experimental sequence of several hours (see Methods and Supplementary Figure 3.A.1). Using a setup with a carefully calibrated deformable mirror (see Methods and Supplementary Figures 3.A.2 and 3.A.3) we introduced 25 random aberration configurations of 0.75 rad RMS wave-front error, consisting of random combinations of Zernike modes up to the fourth radial order (excluding piston, tip, tilt and defocus) and assessed how well the various methods were able to correct these aberrations (see Figure 3.1e&f). In order to achieve a realistic signal and background level, we tuned the emitter density and intensity to around 20 emitters per frame and 2500 signal photons per emitter. Transmission brightfield illumination was used to substantially increase the background level to 20 photons per pixel in the 400x400 pixel field of view, resulting in a total signal background ratio (SBR) of 0.016 (2500 signal photons x 20 emitters / (20 background photons x 400x400 pixels)). In addition, we tested the performance of the methods on simulated data sets (see Methods).

In both the standardized experiments and the simulations, we found that the previously proposed methods were unable to meaningfully correct the aberrated wave-front. For example, method 1 and method 2 increased the aberration level in 100% and 48% of the experimental cases, respectively, whereas method 3 decreased the aberration level only by 20% (0.16 rad RMS) on average. The experimentally achieved corrections deviated to some extent from the simulation results (Figure 3.1f), likely due to additional noise sources such as read noise and fixed pattern noise from the camera, which are not included in the simulation. Furthermore, the small initial aberration introduced by the DM limited the experimentally achievable aberration level to 0.2 rad RMS (Supplementary Figure 1e). Nonetheless, both simulations and experimental data show that none of the three methods robustly achieves proper correction (here taken as a Strehl-ratio of 0.9).

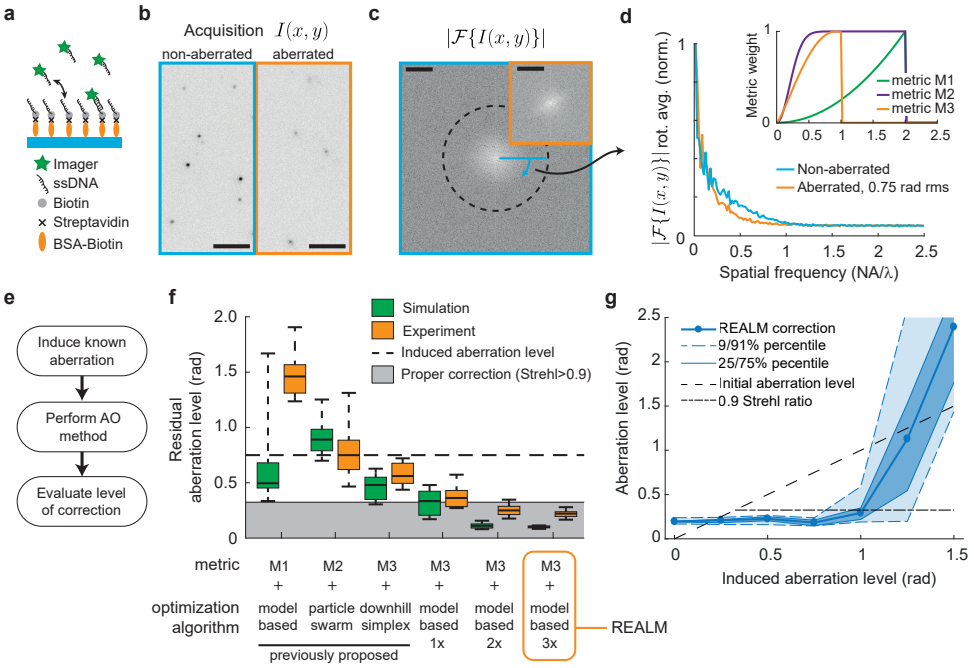

Figure 3.1: Systematic comparison between different AO methods reveals that only REALM achieves robust correction. a) DNA-PAINT test sample: imager strands bind transiently to the coverslip, mimicking single-molecule blinking with consistent signal levels for many hours. b) Representative acquisition of a non- and 0.75 rad RMS aberrated acquisition (I(x,y)) corresponding to (f) (n = 625). Scale bar indicates 5 μm. c) Absolute value of the 2D Fourier transform of a non-aberrated acquisition and aberrated acquisition of (b) (orange insert, center crop) ($|FI(x,y)|$). Dashed line indicates $2NA/\lambda$. Scale bars indicate NA/λ. d) The rotational average of (c) shows that noise dominates spatial frequencies above 1 NA/λ. The major decrease in the MTF due to aberrations occurs between 0.25 and 1 NA/λ. Insert shows the spatial frequency weights of the different proposed metrics. e) Strategy for comparing AO methods by inducing known aberrations in a well-corrected system. f) Performance of different AO metrics and optimization algorithms. Boxplot indicates 9/91-percentile, 25/75-percentile and median for 25 random aberration configurations of 0.75 rad rms wave-front error consisting of random combinations of Zernike modes up to the fourth radial order (excluding piston, tip, tilt and defocus). Each frame contains on average 13 emitters, emitting 2500 photons with a background of 20 photons per pixel. See Suppl. Fig. 1 for more details. g) Performance of REALM as function of induced aberration level (10 random aberration configurations). Each frame contains on average 17 emitters, emitting 2465 photons with a background of 40 photons per pixel.

To understand why correction often fails, we next examined how the different metrics depend on noise levels and aberrations. The spatial frequency content of acquisitions in non-aberrated and aberrated conditions revealed that, in both cases, spatial frequencies above 1 NA/λ are dominated by noise (see Figure 3.1d). Metric M1 and M2 have the highest weights for these frequencies, which includes a large amount of noise in the metric value. In contrast, M3 only weights the low spatial frequencies (<1 NA/λ, where signal levels are much higher. This makes metric M3 the most robust measure of the MTF and explains why M3 enables consistent correction, albeit without reaching diffraction-limited imaging.

We wondered whether the limited correction obtained using metric M3 could be caused by the use of simplex optimization. The simplex optimization is sensitive to local noise in the parameter space as it only compares two values per optimization parameter. In contrast, model-based optimization iteratively corrects Zernike modes by applying a sequence of biases for each Zernike mode to be corrected. The metric values for these series of acquisitions are then fitted to a curve (the model or so-called metric curve) to find the optimum (see Supplementary Figure 3.A.4) [17]. This procedure reduces noise and therefore appears more suitable for AO in SMLM, as originally proposed by Burke et al. To test this, we implemented metric M3 in combination with model-based optimization. We first simulated aberrated acquisitions to assess the metric curve and found that it could be approximated by a Gaussian function with offset within a range of 1 rad per Zernike mode (see Supplementary Figure 3.A.5). Next, we used a series of simulations to optimize our method in terms of maximum bias range, the number of biases per Zernike mode, and the number of correction rounds (see Supplementary Figure 3.A.6).

These simulations provided two key insights. First, they revealed the importance of varying the bias over a sufficiently large range to confidently estimate the optimal bias (see Supplementary Figure 3.A.6a-c). In order to estimate the optimal bias with a high precision, the contrast in the metric value has to be as large as possible and needs to be probed $\sim$0.5-0.75 rad around the optimum. We found that using a maximum bias range of ±1 rad resulted in the best correction, which is in line with previous work on model-based modal aberration correction [17]. Secondly, these simulations revealed that the precision of the estimated optimal bias depends on the amount of aberration in the other modes, i.e. the contrast in the obtained metric values for the Zernike mode that is being corrected improves when the overall level of aberration is lower. Consequently, the use of multiple correction rounds improves the correction (see Figure 3.1f and Supplementary Figure 3.A.6d-f). The optimization analysis indicated that there are two efficient correction strategies: either 3 correction rounds, with 9 biases per Zernike mode (3x9x11=297 acquisitions) or 2 correction rounds with 13 biases per Zernike mode (2x13x11=286 acquisitions). The latter option appeared to perform slightly more robust in the conditions with low SBR, whereas the first option achieved slightly better correction if the aberration profile was very unevenly distributed between Zernike modes. In all cases, it was beneficial to first correct the Zernike modes expected to dominate, such as spherical aberration, because for any mode the correction precision depends on the amount of aberration in the other modes.

We experimentally verified this approach using the DNA-PAINT sample and were able to consistently reduce the induced wave-front error of 0.75 rad RMS by a factor of two in the first correction round (99 acquisitions). The second correction round (another 99 acquisitions) yielded further improvement and achieved diffraction-limited imaging in 21 out of 25 cases, whereas after the third correction round (297 acquisitions in total) all induced aberrations were corrected (see Figure 3.1f). We termed this method REALM (Robust and Effective Adaptive Optics in Localization Microscopy) and implemented it as a freely available and open source Micro-Manager plugin [18] (see Methods). The performance of REALM was evaluated further by measuring the aberration correction for increasing amounts of induced aberrations and different signal background ratios. This revealed that our method was able to robustly correct aberrations of up to 1 rad RMS (see Figure 3.1g and Supplementary Figure 3.A.7) for various signal and noise levels. Even with very low signal levels (6 emitters on average, 1745 signal photons per emitter and 216 background photons, 0.0003 SBR) REALM was able to correct significant aberrations (see Supplementary Figure 3.A.7c).

We next aimed to test this approach for SMLM using more complex experimental samples. Previously, Mlodzianoski et al. used a water-filled cavity to validate their method [14]. However, such a sample does not fully capture the complexity of complex tissue, where cell bodies, capillaries and nerve fibers all may act as obstacles for light and distort the wavefront. Others have tested their AO method using fluorescent beads imaged through the nematode C. elegans [13]. While this assay features a richer aberration profile, the beads are bright and do not exhibit blinking dynamics. In an effort to better mimic deep-tissue localization microscopy, we performed SMLM on COS-7 cells stained for microtubules (a staple reconstruction test in SMLM), but imaged these cells through brain sections of 50 and 80 μm thickness (see Figure 3.2 and Supplementary Figure 3.A.8). We chose this sample over stained tissue for our first analyses, because these microtubule immunostainings are highly reproducible and result in recognizable structures. To address the scattering induced by the sample we mounted the brain sections in a glycerol-based buffer instead of a water-based buffer, similar to previous work [7]. This reduces scattering by reducing the local differences in refractive index between the subcellular content and the mounting medium. Slices mounted in this buffer appear almost transparent in regions such as the cortex, indicating that scattering is indeed reduced. We estimated that the refractive index of brain sections in this buffer is around 1.48 (assuming an overall refractive index of 1.4 and a water content of 70% before incubation in the glycerol buffer). We therefore used a 1.49 NA oil objective to ensure larger collection efficiency and less sample-induced spherical aberrations compared to a silicon immersion objective lens (see Supplementary Figure 3.A.9).

With this assay, we performed a systematic comparison between REALM and no-AO conditions by switching between the system-corrected state (without REALM) and the sample-corrected state (with REALM) every 500 frames during the SMLM acquisition. We found that REALM increased the number of successful localizations (see methods for classification details) up to 6-fold, resulting in a strongly improved reconstruction (see Figure 3.2). The resolution estimated using Fourier

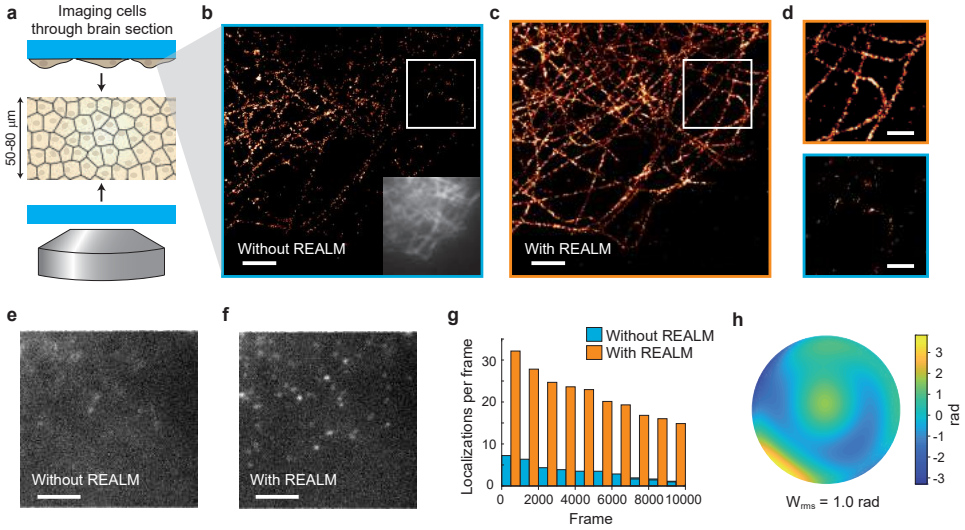

Figure 3.2: . Improved single-molecule imaging through brain sections using REALM. a) Illustration of the sample. A 50 μm brain slice is mounted in between two cover glasses, on one of which COS-7 cells were grown. These cells were stained for microtubules (αTub) and imaged through the brain section, to mimic deep-tissue imaging. b-c) SMLM reconstruction of microtubules in COS-7 cells through a 50 μm thick brain section with 5000 frames without AO sample correction (without REALM, panel b) and with sample-based correction (with REALM, panel c). Insert in panel b shows the widefield image prior to correction. FRC resolution is 196 nm and 127 for (b) and (c) respectively. Scale bars indicates 2 μm. d) zoom of (b) and (c) indicated by white square. Scale bars indicates 1 μm. e-f) Representative single acquisitions corresponding to the reconstruction of (b) and (c) respectively. Scale bars indicate 4 μm. g) Number of localizations in the acquisition series during which the DM alternated between the system-corrected state (without REALM) and sample-corrected state (with REALM) every 500 frames. h) Estimated wave-front distortion as estimated using REALM, of which 0.55 rad was used as initial guess for primary spherical aberration. Repeated n = 10 times in 3 distinct samples.

Ring Correlation (FRC) improved by 35% when using REALM. For the 80 μm thick slices, we estimated the spherical aberration to be around 100 nm and used this for pre-correction. We switched the DM between this pre-corrected state and the sample-corrected state and again found an improvement in both the number of detected events when using REALM as well as the FRC (24% improvement) (see Supplementary Figure 3.A.8), indicating that non-spherical aberrations contribute considerably to image deterioration as well.

We found that without AO blinking events are detectable only if the events are bright and perfectly in focus. This approach still yielded recognizable features in the reconstruction (see Figure 3.2b), but with much lower number of localizations. This was caused by the aberrated PSF, which quickly broadened when molecules were slightly out of focus (±100-200nm) and therefore significantly hampered detection (see Figure 3.2e and Supplementary Movie 1). With REALM, the PSF is more symmetric and remains focused along the focal depth of the objective. This increases the detection of dim blinking events as well as the detection of molecules inside the complete depth of focus. Therefore the reconstruction with REALM also

contains microtubule structures that are not visible in the reconstruction without AO (see Figure 3.2d). Although the ground-truth aberrations were unknown, the increase in the number of detected events, as measured using the exact same fluorescent structures, demonstrates the success of the AO algorithm.

We next used a similar sample (COS-7 cells imaged through 60 μm thick brain slices) to directly compare REALM to the method proposed by Mlodzianoski et al., (see Supplementary Figure 3.A.10). This revealed that REALM was more effective in restoring the PSF, which consequently improved detection and localization. Overall, this resulted in a 2.2x increase (median) in number of localizations with a localization precision below 20 nm and a 8.6x increase in the number of localizations with a precision below 5 nm. Even when we extended the previously published method by including more Zernike modes than originally proposed, it could not achieve the same correction as REALM. The FRC resolution improved from 150 nm (median) when using the method of Mlodzianoski et al. to 120 nm (median) when using REALM. On average, REALM estimated the aberrations to be around 1 rad RMS, whereas the method of Mlodzianoski et al. resulted in a 3-fold lower estimate, leaving an average residual aberration of around 0.7 rad RMS. These results demonstrate that REALM achieves a 3-fold improvement in aberration correction over previous methods and enables robust single-molecule imaging at 60 μm depth through brain tissue with improved resolution.

Next, we aimed to image structures stained within the tissue itself and focused on the axon initial segment (AIS) of cortical layer 5 pyramidal neurons in rat brain slices of 300-400 μm thickness. Landmark SMLM experiments have used neurons cultured on coverslips to reveal that axons display a 190 nm actin-spectrin based periodic structure called the membrane-associated periodic scaffold (MPS) 4, which at the AIS includes βIV-spectrin 4, 5. However, due to the limited imaging depth of conventional SMLM, correlating these structures to functional recordings of neurons in brain slices is not possible. In acute brain slices healthy neurons are typically located at >30 μm depth from the slice surface and can be reliably targeted by a patch pipette up to 100 μm depth [19]. Using REALM, we could perform multiplane 3D astigmatic SMLM imaging on βIV-spectrin stained brain sections up to a depth of 50 μm (Figure 3.3). We resolved the periodic patterning of this scaffolding protein in 3D and revealed a periodicity of 203 ± 10 nm (mean ± s.d., Figure 3.3, and Supplementary Figure 3.A.11). For details of the estimated aberrations see Supplementary Figure 12. Beyond 50 μm depth, the increase background levels hindered both REALM and single-molecule detection.

To further examine the improvement achieved by REALM we imaged βIV-spectrin in slices and switched between uncorrected and corrected mirror states during the acquisition, which resulted in an improved reconstruction upon correction (76 nm FRC with AO, 100 nm FRC without AO, see Supplementary Figure 3.A.13a). In addition to improving the number of detections and the FRC, the use of Adaptive Optics also corrected the loss of ellipticity when performing astigmatic 3D SMLM [14, 20]. We observed a depth-dependent increase in aberrations (see Supplementary Figure 3.A.13d) and have shown in previous work [20] that this loss of ellipticity is due to (higher order) spherical aberration, revealing why the applied astigma-

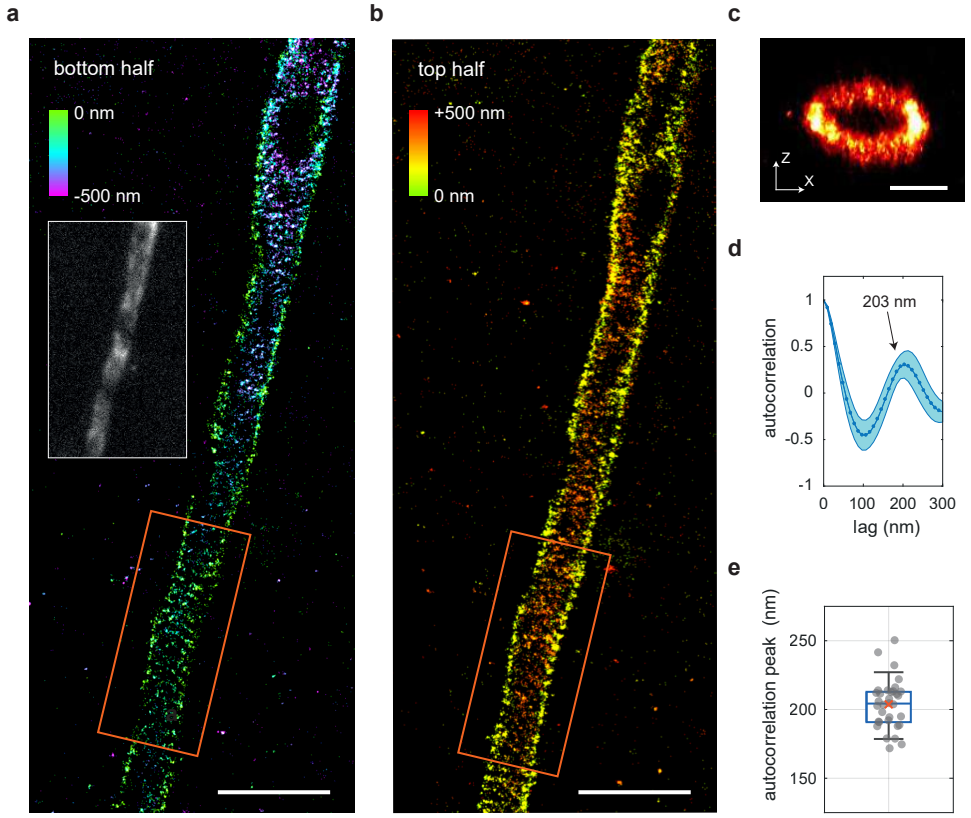

Figure 3.3: Resolving the nanoscale spectrin organization in axons at 50 μm depth. a-b) SMLM reconstruction of the upper half (panel a) and lower half (panel b) of a layer 5 pyramidal neuron AIS stained for βIV-spectrin in a rat brain slice at 50 μm depth. Color encoding indicates the z-position. Scale bars indicates 2 μm. Insert with white rim shows the widefield image prior to aberration correctionThe holes in βIV-spectrin pattern are likely sites of synaptic connections. Scale bar indicates 2 μm. c) z-x cross-section of the rectangular orange area indicated in (a-b). Scale bar indicates 500 nm (both directions). d) The average autocorrelation (blue line) of 30 line segments in the reconstruction of 3.2(a,b) and Supplementary Figure 3.A.11 shows a peak at 203 ± 10 nm. Shaded region indicates the standard deviation. e) Distribution of the estimated autocorrelation peaks of the individual line segments of reconstructions of 3.2(a,b) and Supplementary Figure 3.A.11. Boxplot indicates 9/91-precentile, 25/75-precentile and median. Red cross indicates the mean autocorrelation distance. See also Supplementary Figure 3.A.11. Repeated n=12 times in 4 distinct samples with similar results.

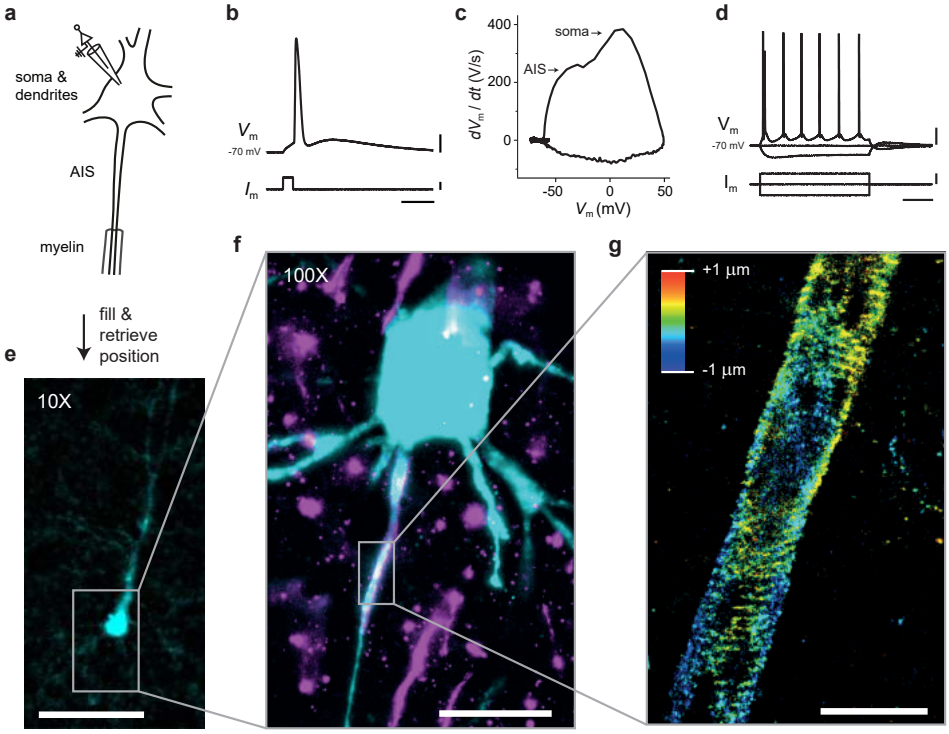

Figure 3.4: Proof-of-principle for following up electrophysiological recordings with 3D SMLM in brain sections. a) Schematic of electrophysiological whole-cell patch clamp recording. b) An action potential of a layer 5 pyramidal neuron in an acute brain slice patched at 35 μm depth. Vm, membrane potential and IM, injected current. Scale bars indicate from top to bottom: 20 mV, 500 pA and 10 ms. c) Phase-plane plot (dVm /dt versus Vm) of the action potential shown in (b) showing separate peaks from the AIS and the somatodendritic compartment. d) The membrane potential (Vm) in response to negative and positive current injections (Im). Scale bars indicate from top to bottom: 20 mV, 200 pA, 200 ms. e) Widefield image (10X) of the whole-cell recorded and biocytin-filled pyramidal neuron (b-d) labelled with streptavidin-Alexa488. Scale bar indicates 100 μm. f) Same as (e) but with a 100X objective. Magenta shows the βIV-spectrin-Alexa647 staining. Scalebar indicates 20 μm. c) 3D SMLM reconstruction of the βIV-spectrin at the AIS of the same whole-cell patch clamped neuron (b-f). Single-molecule localizations of four focal planes are merged. Color depicts z-position. Scalebar indicates 2 μm.

tism level has to increase when imaging in tissue even with using AO. Without such an increased level of astigmatism, the z-encoding is lost, rendering volumetric multiplane astigmatic 3D SMLM unattainable because individual focal planes cannot be stitched (see Supplementary Figure 3.A.13b,c). Using PSF simulations described in our previous work [20] we could determine the theoretical required astigmatism level at each depth to obtain a constant calibration curve. Application of these estimated levels of astigmatism restored proper z-encoding and allowed volumetric multiplane astigmatic 3D SMLM (Figure 3.3 and Supplementary Figures 3.A.11 & 3.A.13).

Finally, we also successfully resolved the βIV-spectrin structure of a functionally identified pyramidal neuron in a brain section (see Figure 3.4). First, electrophysiological recordings were performed on a layer 5 pyramidal neuron (Figure 3.4a-d), after which the neuron was filled with biocytin, fixed and stained. After mounting of the brain section and application of the SMLM buffer, the position of the patched neuron was retrieved using the stained biocytin fill and a 10X objective. Subsequently, SMLM in combination with REALM was used to resolve the nanoscale architecture of βIV-spectrin, demonstrating the possibility to directly correlate functional studies and nanoscopic organization.

3.3 Discussion

In this work, we systematically analyzed the performance of different AO techniques for SMLM using standardized samples. Comparing different methods in an objective and robust manner is challenging, because signal and background levels can vary dramatically between samples and often also rapidly change during acquisitions. To overcome this, we first used DNA-PAINT in combination with a well-calibrated deformable mirror to compare and validate the performance of previously published methods in identical signal and background levels, while systematically varying the levels and types of aberrations. We augmented these experiments with simulations to further compare how different methods perform in identical conditions. Furthermore, we imaged densely-labeled cells through brain slices of varying thickness, enabling the side-by-side evaluation of different methods in identical conditions with physiological aberrations. Together, these assays revealed that previously proposed AO methods provide only limited correction or in some cases introduced additional aberrations. Careful analysis of the reasons that underlie this limited success enabled us to develop REALM. We demonstrated that REALM can robustly correct aberration levels up to 1 rad RMS in realistic signal and noise levels and using less than 300 acquisitions. Compared to standard imaging (non-AO) and earlier AO methods, REALM detects more molecules and obtains better FRC resolutions.

Next to these idealized samples, we also tested the performance of REALM in stained brain slices. We demonstrated multiplane 3D astigmatic SMLM imaging on βIV-spectrin stained brain sections up to a depth of 50 μm and resolved the periodic structure in 3D. Importantly, we also resolved this structure in a functionally identified pyramidal neuron, demonstrating the feasibility of directly correlating functional studies to nanoscopic organizations. While imaging βIV-spectrin, typ-

ical background levels ranged between 200-300 photons per pixel, resulting in a SBR of around 0.005 (depending on the imaging depth, size of the AIS, and labeling), which is in the range in which REALM can achieve significant correction (see Supplementary Figure 3.A.7).

Beyond 50 μm depth, we found that not the aberration level, but the increase in background fluorescence hampered both aberration correction and localization. In preliminary experiments we noticed that at lower glycerol concentrations (50%), less laser power was required to switch fluorophores to a dark state, which reduced the background levels (to 50 background photons per pixel) at the expense of more spherical aberration and scattering. The best imaging buffer in tissue might therefore depend on the required imaging depth, the abundance of the staining throughout the sample and the number of fluorophores blinking inside the field of view. To further reduce background, light-sheet based illumination could be considered. In addition, the use of cell-specific in vivo knock-in (KI) approaches in brain tissue, such as ORANGE [21], enables tagging endogenous proteins in only a subset of cells (1-10%) within the tissue, thereby further reducing background. We anticipate that REALM can enable 80 or 100 μm deep imaging in tissue when combined with approaches that limit out-of-focus fluorescence by either light-sheet illumination or sparse labeling using an in vivo knock-in approach [21].

REALM can be combined with other z-localization techniques such as PSF engineering [22, 23] or self-interference [24]. Our approach also complements the recently introduced INSPR (In Situ Point Spread function Retrieval) localization method, which demonstrated accurate 3D localization in aberrated conditions when imaging below 20 μm depth [25]. Thus, we anticipate that the open source micromanager plug-in REALM that we provide will enable new avenues for SMLM in deep tissue and facilitate correlative functional and nano-structural research.

3.A Appendix

3.A.1 Methods

Set up

Experiments were performed using a Nikon Ti Eclipse body with a 100X 1.49 NA objective and a quad-band filter cube (containing a ZT405/488/561/640rpc dichroic and ZET405/488/561/640m emission filter, Chroma), to which a MICAO adaptive optics module containing a MIRAO52E (Imagine Optics) deformable mirror was mounted 19 (see Supplementary Figure 3.A.2). Detection is performed with a CMOS camera (Orca Flash v4.0, Hamamatsu). For excitation we used a single mode 647nm laser (140mW, LuxX, Omicron) and 405nm laser (60mW LuxX, Omicron) which can be used for normal widefield and TIRF illumination.

Calibration of the DM

In order to ensure accurate modulation of the Zernike modes, the deformable mirror needs to be properly calibrated. The DM was calibrated by replacing the camera with a Shack-Hartmann sensor (HASO, Imagine Optics) to directly measure the wave-front, using the provided software. A 1 μm bead (TetraSpeck, ThermoFisher, T7282, dilution 1:1000) dried on a coverslip and mounted in glycerol was used as a point source. Mounting in glycerol reduces apodization in the pupil plane due to possible super-critical angle fluorescence, ensuring a homogeneously filled pupil. We blocked other beads in the FOV by placing an iris in the intermediate image plane. The wave-front deformation of each actuator was measured with 10 push-pull cycles to obtain the interaction matrix, which was then converted into the Zernike-based control matrix. We perform this calibration once a year.

The calibration was verified using a phase retrieval algorithm [26] in combination with through-focus scans of 175 nm green fluorescent beads (PS-speck, ThermoFisher, P7220, dilution 1:500) mounted in PBS. This revealed that upon startup the shape of the mirror is imperfect due to thermal drift and needs to be corrected (see Supplementary Figure 3.A.3). The inverse estimated Zernike coefficients from the phase retrieval algorithm were subsequently applied by the mirror, after which a second through-focus scan was acquired. This revealed that this approach was able to correct the complete system within 0.1-0.2 rad RMS (15-30 mλ) wave-front error. Prior to each experiment we performed this calibration step to ensure that the system was properly corrected. Next, we modulated individual Zernike modes and acquired through-focus scans of these PSFs. Phase retrieval indicated that all modes up to the 4th order could be accurately modulated with little crosstalk between Zernike modes (see Supplementary Figure 3.A.3).

DNA-PAINT sample and imaging protocol

Sample chambers were prepared using double sided tape to create two cavities of 10 μl between a microscope slide and a plasma-cleaned #1.5 high-precision cover glass. Next, 10 μl of a solution of BSA-biotin (1 mg/ml in ultra-pure water MQ, Sigma Aldrich, A8549) was incubated for 5 min after being washed with 50 μl washing buffer (1x PBS containing 10 mM MgCl2). 10 μl of streptavidin (1 mg/ml in MQ, Sigma Aldrich, 434302) was then flushed in and incubated for 5 minutes and

washed with washing buffer. Next, biotin conjugated to the complementary DNA-strand P1 (1 mg/ml in MQ) 15 was incubated for 5 minutes and washed away. Finally, washing buffer containing 500 pM of Atto645 conjugated to DNA-strand I1 and green fluorescent beads (PS-speck, ThermoFisher, dilution 1:1000) was flushed in, after which the cavity was sealed with grease and nail polish. The fluorescent beads were used to monitor the stability of the deformable mirror and if needed to correct for thermal drift in between experiments. For each AO correction, a random aberration configuration consisting of Zernike modes $Z_2^{\pm 2}$, $Z_3^{\pm 1}$, $Z_3^{\pm 3}$, Z_4^0, $Z_4^{\pm 2}$ and $Z_4^{\pm 4}$ (11 modes) was induced by the DM. The amplitudes of these modes were chosen uniformly random and normalized to 0.75 rad RMS. Next, the adaptive optics method was performed (see below for implementation details). Afterwards the residual aberration level Wrms was evaluated as

$$W_{\text{rms}} = \sqrt{\sum_{j=1}^{1} 1(A^j_{\text{induced}} - A^j_{\text{estimated}})^2} \tag{3.1}$$

with A^j_{induced} being the induced known Zernike coefficient of Zernike mode j and the A_estimated^j the coefficient of Zernike mode j estimated by the AO method. Prior and during the experiment the signal levels and state of the DM were monitored to ensure equal comparison between these methods (see Supplementary Figure 3.A.1 for experimental details).

Single-molecule acquisition simulations

The single-molecule acquisitions were simulated using a vector PSF model to capture the full complexity of the aberration configurations [27]. Blinking dynamics play a large role in the variability of the metric value and needed to be incorporated in the simulation. We mimicked these blinking dynamics by introducing a variability in the number of emitters in each frame and in the number of photons each emitter emits. The parameters for these distributions corresponded to the experimental signal levels of the DNA-PAINT sample (see Supplementary Figure 3.A.1). The number of emitters per frame was randomly chosen from a Poisson-distribution (with an average of 13 emitters), and the number of photons of each emitter followed an exponential distribution (with an average of 2500 photons). The emitters were randomly positioned with uniform probability across in the field of view (400x400 pixels, 65 nm pixel size) with a uniform background of 20 photons per pixel. Lastly, Poisson noise was added to represent the shot-noise.

The performance of the AO methods was evaluated similar to the procedure described above. Known aberration configurations were induced, followed by AO-based corrections using the different approaches. For comparison with our DNA-PAINT experiment all emitters were placed in focus (z-position = 0 nm) and simulated with a 1.49 NA objective, while for the metric curve and optimization of our method (see Supplementary Figures 3.A.3&3.A.4) the emitters were uniformly random positioned in the z-direction between $\pm$00 nm at a depth of 20 μm with a 1.35 NA silicon immersion objective with refractive index matching. AO methods

Model-based optimization iteratively corrects Zernike modes by applying a sequence of biases of the Zernike mode that is to be corrected. The metric values of

these acquisitions are computed and a metric curve is fitted to find the optimum (see Supplementary Figure 3.A.4). Metric curve fitting was implemented by least-squares fitting with a Gaussian function with an offset (4 fit parameters). The width and center of the fitted Gaussian were constrained to prevent that occasional outliers in the metric values resulted in extreme fit values. The width was constrained to [0.4, 1] rad and the center to [-0.5, 0.5] rad. This greatly improved the performance of the previously proposed method 11 as the noise-sensitive metric M1 often led to extreme fit-values when not constrained. For Figure 3.1, the model-based optimization by Burke et al. was implemented with 11 biases per Zernike mode, whereas REALM used 9 biases per Zernike mode.

The downhill-simplex algorithm uses simplexes (higher dimensional triangles) to find an optimum in the parameter space. We implemented this optimization algorithm via the MATLAB function fmincon with the initial simplex size set to 0.2 rad, which was found to work optimally. Metric M3 was used for all Zernike modes as we did not induce secondary spherical aberration. Therefore, a separate simplex routine with a different metric for primary and secondary spherical aberration as originally proposed 13 could not be implemented. We did not find any reduced correction ability for primary spherical aberration using metric M3. However, we noticed that when correcting more than 4 Zernike modes, the simplex optimization was unable to converge in this larger noisy parameter space. Therefore, optimization was stopped after 300 acquisitions and the state with the best obtained metric value was taken as the estimated correction.

Particle-swarm optimization uses a collection of solutions moving through solution space, where their movement is affected by the individually best solution it found so far, as well as the groups best solution. Particle-swarm optimization was implemented via the MATLAB function particleswarm with a swarm size of 25 as suggested 12 with a maximum of 20 iterations for a maximum of 300 acquisitions. We used an initial swarm spansize of 0.1 rad and a maximum spansize of 0.75 rad. Other settings for particleswarm were set to standard values (InertiaRange, SelfAdjustment and SocialAdjustment set to 1).

COS7 staining

COS-7 cells for Figure 3.2a-e were seeded onto 25 mm coverslips. After 24 hours, cells were pre-extracted with 0.1% glutaraldehyde and 0.2% Triton-X100 in PEM80 (80 mM Pipes, 1 mM EGTA, 4 mM MgCl2, pH 6.8) for one minute. The cells were subsequently fixed with 4% PFA in PEM80 for 10 minutes. After washing in PBS (3x5 min) cells were permeabilized in 0.2% Triton-X100 in PEM80 for 15 minutes. After washing (3x5 min) blocking was performed in 3% BSA in PEM80 for 45 minutes and incubated overnight with a primary antibody against αTub (mouse IgG1, Sigma Aldrich, B-5-1-2, dilution 1:500). The cells were again washed with PBS (3x5 min) and incubated with secondary antibody (goat, anti-Mouse IgG (H+L), AlexaFluor647, Life Technologies, dilution 1:500) for 1 hour at RT. The coverslip was then placed on a microscope slide with the cells facing upwards, after which a 50 or 80 μm thick rat brain section (see below for details) was placed on the coverslip. The surplus of PBS was removed with a tissue and 70 μl of glycerol blinking buffer (see below) was deposited on the slice. Next, a 25 mm #1.5 high precision coverslip

was placed on top of the slice and the assembly was sealed with nail polish. For the blinking buffer 10 μl of 1M MEA, together with 2,5 μl of 20% glucose and 1 μl of gloxy buffer (70 mg/ml glucose oxidase, 4 mg/ml catalase in MQ), were mixed with 86 μl of a mixture of 95% glycerol and 5% Tris 20 mM, pH 8.0.

Slice preparation and βIV-spectrin staining

All animal experiments were performed in compliance with the European Communities Council Directive 2010/63/EU effective from 1 January 2013. They were evaluated and approved by the national CCD authority (license AVD8010020172426) and by the Royal Netherlands Academy of Arts and Science (KNAW) animal welfare and ethical guidelines and protocols (IvD NIN 17.21.01 and 19.21.11). To obtain sections with a fixed thickness (Figure 3.1a-e), adult rats were deeply anaesthetized by an i.p. injection of pentobarbital (50 mg/kg) and transcardially perfused with PBS and 4% PFA. The brains were removed and post-fixed in PFA for 24 hours after which the tissue was stored in PBS. Coronal sections of 50 μm thick were cut on a vibratome (VT1200S, Leica Microsystems).

For βIV-spectrin staining (Figure 3.3&3.4 and Supplementary Figures 3.A.11& 3.A.13), adult rats were deeply anaesthetized by 3% isoflurane inhalation and decapitated, after which the brains were moved to ice-cold artificial cerebral spinal fluid containing (in mM): 125 NaCl, 3 KCl, 25 glucose, 25 NaHCO3, 1.25 Na2H2PO4, 1 CaCl2, 6 MgCl2, saturated with 95% O2 and 5% CO2 (pH 7.4). 300-400 μm thick parasagittal brain sections containing the primary somatosensory cortex were cut on a vibrotome (1200S, Leica Microsystems). Following a recovery period at 35 °C for 35-45 minutes slices were stored at room temperature in the ACSF. For whole-cell filling with biocytin (Figure 3.4), the slice was transferred to a customized upright microscope (BX51WI, Olympus Nederland BV). The microscope bath was perfused with oxygenated (95% O2, 5% CO2) ACSF consisting of (in mM): 125 NaCl, 3 KCl, 25 glucose, 25 NaHCO3, 1.25 Na2H2PO4, 2 CaCl2, and 1 MgCl2. Patch pipettes were pulled from borosilicate glass (Harvard Apparatus, Edenbridge, Kent, UK) pulled to an open tip of 3 – 6 MΩ resistance. The intracellular solution contained (in mM): 130 K-Gluconate, 10 KCl, 4 Mg-ATP, 0.3 Na2-GTP, 10 HEPES, 10 Na2-phosphocreatine and 5 mg ml^{-1} biocytin (pH 7.25 adjusted with KOH, 280 mOsmol kg^{-1}). An Axopatch 200B (Molecular Devices) was used to obtain whole-cell configuration. The cell was left to fill for 30 min, during which the bridge balance was monitored and stayed below 15 mλ. Slices were fixed in 4% PFA (20 minutes) and blocked with 5% NGS and 2% Triton (2 hours) before incubation with rabbit anti-βIV-spectrin antibody in blocking buffer (1:1000, 24 hours, gift from M. Engelhardt). Slices were washed (3x15 minutes), incubated with goat anti-rabbit Alexa 647 (1:500 or 1:1000, 2 hours, ThermoFisher) and in the case of biocytin filling, with Streptavidin Alexa-488 conjugate (1:500, Invitrogen) and washed again. During all steps, the slices were at room temperature and on a shaker. The slices were stored in PBS (4°C). Before imaging, slices were incubated for at least 15 minutes in 95% glycerol and 5% Tris 20 mM after which they were mounted between a microscope slide and #1.5 high precision coverslip with two 120 μm spacers (Secure-Seal Spacer, Thermofisher, S24735) in the blinking buffer described above.

Direct comparison between REALM and Mlodzianoski et al.
We first performed both correction methods and performed SMLM while switching between mirror states during the acquisition every 500 frames. Mlodz. (as published) indicates the implementation as published, including a separate simplex routine with a different metric for primary and secondary spherical aberration, after which a secondary simplex routine corrects astigmatism and coma. Mlodz. (extended) denotes the method as published, except that trefoil and secondary astigmatism are also included in the second simplex routine. REALM was implemented as in Supplementary Figure 3.A.9.

SMLM detection, localization and reconstruction
The detection, localization and reconstruction was performed with the ImageJ plugin DoM (Detection of Molecules) [28] (see). DoM detects single molecules events by convolving images with a combination of a Gaussian and Mexican hat kernel. Localization is performed by an unweighted nonlinear 2D Gaussian fit with Levenberg–Marquardt optimization. The detection PSF size was set to 150 nm. Localizations with a width larger than 130% of this size (195 nm) are regarded as false positives. A localization is classified as successful if it is non-false positive and has a positive integrated intensity. SMLM reconstructions were rendered by plotting each molecule as a 2D or 3D Gaussian with standard deviations in each dimension equal to the corresponding localization errors. For astigmatic 3D localization the z-position was estimated from the difference in x- and y-width of the spot, where we corrected for depth-induced loss of astigmatism 19 using a simulated required astigmatism level at each depth (see Supplementary Figure 3.A.13e-f). Drift was corrected by 2D cross-correlation of intermediate reconstructions consisting of 500 or 1000 frames. The FRC resolution was computed by splitting the localizations in two batches every other 500 frames. The corresponding reconstructions where then used the calculate the FRC resolution using the ImageJ Fourier Ring Correlation plugin.

REALM
REALM (Robust and Effective Adaptive optics in Localization Microscopy) is a free open-source Micro-Manager plugin (github.com/MSiemons/REALM [29]) where the method described in this work is implemented (see Supplementary Figure 3.4). It offers a compact and intuitive user interface suitable for non-experts. It currently supports two types of DMs: MIRAO52E (Image Optics) and DMH40-P01 (Thorlabs, see github.com/ HohlbeinLab/Thorlabs_DM_Device_Adapter for the device adapter) and we encourage others to build device adapters for other DM manufacturers to interface with REALM. The Fourier transform needed for the metric evaluation is implemented via the 2D Fast Hartley Transform (FHT), where the image is padded with the mode value of the acquisition to a size of 2n x 2n (with n in integer), usually resulting in a size of 256 x 256 or 512 x 512. All aberration corrections for Figure 3.2 and 3.3 are performed with REALM.

Acknowledgements
The authors thank Alard Mosk, Giulia Sereni and Ivo Vellekoop for useful discussion on aberration in brain tissue, Roderick Tas and Chiung-Yi Chen for help with the DNA-PAINT assays and Audrius Jasaitis (Imagine Optic) for help in controlling the Deformable Mirror. This work was funded by the Dutch Research Council (NWO) through the FOM program Neurophotonics.

3.A.2 Supplementary figures

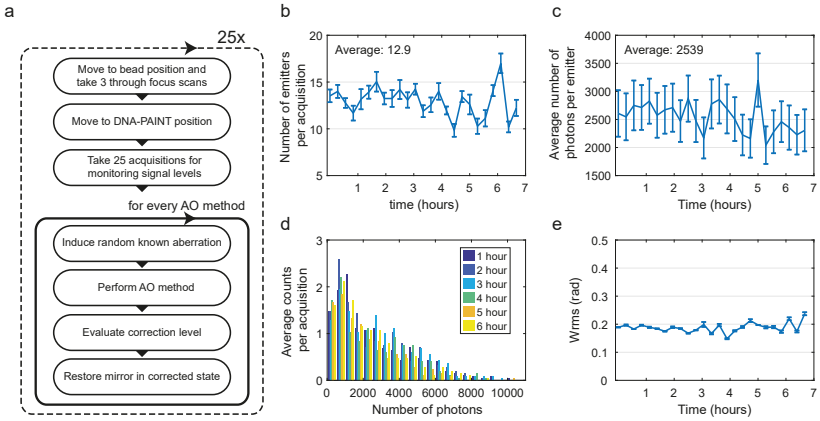

Figure 3.A.1: DNA-PAINT sample and deformable mirror remain stable during the experiment of Figure 3.1f. a) Schematic of the experimental procedure, consisting of a monitoring part (first 3 blocks) and a correction part (bottom 4 blocks). Prior to a series of AO corrections, the stage moves to a position with a bead and acquires 3 through-focus scan. Next, 25 frames were acquired at the DNA-PAINT position (without a bead in the FOV) with the system-corrected DM state. From these acquisitions the number of emitters (b), number of photons per emitter (c) and distribution of photon counts were measured (d). This revealed that the signal levels remained constant for the full 7 hour duration of the experiment. The acquired through-focus scans (in system corrected state) are analyzed with a phase retrieval algorithm 25 to check for possible drift in the mirror. The aberration level (e) remained at a level of 0.2 rad RMS during the whole experiment. Error bars indicate the standard error of mean in the number of emitters (b), number of photons (c) of the 25 frames and estimated aberration level (e).

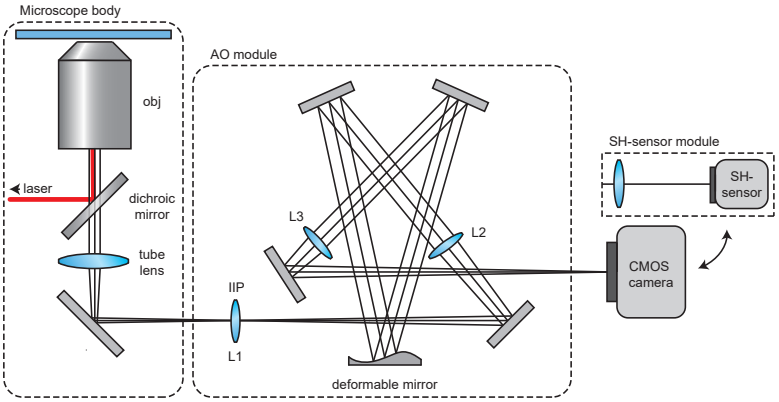

Figure 3.A.2: Illustration of the set up. The AO module consists of a 4F system (lenses L2 and L3, f = 500 mm), where the deformable mirror (DM) is placed in the back focal plane of L2. Another lens (L1, f = 750 mm) is placed in the intermediate image plane (IIP), which conjugates the pupil plane of the objective to the DM. This lens is needed as the tube lens and objective inside the microscope body are placed approximately 5 cm too close to each other to form a 4F system. For calibration of the DM, the CMOS camera is replaced with the SH-sensor module, which consists of a lens (f = 100 mm) and a Shack-Hartman sensor.

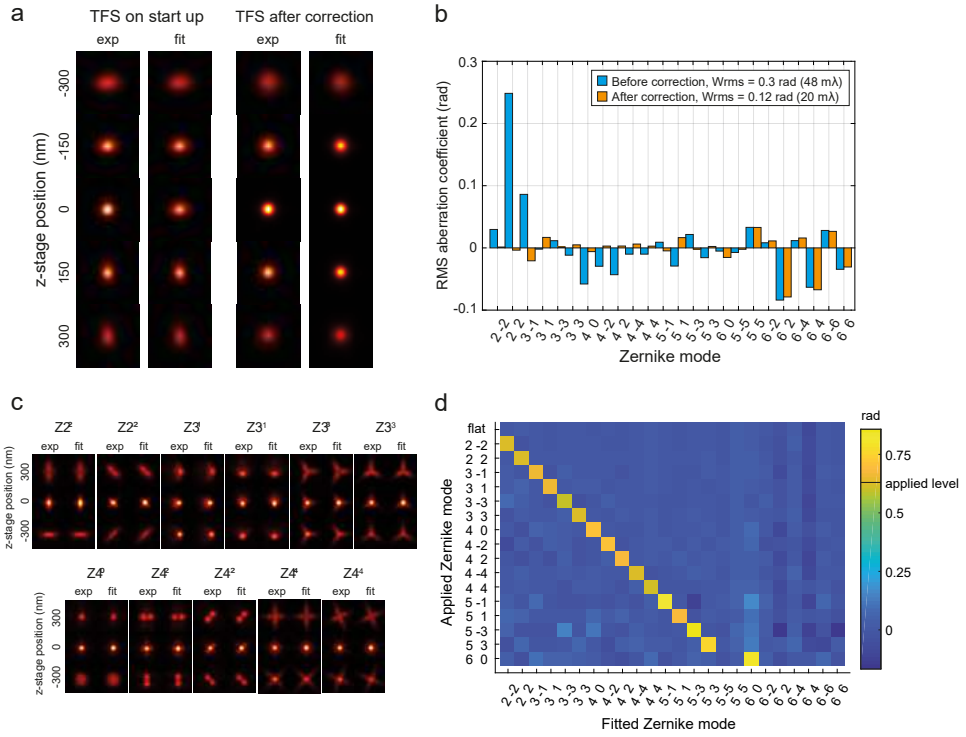

Figure 3.A.3: Verification of the DM-calibration. a) On start-up the experimental PSF (exp) is aberrated due to drift in the deformable mirror. A phase retrieval algorithm (fit) (see methods) estimated the specific Zernike modes as shown in (b). The inverse Zernike coefficients of modes $Z_2^{\pm 2}$, $Z_3^{\pm 1}$, $Z_3^{\pm 3}$, Z_4^0, $Z_4^{\pm 2}$, $Z_4^{\pm 4}$, $Z_5^{\pm 1}$, $Z_5^{\pm 3}$ and Z_6^0 were subsequently applied by the mirror, which improves the PSF (TFS after correction). Phase retrieval revealed that all major contributing Zernike modes were nullified. c) PSFs and phase retrieval fits corresponding to Zernike modes $Z_2^{\pm 2}$, $Z_3^{\pm 1}$, $Z_3^{\pm 3}$, Z_4^0, $Z_4^{\pm 2}$, $Z_4^{\pm 4}$ with an amplitude of 0.63 rad (100 mλ). d) phase retrieval of (c) revealed that this DM is capable of accurately modulating Zernike modes up to the fourth order with little crosstalk. Higher order modes such as $Z_5^{\pm 1}$, $Z_5^{\pm 3}$ and Z_6^0 appear to have crosstalk with lower modes.

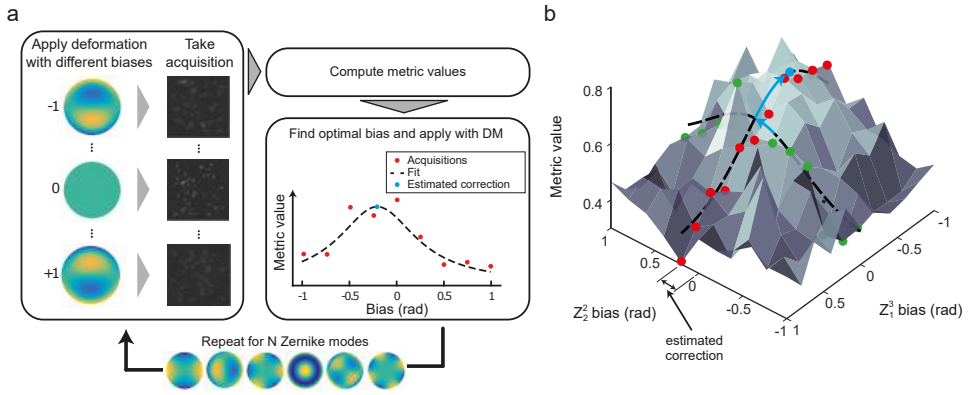

Figure 3.A.4: Schematic of model-based optimization. a) For each Zernike mode a series of frames is acquired with different biases (amplitude of the Zernike mode). From these acquisitions the metric value is computed. Next, the optimal bias is determined by fitting an appropriate function (the metric curve) to these points, after which the estimated correction is applied. This is performed for multiple Zernike modes. b) The optimum correction for Zernike modes can be more easily estimated when the contrast in metric value is improved. Therefore it is beneficial to first correct major expected types of aberrations, such as spherical aberration. For the same reason, multiple correction rounds also yield additional improvement.

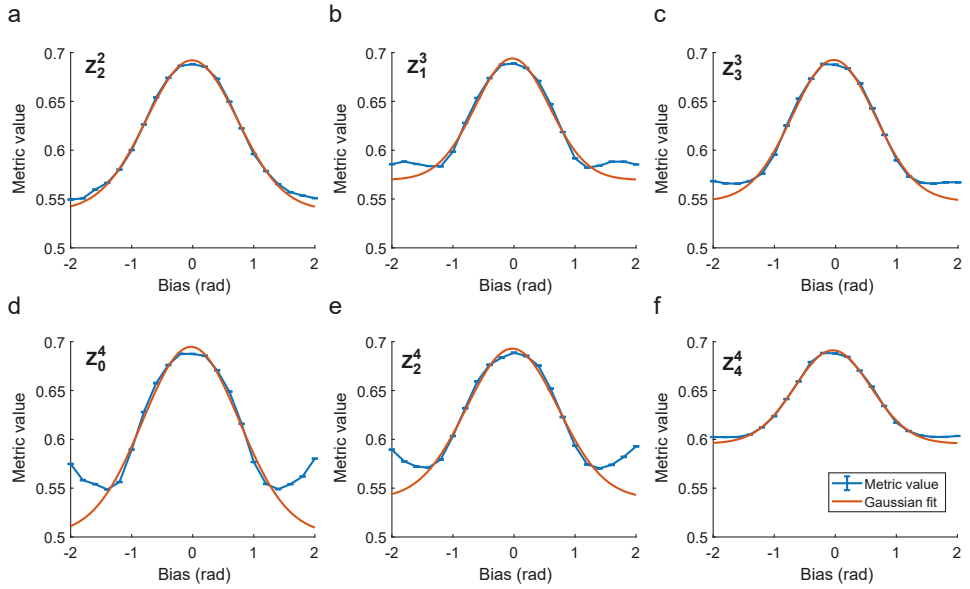

Figure 3.A.5: Metric curves for different Zernike modes. a-f) Metric value as function of applied bias for different Zernike modes. These values were obtained by simulating single-molecule acquisitions (see methods) with different biases for each Zernike mode. A Gaussian function with offset properly describes the metric values to all Zernike modes up to the 4th order in a ± 1 rad range and was therefore used as the metric curve. Increasing the bias beyond ± 1.5 rad results in an increase in the metric value for some Zernike modes. This inversion of the metric value occurs due to contrast inversion at (specific) spatial frequencies.

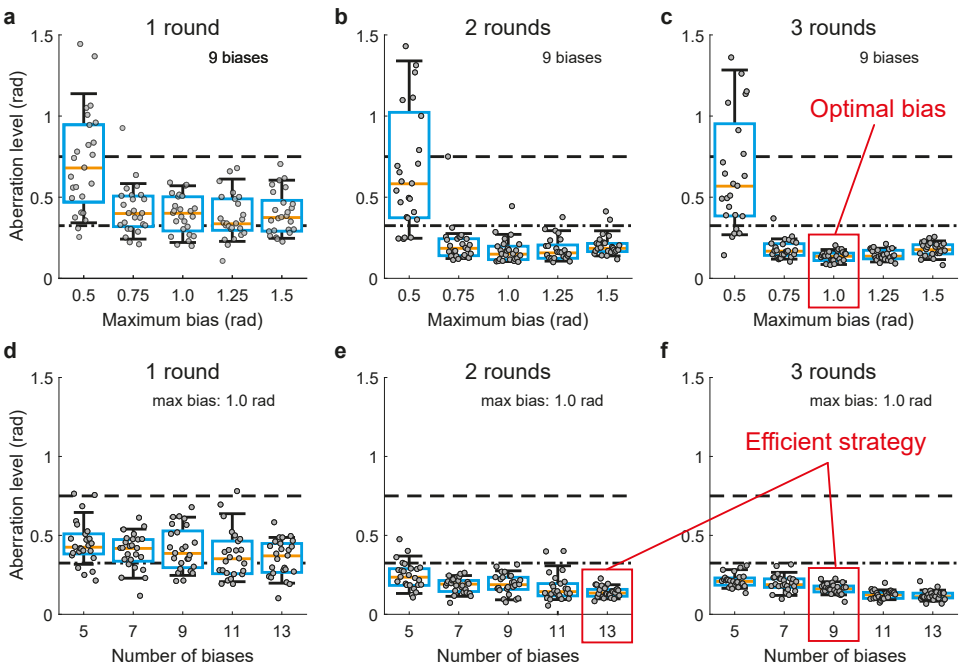

Figure 3.A.6: Simulation-based optimization of REALM. a-c) residual aberration level for different maximum applied biases and correction rounds, using 9 biases per Zernike mode (11 Zernike modes in total). Dashed line indicates induced aberration level (0.75 rad RMS). Residual aberrations are minimal when using a bias of 1 rad. d-f) Residual aberration level for different number of biases and correction rounds. Approaches with 13 biases in 2 correction rounds (total of 286 acquisitions for 11 Zernike modes) or 9 biases in 3 correction rounds (total 297 acquisitions for 11 Zernike modes) both constitute efficient strategies to achieve robust correction. All simulations contain 25 random aberration configurations (n = 25) for each optimization configuration. Box plot indicates 9/91-percentile, 25/75-percentile and median.

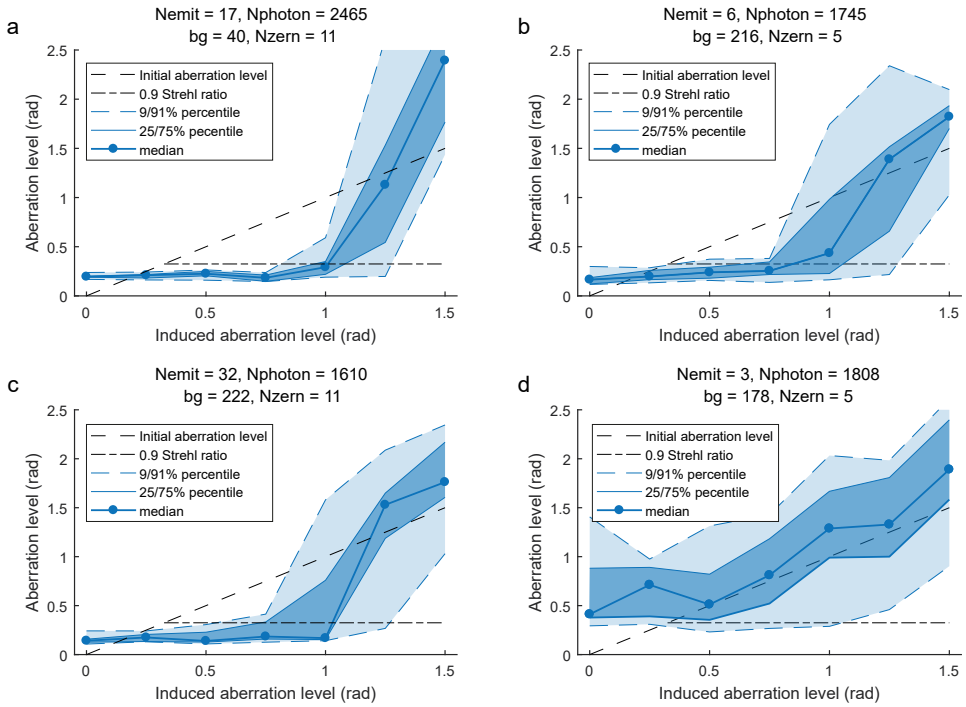

Figure 3.A.7: Experimental performance of REALM as function of induced aberration level using a DNA-PAINT sample in different signal to background ratio's (SBR). Here 2 correction rounds with 13 biases per Zernike mode with a maximum bias of 1 rad is used. For each aberration level, 10 random aberration configurations were induced by the deformable mirror and subsequently corrected. Results below the initial aberration level (dashed line) indicate improvement, results below 0.9 Strehl-ratio (dashed-dotted line) indicate proper imaging conditions. For (a) and (b) these aberration configurations consisted of 11 Zernike modes (astigmatism, coma, primary spherical aberration, trefoil, second order astigmatism and quadrafoil) and for (c) and (d) these consisted of 5 Zernike modes (astigmatism, coma and primary spherical aberration). The measured total signal to background ratio (SBR) was 0.0065 (a), 0.0015 (b), 0.0003 (c) and 0.0002 (d). The signal and background level are estimated from 25 pre-acquisitions before an aberration is induced. Nemit, Nphoton, bg and Nzern indicate the average number of emitters per frame, the average number of emitted photons of each emitter, the background photon count and the number of applied Zernike modes present in the aberration configuration. Error bands indicate 9/91% and 25/75% percentile in all panels. REALM was capable of correcting up to 1 rad RMS of wave-front error when the aberration was completely random for all but the lowest SBR. In practice, a major contribution is due to spherical aberration, which can be roughly pre-corrected, significantly increases the aberration level which can be corrected by REALM.

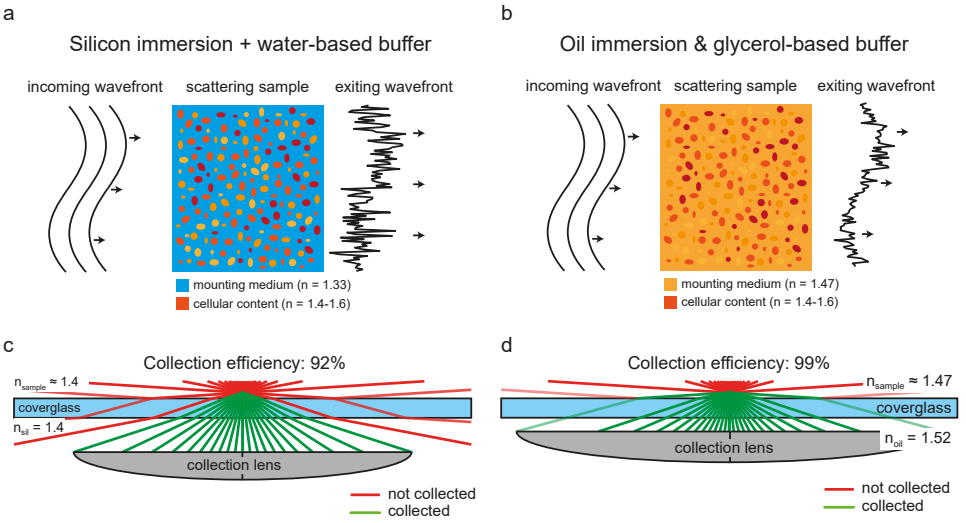

Figure 3.A.8: a) Experimental procedure for comparing SMLM with and without adaptive optics. First, the mirror was used to correct all system induced aberrations using a bead sample (see Supplementary Figure 3.A.2). This mirror state was saved and later used as the system-corrected DM state. For the 80 μm slice we pre-corrected spherical aberration by applying this mode with an amplitude of 100 nm (0.9 rad) (RMS normalized amplitude). Next, the sample was mounted and focused using widefield imaging, while trying to keep the illumination minimal. Subsequently, the laser power was increased to initiate the blinking and spherical aberration was corrected, followed by the other Zernike modes. After correction the mirror state was saved as sample-corrected state and the SMLM acquisition was started. During this acquisition the mirror switches between the system- or Z40 pre-corrected and sample-corrected state every 500 frames. b) SMLM reconstruction of microtubules in COS-7 cells imaged through a 50 μm thick brain section using the frames with the DM in system-corrected state (without AO). Image contains a total of 34K successful localizations with a localization precision <20 nm. c) SMLM reconstruction of b) using frames with sample-corrected DM state. The estimated aberration level was 0.81 $\pm$0.02 rad RMS and 123K events were successfully localized with a precision <20 nm. d&e) Another example as b&c, consisting of 17K localizations (without AO) and 53K localizations (with AO) with a localization precision <20 nm. Estimated aberration level was 1.07$\pm$0.08 rad RMS. f) SMLM reconstruction of microtubules in COS-7 cells imaged through a 80 μm thick brain section using the frames with a precorrection of spherical aberration (35K localizations with a localization precision <20 nm). g) as (f) but with frames with the DM in sample corrected state (79K localizations with a localization precision <20 nm). Estimated aberration level was 0.91$\pm$0.04 rad RMS (on top of 0.9 rad pre-corrected spherical aberration). Repeated n=10 times in 3 distinct samples with similar results.

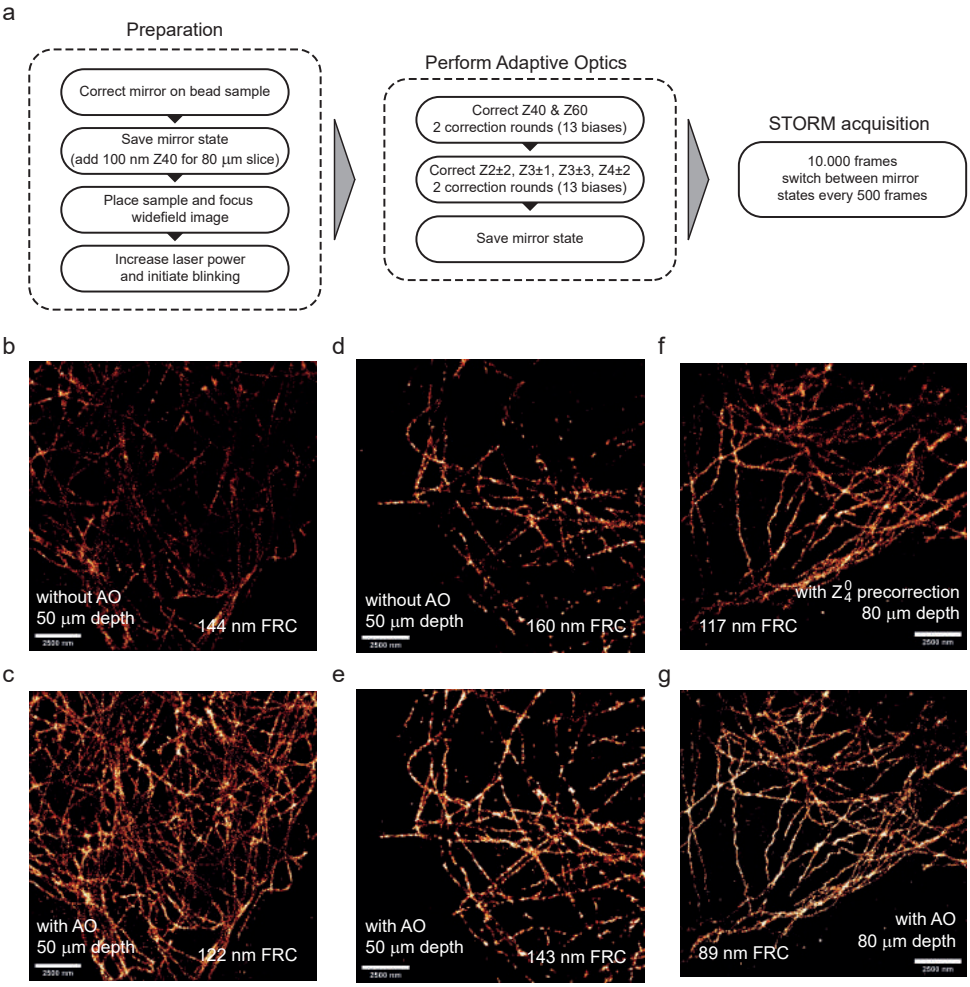

Figure 3.A.9: Illustration of the effect of a high refractive index buffer and objective choice. a) When using a water-based buffer the subcellular content of the tissue (organelles, DNA) has a large refractive index mismatch with the buffer. This rapid local change in refractive index drowns the gradually aberrated wave-front, thereby rendering AO less useful. b) By mounting the sample in a higher refractive index buffer using glycerol, the subcellular content causes less scattering and AO becomes more useful. c) A silicon immersion lens is the objective of choice when using a water buffer as the average refractive index of (brain) tissue is around 1.4. This matches the refractive index of the silicon oil, minimizing sample induced spherical aberration. However, the collection efficiency is only 92% as the largest available NA (1.35) is smaller than the refractive index. d) The glycerol-based buffer increases the average to around 1.48 (assuming a water content of 70%, which is replaced by the glycerol blinking buffer). Therefore a 1.49 NA oil immersion lens has a smaller refractive index mismatch than silicon oil and a higher collection efficiency as it collects the complete 2π sr solid angle and is therefore the objective of choice. For the computation of the collection efficiency we incorporated the Fresnel reflection at each interface.

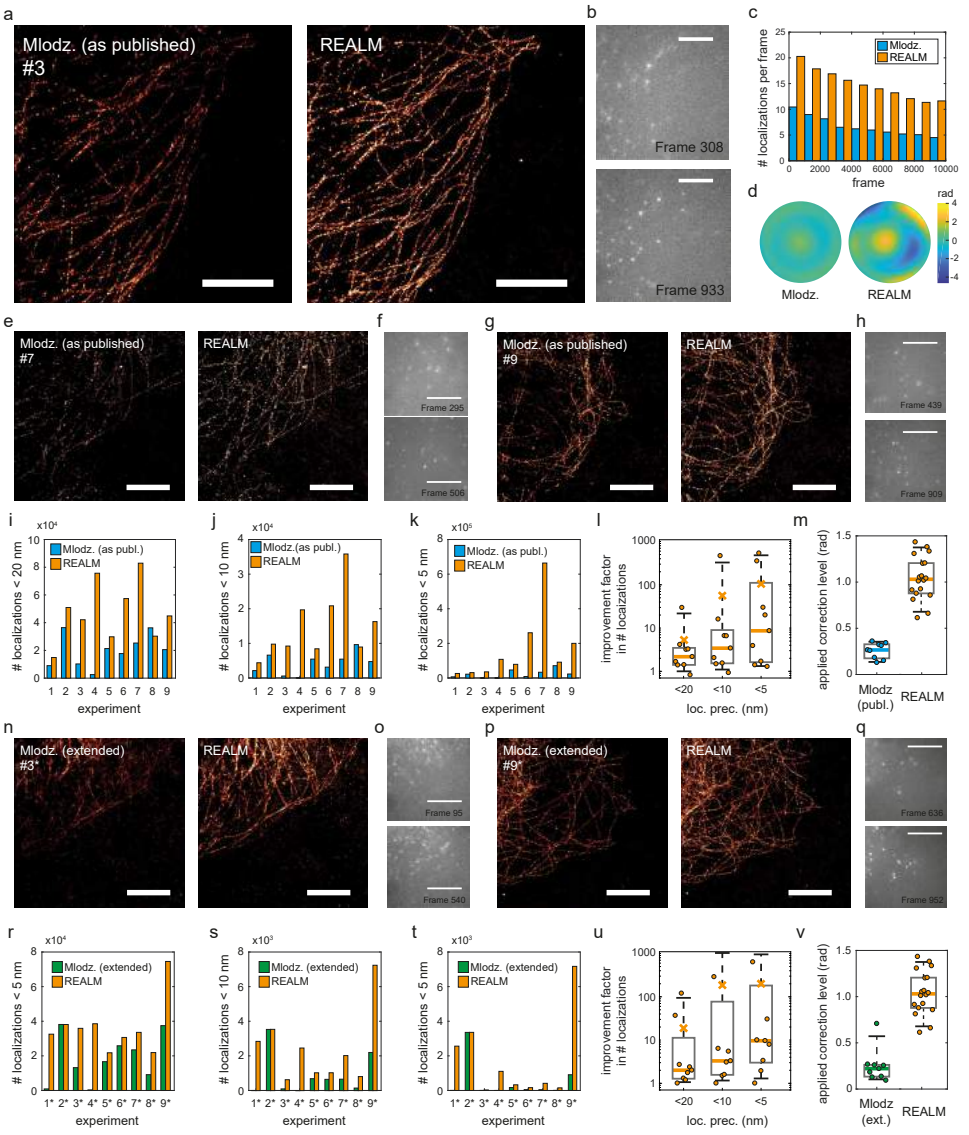

Figure 3.A.10: Direct comparison between the method proposed by Mlodzianoski et al. (here shortened to Mlodz.) and REALM by imaging COS-7 cells through 60 μm thick slices (2x9 experiments). a) Reconstruction of Mlodz. (as published) and REALM for experiment # 3. b) Representative single acquisition for Mlodz. and REALM corresponding to (a). Spots appear more confined and round with REALM. c) Average number of localization per frame for Mlodz. and REALM for (a). d) Estimated wave-front by Mlodz. (Wrms = 0.36 rad) and REALM (Wrms = 1.3 rad) for (a). e-h) Same as (a,b) but for experiment # 7 & # 9. i-k) Total number of successful localizations with a localization precision below 20 nm, 10 nm and 5 nm resp. for Mlodz. (as published) compared to REALM. l) Improvement factor in the number of localizations below 20 nm (2.2x, median), 10 nm (3.4x, median), and 5 nm (8.6x, median) with REALM compared to Mlodz. (as published). m) Applied correction level for Mlodz. (as published), Mlodz. (extended) and REALM. REALM applies a larger correction, indicating that simplex optimization remains in a noise induced local minimumn-u) Same as (e-l) but with Mlodz. (extended). v) Box plot of the calculated FRC of Mlodz. as published (151 nm median), Mlodz. Extended (145) and REALM (122 nm). All experiments were performed on three distinct samples. All scale bars indicate 5 μm. Box plots (l,m,u,v) indicate 9/91-percentile, 25/75-percentile and median. Reconstruction pairs are shown with the same contrast.

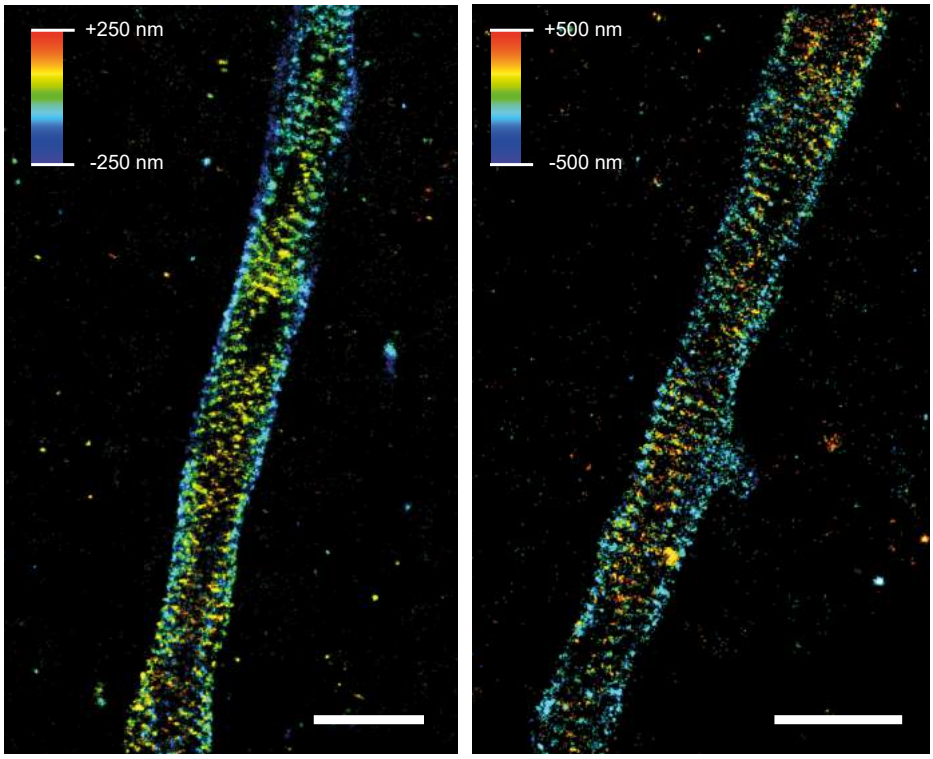

Figure 3.A.11: Example 3D SMLM reconstructions of βIV-spectrin in the AIS of layer 5 axons at a depth of 40 μm (a) and 50 μm (b). Scalebar indicates 2 μm. Repeated n=12 times in 4 distinct samples with similar results.

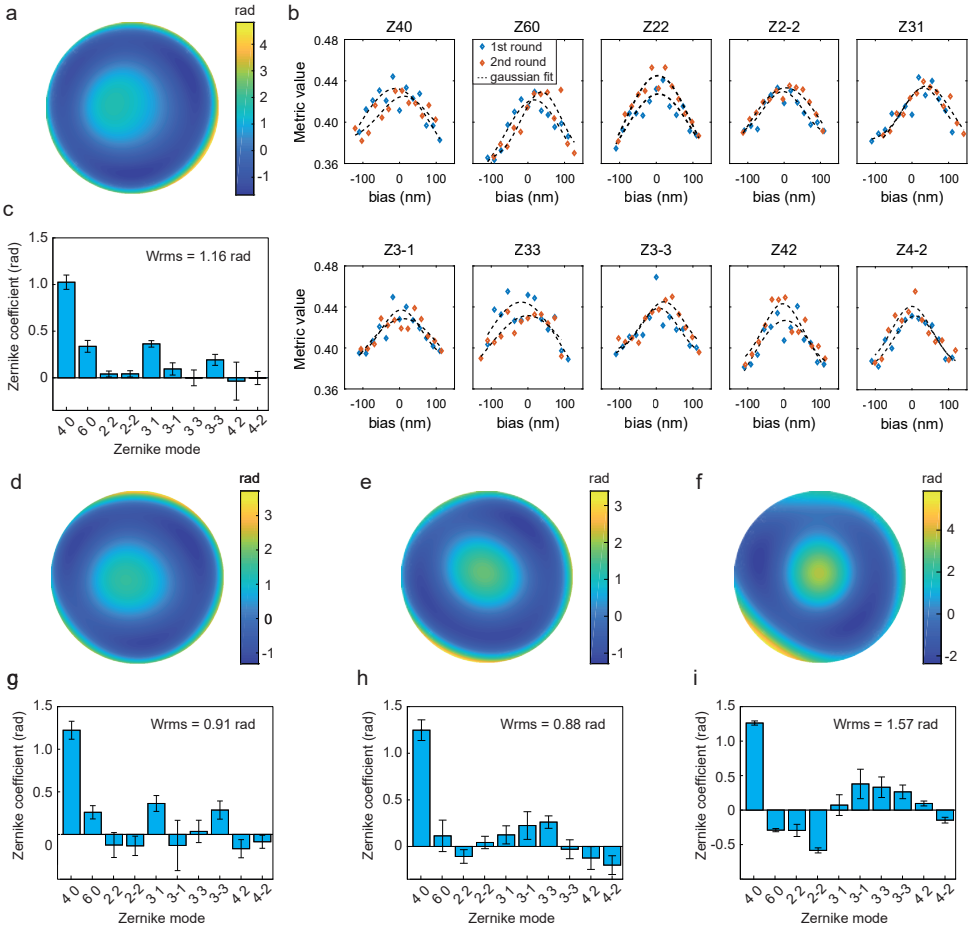

Figure 3.A.12: Estimated aberrations by REALM. a) Aberration profile corresponding to the βIV-spectrin reconstruction of Figure 3.3. b) Metric values and Gaussian fits of (a) of the model-based optimization algorithm of REALM. c) Estimated Zernike coefficients of (a) and (b). Error bars indicate the standard deviation based on the goodness of fit to the metric values. d-f) Aberration profiles corresponding to βIV-spectrin reconstructions of Supplementary Figure 3.A.11(a,b) and Figure 3.2 resp. g-i) Estimated Zernike coefficients of (d-f), respectively. Error bars indicate the standard deviation based on the goodness of fit to the metric values.

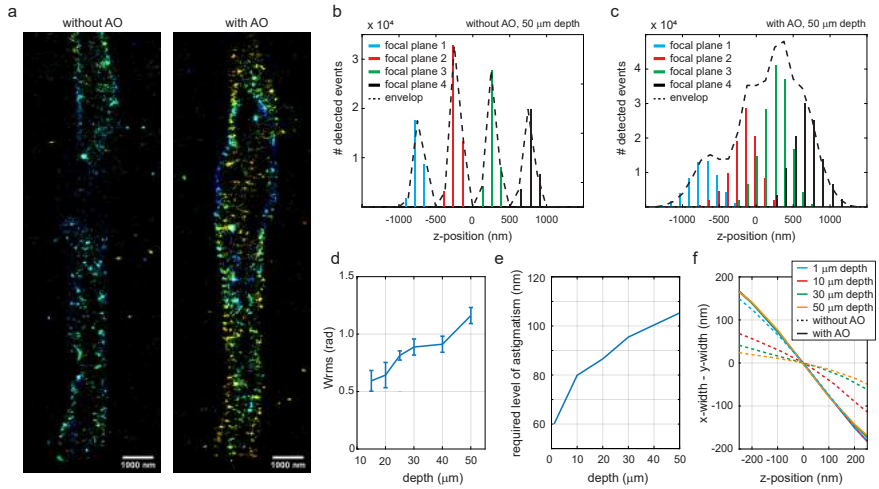

Figure 3.A.13: REALM improves 3D multiplane astigmatic SMLM. a) SMLM reconstruction of a single-plane astigmatic imaging experiment using βIV-spectrin at a depth of 50 μm. Every 500 frames the DM state was switched to system-corrected (without AO, 100 nm FRC) and sample-based correction (with AO, 76 nm FRC) (repeated n=3 times with similar results). b) Due to spherical aberration, the ellipticity of the PSF and therefore the z-encoding is lost without AO. This prevents multiplane astigmatic SMLM reconstructions to be 'stitched' together. c) Using REALM for aberration correction, z-encoding is restored allowing for 3D multiplane astigmatic SMLM. d) Measured aberration level using REALM on βIV-spectrin stained slices at different depths. Data comprised of estimated aberration levels in 3 samples. Error bars indicate standard deviation of REALM. Correction was performed once (n=1). e) Required level of astigmatism to maintain a similar calibration curve for astigmatic z-encoding, based on PSF simulations 19 and a refractive index of 1.48. f) Theoretical calibration curve with and without AO with astigmatism levels of (e) as a function of depth. Without AO the ellipticity of lost, resulting in failure of 3D multiplane astigmatic SMLM as shown in (b).

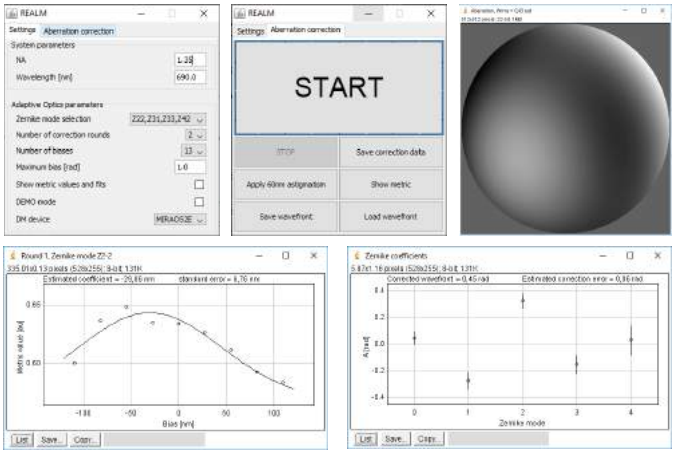

Figure 3.A.14: Images of the open-source Micro-Manager plugin REALM (28). Relevant parameters can be tuned (Zernike modes, number of biases, maximum bias, number of correction rounds). REALM requires only little input parameters (NA and wavelength), resulting in a clear and user-friendly interface.

References

[1] M. E. Siemons, N. A. Hanemaaijer, M. H. Kole, and L. C. Kapitein, *Robust adaptive optics for localization microscopy deep in complex tissue,* Nat Commun **12**, 1 (2021).

[2] M. J. Rust, M. Bates, and X. Zhuang, *Sub-diffraction-limit imaging by stochastic optical reconstruction microscopy (storm),* Nat Methods **3**, 793 (2006).

[3] E. Betzig, G. H. Patterson, R. Sougrat, O. W. Lindwasser, S. Olenych, J. S. Bonifacino, M. W. Davidson, J. Lippincott-Schwartz, and H. F. Hess, *Imaging intracellular fluorescent proteins at nanometer resolution,* Science **313**, 1642 (2006).

[4] S. T. Hess, T. P. Girirajan, and M. D. Mason, *Ultra-high resolution imaging by fluorescence photoactivation localization microscopy,* Biophys J **91**, 4258 (2006).

[5] K. Xu, G. Zhong, and X. Zhuang, *Actin, spectrin, and associated proteins form a periodic cytoskeletal structure in axons,* Science **339**, 452 (2013).

[6] C. Leterrier, J. Potier, G. Caillol, C. Debarnot, F. Rueda Boroni, and B. Dargent, *Nanoscale architecture of the axon initial segment reveals an organized and robust scaffold,* Cell Rep **13**, 2781 (2015).

[7] Y. Hou, I. Jayasinghe, D. J. Crossman, D. Baddeley, and C. Soeller, *Nanoscale analysis of ryanodine receptor clusters in dyadic couplings of rat cardiac myocytes,* J Mol Cell Cardiol **80**, 45 (2015).

[8] J. P. Heller, T. Odii, K. Zheng, and D. A. Rusakov, *Imaging tripartite synapses using super-resolution microscopy,* Methods **174**, 81 (2020).

[9] L. Barna, B. Dudok, V. Miczan, A. Horvath, Z. I. Laszlo, and I. Katona, *Correlated confocal and super-resolution imaging by vividstorm,* Nat Protoc **11**, 163 (2016).

[10] S. Liu, H. Huh, S. H. Lee, and F. Huang, *Three-dimensional single-molecule localization microscopy in whole-cell and tissue specimens,* Annu Rev Biomed Eng (2020), 10.1146/annurev-bioeng-060418-052203.

[11] M. Booth, D. Andrade, D. Burke, B. Patton, and M. Zurauskas, *Aberrations and adaptive optics in super-resolution microscopy,* Microscopy (Oxf) **64**, 251 (2015).

[12] D. Burke, B. Patton, F. Huang, J. Bewersdorf, and M. J. Booth, *Adaptive optics correction of specimen-induced aberrations in single-molecule switching microscopy,* Optica **2**, 177 (2015).

[13] K. F. Tehrani, Y. Zhang, P. Shen, and P. Kner, *Adaptive optics stochastic optical reconstruction microscopy (ao-storm) by particle swarm optimization,* Biomed Opt Express **8**, 5087 (2017).

[14] M. J. Mlodzianoski, P. J. Cheng-Hathaway, S. M. Bemiller, T. J. McCray, S. Liu, D. A. Miller, B. T. Lamb, G. E. Landreth, and F. Huang, *Active psf shaping and adaptive optics enable volumetric localization microscopy through brain sections,* Nat Methods **15**, 583 (2018).

[15] M. J. Booth, *Adaptive optics in microscopy,* Philos Trans A Math Phys Eng Sci **365**, 2829 (2007).

[16] J. Schnitzbauer, M. T. Strauss, T. Schlichthaerle, F. Schueder, and R. Jungmann, *Super-resolution microscopy with dna-paint,* Nat Protoc **12**, 1198 (2017).

[17] A. Facomprez, E. Beaurepaire, and D. Debarre, *Accuracy of correction in modal sensorless adaptive optics,* Opt Express **20**, 2598 (2012).

[18] A. Edelstein, N. Amodaj, K. Hoover, R. Vale, and N. Stuurman, *Computer control of microscopes using micromanager,* Curr Protoc Mol Biol **Chapter 14**, Unit14 20 (2010).

[19] G. J. Stuart, H. U. Dodt, and B. Sakmann, *Patch-clamp recordings from the soma and dendrites of neurons in brain slices using infrared video microscopy,* Pflugers Arch **423**, 511 (1993).

[20] M. Siemons, B. M. C. Cloin, D. M. Salas, W. Nijenhuis, E. A. Katrukha, and L. C. Kapitein, *Comparing strategies for deep astigmatism-based single-molecule localization microscopy,* Biomed Opt Express **11**, 735 (2020).

[21] J. Willems, A. P. H. de Jong, N. Scheefhals, E. Mertens, L. A. E. Catsburg, R. B. Poorthuis, F. de Winter, J. Verhaagen, F. J. Meye, and H. D. MacGillavry, *Orange: A crispr/cas9-based genome editing toolbox for epitope tagging of endogenous proteins in neurons,* PLoS Biol **18**, e3000665 (2020).

[22] S. R. Pavani, M. A. Thompson, J. S. Biteen, S. J. Lord, N. Liu, R. J. Twieg, R. Piestun, and W. E. Moerner, *Three-dimensional, single-molecule fluorescence imaging beyond the diffraction limit by using a double-helix point spread function,* Proc Natl Acad Sci U S A **106**, 2995 (2009).

[23] Y. Shechtman, S. J. Sahl, A. S. Backer, and W. E. Moerner, *Optimal point spread function design for 3d imaging,* Phys Rev Lett **113**, 133902 (2014).

[24] P. Bon, J. Linares-Loyez, M. Feyeux, K. Alessandri, B. Lounis, P. Nassoy, and L. Cognet, *Self-interference 3d super-resolution microscopy for deep tissue investigations,* Nat Methods **15**, 449 (2018).

[25] F. Xu, D. Ma, K. P. MacPherson, S. Liu, Y. Bu, Y. Wang, Y. Tang, C. Bi, T. Kwok, A. A. Chubykin, P. Yin, S. Calve, G. E. Landreth, and F. Huang, *Three-dimensional nanoscopy of whole cells and tissues with in situ point spread function retrieval,* Nat Methods **17**, 531 (2020).

[26] M. Siemons, C. N. Hulleman, R. O. Thorsen, C. S. Smith, and S. Stallinga, *High precision wavefront control in point spread function engineering for single emitter localization,* Opt Express **26**, 8397 (2018).

[27] S. Stallinga and B. Rieger, *Accuracy of the gaussian point spread function model in 2d localization microscopy,* Opt Express **18**, 24461 (2010).

[28] A. Chazeau, E. A. Katrukha, C. C. Hoogenraad, and L. C. Kapitein, *Studying neuronal microtubule organization and microtubule-associated proteins using single molecule localization microscopy,* Neuronal Cytoskeleton, Motor Proteins, and Organelle Trafficking in the Axon **131**, 127 (2016).

[29] M. E. Siemons and L. C. Kapitein, *Robust adaptive optics for localization microscopy deep in complex tissue,* REALM (2021), https://doi.org/10.5281/zenodo.4716044.

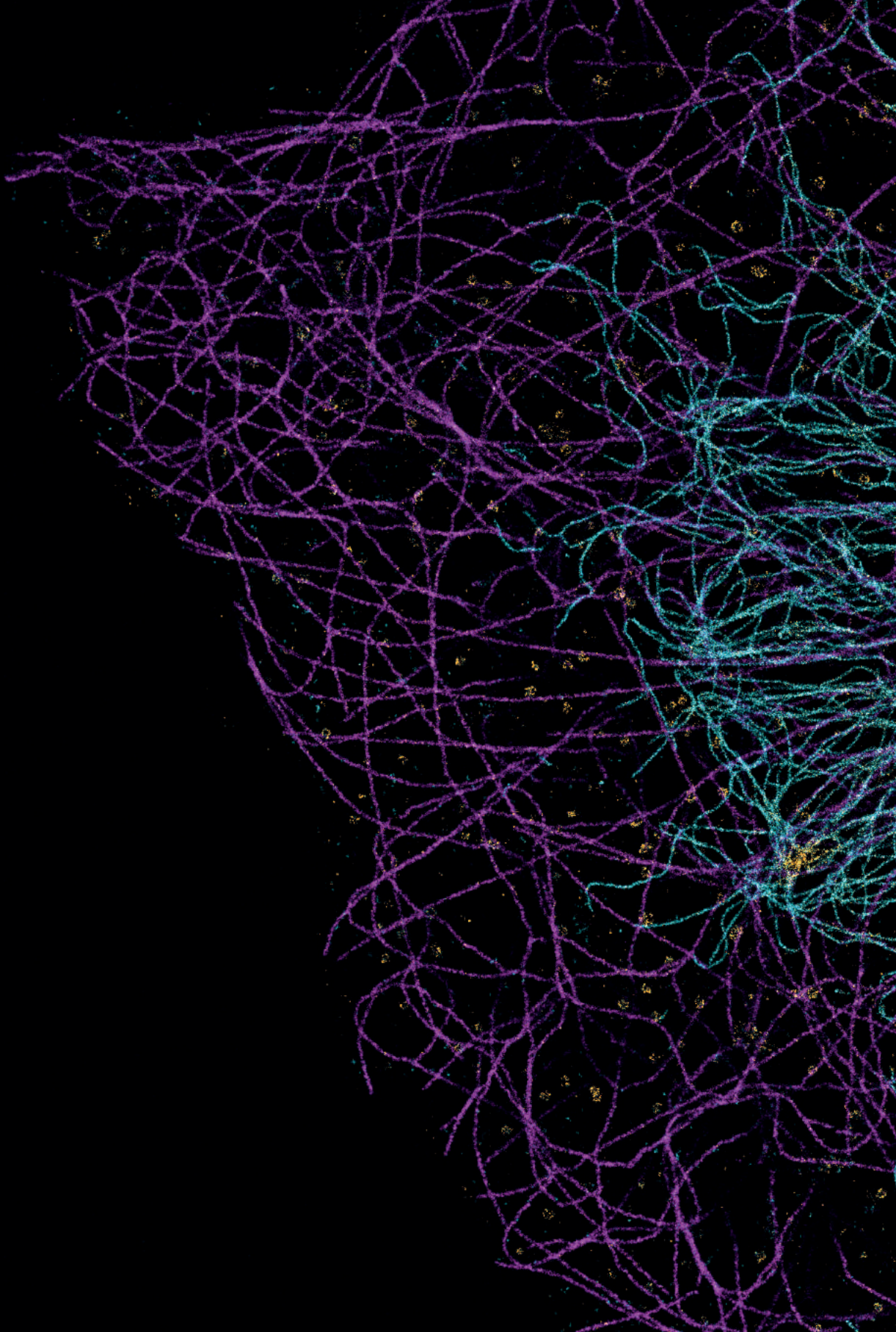

4

3D multi-colour far-red single-molecule localization microscopy with probability-based fluorophore classification

Single-Molecule Localization Microscopy remains limited in its ability for robust and simple multi-colour imaging. Whereas the fluorophore Alexa647 is widely used due to its brightness and excellent blinking dynamics, other excellent blinking fluorophores, such as CF660 and CF680, spectrally overlap. Recently, an alternative way to spectrally unmix far-red fluorophores was demonstrated on a 4Pi microscope, in an approach termed 'salvaged fluorescence' detection. Here we present an improved experimental implementation of the salvaged fluorescence concept which is implementable on conversional microscopes. The emission is split in a short and long wavelength channel to enable classification and localization, but now imaged on a single camera at the emission port. We furthermore explore if the SF classification approach can be improved by using a Generalized Maximum Likelihood Ratio Test that incorporates the photon statistics of both channels and compare the performance of this test to traditional ratio-metric unmixing and Salvaged Fluorescence. We demonstrate the applicability of this implementation on a variety of samples and targets.

This chapter is currently under review.

4.1 Introduction

15 years after its invention, Single-Molecule Localization Microscopy (SMLM) has developed into a reliable and widely used imaging modality to resolve structures beyond the diffraction limit [1–3]. The fluorophore Alexa647 (AF647) is the staple of the most popular SMLM technique called direct Stochastic Optical Reconstruction Microscopy (dSTORM) [4] due to its brightness and excellent blinking dynamics. However, finding spectrally complementary dyes for multi-colour imaging has remained a challenge. It takes extensive tuning of laser power and buffers to optimize the blinking when using fluorophores outside of the far-red channel [5]. In contrast, other far-red fluorophores such as CF660 and CF680 also exhibit proper brightness and blinking, but display significant spectral overlap.

One way to overcome this challenge is the use of a grating or prism (spectroscopic SMLM) [6–8] or to encode the spectral information in the PSF [9]. However, these methods increase the footprint of the spot deteriorating the signal to background ratio and significantly increase the sparsity constraints, which makes them unsuitable for many applications. Another option is to use ratio-metric spectral unmixing [10–12]. However, regular ratio-metric spectral unmixing still requires significant separated emission spectra (i.e. AF647 and CF660 cannot be used without major crosstalk or significant rejection). Another complication of ratiometric spectral unmixing is that it requires nanometer registration of the imaging channels. In order to perform this correctly, chromatic aberrations and field distortions have to be calibrated with a high precision, about 20 to 50 times smaller than the pixel size, to ensure super-resolution reconstructions without significant misalignment [10]. Therefore artefacts can be easily introduced when calibration is not performed correctly and frequently.

Recently, an alternative way to spectrally unmix AF647 and CF660 was demonstrated on a 4Pi microscope, in an approach termed 'Salvaged Fluorescence' (SF) detection [13]. Here localization and detection is performed using the fluorescence collected in the regular imaging channel, but the fluorescence reflected by the dichroic mirror that couples in the excitation light (called 'salvaged fluorescence') is used for classification. This captures the low wavelength front of the emission spectrum, which is the most distinguishable feature of the different far-red fluorophores. As such, this small wavelength window enables adequate classification without compromising the detection and localization in the other channel. Furthermore, this method does not require nanometer channel registration. However, conventional microscopes require an extensive rebuild and an additional camera in order to detect the light reflected by the excitation dichroic mirror. This has so far limited the implementation of SF to other systems. There is therefore a need for a implementable solution for conventional microscopes.

Another possible point of improvement of SF is the classification pipeline. In SF the intensity in the short wavelength channel is estimated by integrating the (background corrected) region of interest (ROI) of the spot. Additionally, a 2D Gaussian mask is applied to ROI to reduce the effect of (high) pixel values at the periphery of the ROI. This SF metric is then divided by the estimated photon count in the (high intensity) long wavelength channel to get the SF ratio. This pragmatic approach has

proven to be a successful classification pipeline, but does not incorporate photon statistics. This aspect is generally considered as one of the main principles in SMLM where the Cramér Rao Lower Bound dictates localization precision. We therefore hypothesized that a classification approach which incorporates photon statistics is able to outperform the SF classification approach.

Here we present an improved experimental implementation of the SF concept which is implementable on conversional microscopes. Inspired by the salvaged fluorescence concept, the emission is split in a high intensity, long wavelength channel, used for detection and localization, and a low intensity, short wavelength channel used to facilitate classification. However, by optimizing the choice of dichroic mirrors and filters both channels are now imaged on a single camera which is mounted on the emission port. We furthermore explore if the classification approach of SF can be improved by using a statistical test called a Generalized Likelihood Ratio Test (GLRT) [14]. Such a test has been demonstrated to distinguish optimally between random background fluctuations and (dim) single-molecule blinking events [15]. In our case, the GLRT can determine the most likely fluorophore candidate for the blinking event, given the measured pixel values in both channels. We demonstrate this experimental implementation and classification approach for 2-colour dSTORM (with AF647 and CF660 or CF680) and 3-colour dSTORM (with AF647, CF660 and CF680) in both 2D and 3D using astigmatic PSF engineering [16]. Lastly, we compare the classification performance of the GLRT to traditional ratio-metric demixing and Salvaged Fluorescence and discuss options to improve the performance of the GLRT.

4.2 Results

4.2.1 Setup

We used a regular TIRF microscope equipped with a dual channel module and chose our filters in such a way that all the fluorescence is collected and split onto a single camera (see Material and Methods). The emission was split in a short channel (channel 1) with intensity fraction $\eta_1 = N_{\text{ph}}^{\text{ch1}}/N_{\text{ph}}^{\text{total}}$ and a long channel (channel 2) with fraction $\eta_2 = (1-\eta_1)$. See Supplementary Figure 4.A.1 for the spectral characteristics of all the components. These spectral dichroic mirrors and filters were chosen such that the first part of the emission peak of AF647 was just captured in channel 1, resulting in intensity fractions of $\eta_1^{\text{AF647}} = 13.3\%$, $\eta_1^{\text{CF660}} = 3.3\%$ and $\eta_1^{\text{AF647}} = 1.5\%$ for AF647, CF660 and CF680, respectively. Detection and localization was performed in the long channel which collects 86.7%, 96.7% and 98.5% of their fluorescence, respectively. For a 500 photon event, the small loss in intensity induced by this separation corresponds to a drop in localization precision of roughly 1 nm, 0.2 nm and 0.1 nm in the case for AF647, CF660 and CF680 respectively.

4.2.2 Likelihood Ratio Test for fluorophore classification

The Generalized Likelihood Ratio Test can classify the fluorophores based on the prior knowledge that a specific blinking event is either caused by fluorophore A or fluorophore B, which will yield two different intensity ratios between channel 1

and 2. The GLRT therefore has to test the following hypotheses

$$\begin{array}{ll} H_0: & \eta_1 = \eta_1^A \\ H_1: & \eta_1 = \eta_1^B \end{array} \tag{4.1}$$

with $\eta_1^{\mathrm{A/B}}$ the (calibrated) intensity fraction in channel 1 for fluorophore A or B. This leads to the test statistic T, given by

$$T = 2\left(\log\limits_{\max\theta_A} L\left\{\theta_A, \eta_1^A | d_k\right\} - \log\limits_{\max\theta_B} L\left\{\theta_B, \eta_1^B | d_k\right\}\right) \tag{4.2}$$

where $\log\limits_{\max\theta_A} L\left\{\theta_A, \eta_1^A | d_k\right\}$ denotes the maximum log likelihood obtained by a 2- channel MLE fit of pixel data d_k with fit parameters θ and fixed intensity fraction η_1. This MLE fit procedure fits two coupled Gaussian distributions to the two spots, where the η_1 governs intensity ratio between the two Gaussian distributions (see Supplementary Note for details). To obtain the test statistic value, the two spots of a single blinking event are fitted twice: once with a fixed intensity fraction η_1^A (assuming it is fluorophore A) and once with a fixed intensity fraction η_1^B (assuming it is fluorophore B, see Figure 1d). The GLRT, which determines which fluorophore is the most likely candidate for a blinking event, provides the decision rule

$$\begin{array}{rcl} T > c_0 & \rightarrow & \text{fluorophore A} \\ T > c_1 \,\&\, T < c_0 & \rightarrow & \text{rejection} \\ T < c_1 & \rightarrow & \text{fluorophore B} \end{array} \tag{4.3}$$

with $c_{0/1}$ adjustable thresholds. These thresholds can be chosen to reduce the false positive rates, $P(T > c_0|H_1)$ and $P(T < c_1|H_0)$, and achieve a significance level α via $P(T > c_0|H_0) = \alpha$ and $P(T < c_1|H_1) = \alpha$. As stated by the Neyman–Pearson lemma [14], this likelihood-ratio test is the most powerful among all level-$alpha$ tests and can therefore classify the fluorophores with the lowest possible false positive rate for a chosen threshold c_i. A possible implementation in the case for 3 or more fluorophores is to test which of the models is the most likely [17]. However, here we perform the GLRT recursively (fluorophore A vs B followed by fluorophore B vs C) which is possible because $\eta_1^A > \eta_1^B > \eta_1^C > \cdots > \eta_1^N$. This allows for multiple thresholds to tune the false positive rates of each fluorophore. We termed this classification method Probability-based Fluorophore Classification (PFC).

4.2.3 Classification performance

We first analyzed the performance of the PFC for dual colour cases (AF647 vs CF660 and AF647 vs CF680). We experimentally obtained the distributions of $P(T \mid H_i)$ by measuring the values of the test statistic of blinking events in samples labeled with a single fluorophore (see Figure 4.2.1f). We preferred this experimental approach because it captures the natural variance in the intensity fraction (no event will have the exact calibrated intensity fraction) and it also includes possible SMLM imperfections, such as overlapping events or other blinking artefacts. This approach therefore gives a realistic false positive rate. We chose cutoff values of c_0 = 9 and c_1 = -3

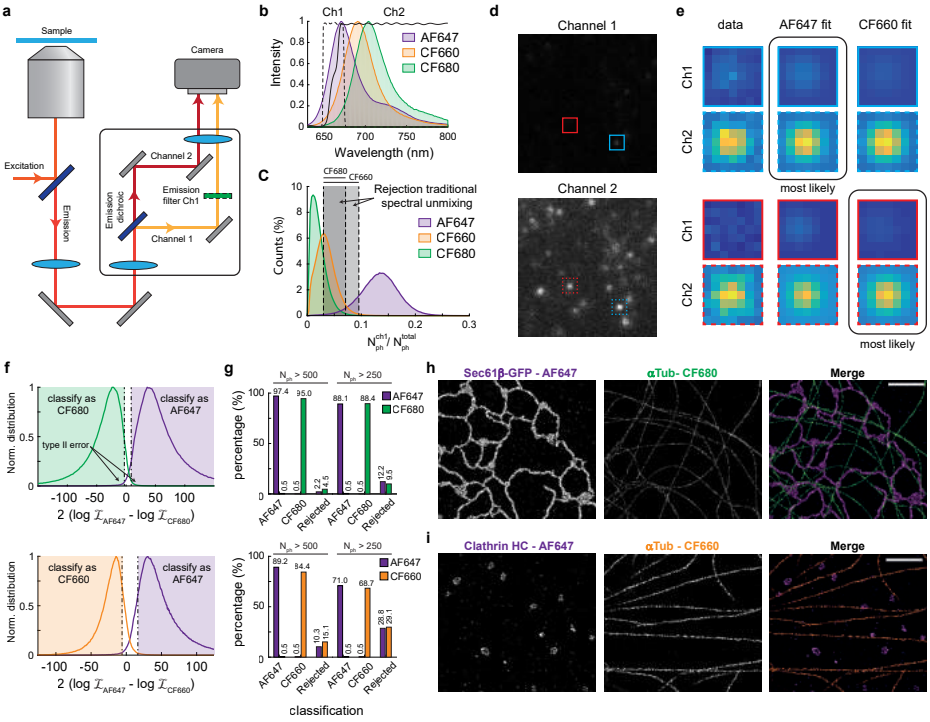

Figure 4.2.1: a) Simplified diagram of the setup. b) Emission spectra of AF647, CF660 and CF680, overlayed with the emission dichroic (solid line) and channel 1 emission filter (dashed line). c) Distribution of the measured intensity fraction of channel 1 for events with 500 photons or more (n = 9.5×10^5 events for AF647, n = 7.8×10^5 events for CF660 and n = 9.6×10^5 for CF680, N=5 acquisitions for each fluorophore). Grey regions indicate rejection areas when using traditional spectral unmixing to achieve a false positive rate of 0.5%. d) Example acquisition of channel 1 and channel 2 with a sample labeled with AF647 and CF660. e) Example of the GLRT classification and the 2 MLE fits. f) Distribution of the GLRT with AF647 versus CF680 (top) and AF647 versus CF660 (bottom) for all events of c. Dashed lines indicate the cutoff values. Events with a GLRT value between the cutoffs are rejected. g) Classification percentages for all events with photon counts 500 or more for AF647 versus CF680 (top) and AF647 versus CF660 (bottom). h) Example 2-colour PFC-dSTORM reconstruction of a COS-7 cell stained for ER (Sec61b-GFP overexpression, magenta) and alpha-tubulin (green) using AF647 and CF680, respectively. Scale bar indicates 2 μm. i) Example 2-colour PFC-dSTORM reconstruction of a COS-7 cell stained for clathrin HC (magenta) and alpha-tubulin (orange) with AF647 and CF660. Scale bar indicates 2 μm.

to achieve false positive rates of 0.5% for both AF647 and CF680. This resulted in successfully classified fractions of 97.4% and 95% of the events as AF647 and CF680, respectively, with unclassified fractions of 2.2% and 4.5% when considering events with 500 photons or more (see Figure 4.2.1g and Supplementary Figure 4.A.2. The distributions of $P(T \mid H_i)$ can be approximated by two Gaussians when binned for photon count and the distance between these two Gaussians increased for higher photon counts (see Supplementary Figure 4.A.2). For this reason, less stringent cutoffs could be used for events with higher photon counts, which would result in a lower rejection rate of these high-intensity events, but a larger total amount of rejected events. A similar classification performance was achieved for AF647 in combination with CF660. In this combination, 10.3% and 15.1% has to be rejected respectively in order to achieve false positivity rates of 0.5%.

With our method we were able to perform 2-colour dSTORM with both fluorophore combinations (see Figure 4.2.1h&i). We observed a clean separation between ER, labelled with AF647, and microtubules labeled with CF680 (see Figure 1h). We furthermore observed clearly visible clathrin coated vesicles and pits alongside densely labeled microtubules with no noticeable crosstalk using AF647 and CF660 (see Figure 4.2.1i). We show a collection of our multi-colour imaging modality for a variety of targets in Supplementary Figure 4.A.4&4.A.5 (i.e. different microtubule subsets, microtubules and mitochondria, pre- and postsynaptic markers).

4.2.4 Three colour imaging

We next tested if we could extend our approach to 3-colour imaging. To achieve sufficient separation in the test statistics we introduced a different emission dichroic mirror (see Figure 4.2.2a and Supplementary Figure 4.A.1). The intensity fractions in channel 1 are in this case 27%, 8% and 3% for AF647, CF660 and CF680, respectively (see Figure 4.2.2b). For 3-colour imaging with GLRT each blinking event is tested for AF647 vs CF660 and CF660 vs CF680. The distribution of the test statistics $T_{\text{AF647vsCF660}}$ and $T_{\text{AF647vsCF680}}$ can then be plotted in a 2D histogram, where each quadrant is associated with a unique fluorophore or rejection (see Figure 4.2.2c). Again, appropriate cutoff values for classification can be introduced to achieve the desired false positive rates (Figure 4.2.2d&e). In this case, false positive rates of 1% can be achieved while rejecting 0.1% of AF647, 28.5% of CF660 and 38.6% of CF680 for events which emitted 500 photons or more.

To demonstrate the 3-colour capabilities of PFC in dense and overlapping structures we stained COS-7 cells for tyrosinated tubulin, vimentin and clathrin heavy chain (Figure 4.2.2f-i). We observed a clear separation between the microtubule network, the intermediate filaments and the clathrin coated pits. However, there appeared to be some crosstalk from the CF660 channel to the CF680 channel at sites where vimentin is abundant. This is expected when there are large discrepancies in the abundance of the stained structure, even with low false positive rates. Reconstructions of the full field-of-view are shown in Supplementary Figure 4.A.6.

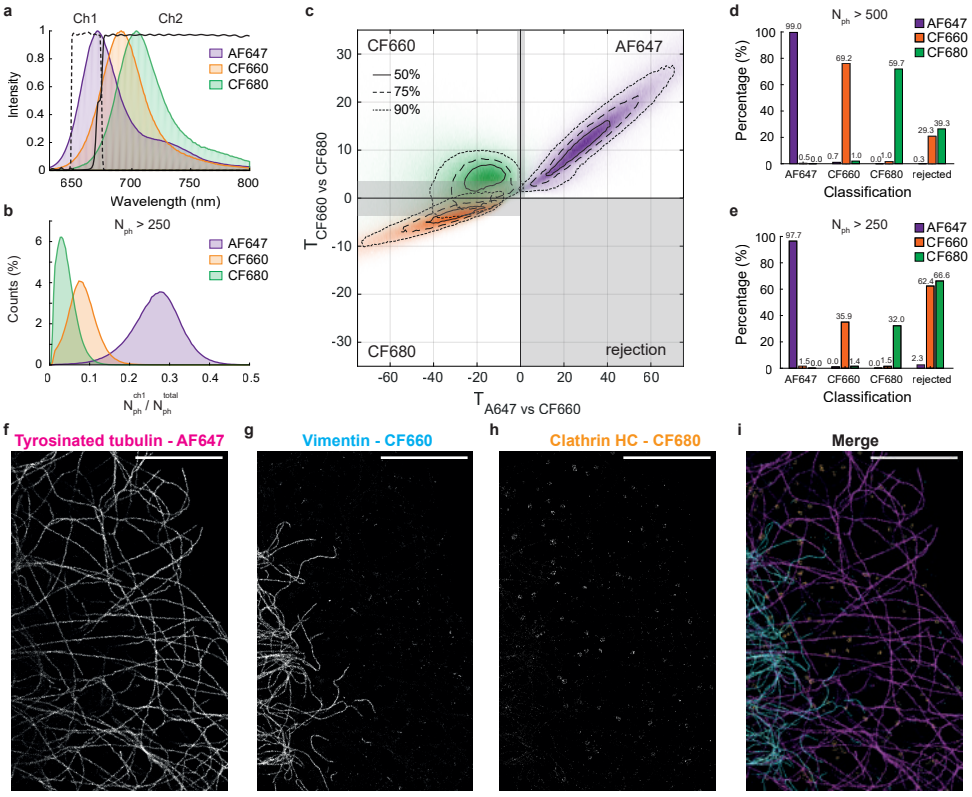

Figure 4.2.2: a) Emission spectra of AF647, CF660 and CF680, overlaid with the emission dichroic (solid line) and channel 1 emission filter (dashed line). b) Distribution of the measured intensity fraction of channel 1 for events with 250 photons or more (n=7.3×10^5 events for AF647, n = 1.1×10^6 events for CF660 and n = 5.1×10^5 for CF680, N=5 acquisitions for each fluorophore). c) 2D histogram of the test statistics AF647 versus CF660 and CF660 versus CF680 for the events shown in b. Grey area indicates rejection zone. (Dotted) lines indicate regions containing 50%, 75% and 90%, as indicated. d&e) Classification rates for photon thresholds of 500 and 250. f) Example 3 colour PFC-dSTORM reconstruction of a COS-7 cell stained for tyrosinated tubulin (magenta), vimentin (cyan) and clathrin heavy chain (orange) with AF647, CF660 and CF680 respectively. Scale bar indicates 5 μm.

4.2.5 Astigmatic 3D imaging

We extended our multi-colour SMLM approach to 3D localization by using astigmatic PSF engineering using a cylindrical lens module. For this, we modified the 2-channel MLE fit required for the GLRT to fit asymmetric Gaussians, which introduced an additional fit parameter (see Supplementary Notes for details). We performed 2-colour 3D SMLM with astigmatic PSF engineering on COS-7 cells stained for ER and microtubules (see Figure 4.2.3). Our method was able resolve a microtubule width of 40 nm, consistent with immunolabeling [18] (see Figure 4.2.3d&g). Furthermore we were able to resolve the nanoscale ER morphology and observed ER matrices, consistent with recent findings using super-resolution microscopy [19] (see Figure 4.2.3e). Additionally, we found ER tubulation in the cellular periphery directly adjacent to microtubules, likely as result of microtubule dependent ER remodeling [20] (see Figure 4.2.3f). Lastly, our imaging modality was able to resolve hollow ER tubules in 3D at certain locations (see Figure 4.2.3i). Altogether, this shows that PFC allows the study of ER - cytoskeleton interaction with nanometer resolution in 3D.

4.2.6 Classification Comparison

We next compared the performance of PFC to the classification scheme used in Salvaged Fluorescence(SF) and ratio-metric unmixing (RU). For our comparison, we again used the single-fluorophore samples to determine the rejection rates for different fluorophore combinations for the desired false-positive rate of 0.5%. The boundaries of the rejection zone for each method were obtained by analyzing the 1D histograms of the estimated intensity ratios (RU), salvaged fluorescence ratios (SF) and log likelihood ratios (PFC), see Figure 4.2.4.

When classifying AF647 vs CF680 PFC clearly outperformed traditional ratiometric spectral unmixing (Figure 4.2.4a-d), but failed to outperform Salvaged Fluorescence. PFC achieves a false-positive rate of 0.5% while rejecting 12.2% and 9.5% of AF647 and CF680 respectively. For this false-positive rate traditional ratio-metric unmixing rejected 20.0% and 45.0%, while SF only rejected 4.7% and 6.1%. Classification performance was substantially reduced when classifying AF647 vs CF660, but the relative performance remained similar. In this case PFC rejected 28.8% and 29.1% for AF647 and CF660 respectively for a false-positive rate of 0.5%, while RU rejected 41.5% and 78.9% and SF rejects 18.7 and 30.7%. Here PFC showed a small improvement over SF when classifying CF660 (29.1% over 30.7%), but the combined rejection rates of AF647 and CF660 were still in favor of SF. In the 3 colour case (AF647 vs CF660 vs CF680) we chose the rejection zones based on a 1.5% false-positive rates, see Figure 4.2.4i-k. Here ratio-metric unmixing was inadequate in classifying CF660 and CF680 and rejects 92.3% and 87.7% of CF660 and CF680 respectively. PFC and SF both classified AF647 with high true-positive rate (97.7% and 96.6% resp.) and achieved similar rejection rate of CF660 (61.1% and 59.9% resp.) and CF680 (66.6% and 54.6% resp.). These results demonstrate that although this implementation of the GLRT clearly improves classification over traditional spectral unmixing, SF remains the best performing classification algorithm.

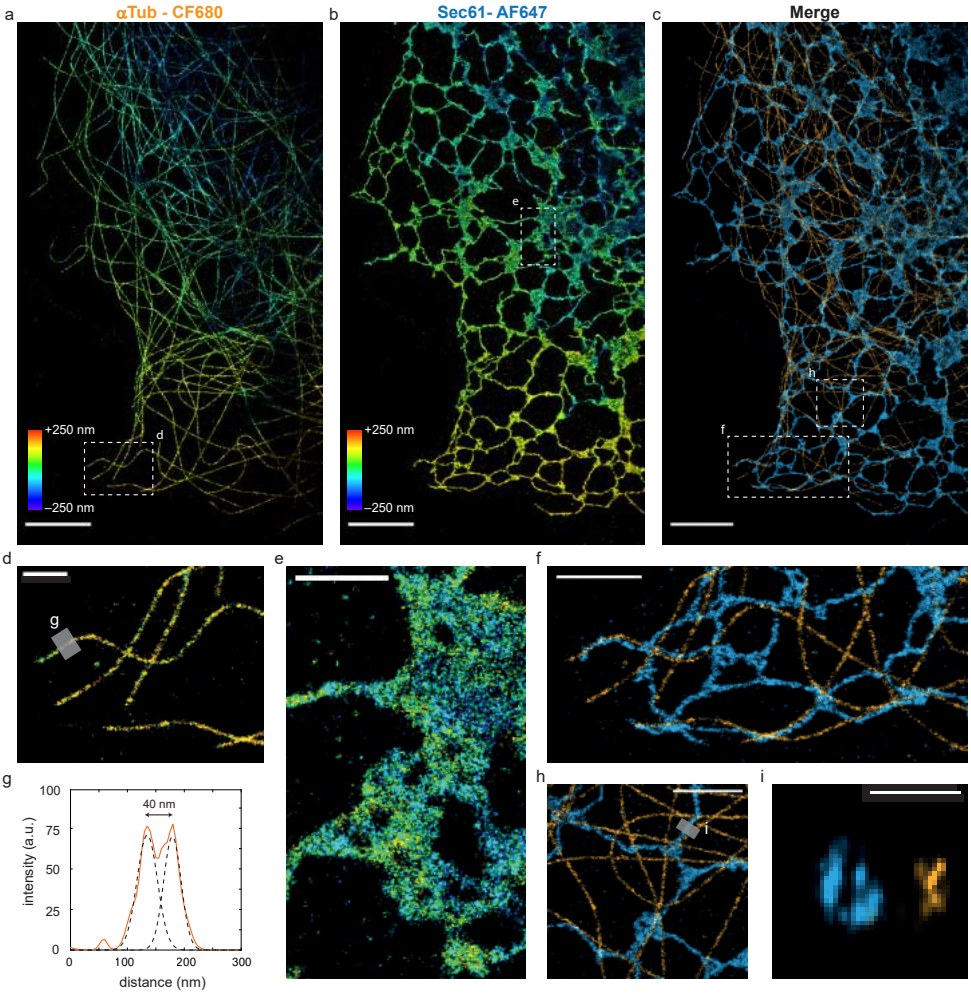

Figure 4.2.3: a-c) Example 2-colour 3D PFC-dSTORM reconstruction of a COS-7 cell stained for ER (Sec61-GFP overexpression, cyan) and alpha-tubulin (orange) with AF647 and CF680, colour-coded for depth. d-f) Zooms of a, b and c. g) Intensity distribution of region indicated at d. h) Zoom of c. i) Cross section of region indicated at h. Scalebars indicates 5 μm (a, b, c), 2 μm (d, e, f, h) and 200 nm (i).

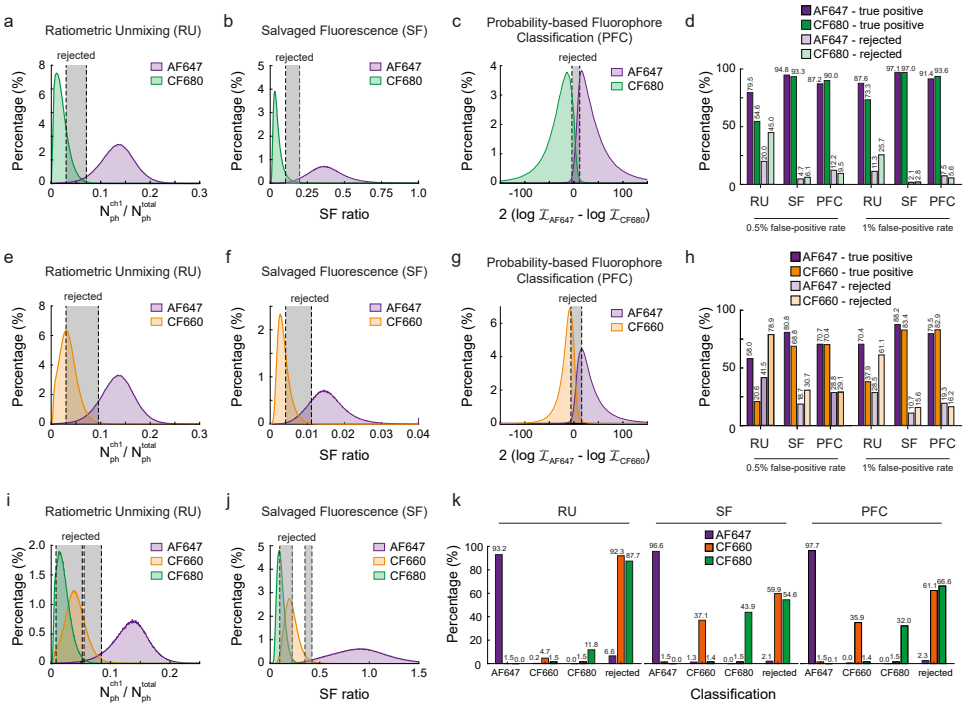

Figure 4.2.4: a-c) 1D histogram of the estimated intensity (a) for ratio-metric unmixing (RU), the salvaged fluorescence ratio (SF, b) and the test statistic of PFC (c) for AF647 vs CF680. Events are filtered by a photon threshold 250. Rejection zones are shown for a 0.5% false-positive rate. d) Classification rates of RU, SF and PFC. e-h) Similar to (a-c) but for AF647 vs CF660. i-j) Similar to (a&b) but for 3 colour case (AF647 vs CF660 vs CF680). k) Classification rates in the 3 colour case for RU, SF and PFC with a false-positive rate of 1.5%.

4.3 Discussion

In this work we introduced an improved experimental implementation of the SF concept which is implementable on conventional microscopes. The emission is split in a high intensity channel and a low intensity channel, inspired by the salvaged fluorescence approach. However, our implementation only requires a single camera, does not require major rework on the microscope and is universally implementable. This approach allowed us perform the nanometric localization on just a single channel, which minimizes chromatic aberrations. The small associated loss in localization precision due to the photon loss in channel 1 mostly affects AF647, which is mitigated by the fact that AF647 is one of the brightest fluorophores available.

We furthermore introduced a Generalized Likelihood Ratio Test for fluorophore classification termed PFC and compared this to traditional ratio-metric unmixing and the Salvaged Fluorescence approach. It appears that this implementation of the GLRT outperforms traditional ratio-metric unmixing but not the Salvaged Fluorescence approach. This is unexpected as the Neyman-Pearman lemma states that this likelihood-ratio test is the most powerful among all level-α tests. A possible explanation why SF outperforms PFC is that the fit algorithm does not converge properly. In many instances the intensity in the short wavelength channel is sufficiently low that the number of signal photons is lower than the background photon level. Therefore the background shot noise outweighs the signal photon level per pixel, which might prevent proper convergence. We explored improving the convergence by constraining the fit algorithm in two ways: 1) a fixed Gaussian width and 2) no cross channel alignment. However, none of these constrains improved the classification performance of PFC (data not shown) and additional investigation is required to understand the performance of PFC. It might be possible to derive a fundamental bound on the rejection rate, similar to the work by Smith et al [15]. Such a bound can be used as reference in a simulation study to assess the performance of PFC and investigate potential inaccuracies.

Another aspect to consider when comparing these different classification methods is which facets of the available information they use. SF uses the temporal median pixel value to estimate the background in channel 1 and thereby performs an improved background estimation compared to an estimation based solely on the data of the spot itself. This implementation of the GLRT statistic does not use this additional information and estimates the (uniform) background which is included as fit parameter. It is therefore likely that SF is able to outperform the GLRT because it estimates the background more effectively. An alternative GLRT implementation, which uses additional acquisitions for background estimation, might therefore be able to improve PFC classification.

Nonetheless, this experimental implementation, where all fluorescence is captured on a single camera and split in a low intensity and high intensity channel, is very photon-efficient compared to spectroscopic methods that often require 50% or more of the fluorescence for wavelength estimation [6–8]. This implementation also has several advantages over other multi-colour SMLM approaches such as multiplexed DNA-PAINT [21], where a single acquisition can take multiple hours and

which requires components with a very short shelf lifetime. Lastly, our implementation has no (additional) sparsity constraints compared to other methods using PSF engineering [9] or other '2-spot' modalities [22, 23]. Therefore, dense structures such as microtubules and ER can still be imaged simultaneously. We demonstrated multi-colour dSTORM with this implementation on a variety of samples and structures, such as the cytoskeleton network, ER and neuronal synapses, both in 2D and 3D, and show that this method is compatible with many different cellular components and is able to separate these with minimal crosstalk. We therefore anticipate this experimental implementation in combination with the SF classification approach to become the go-to method for multi-colour SMLM.

4.A Appendix

4.A.1 Methods

Setup

The setup consisted of a Nikon TI-E microscope equipped with a TIRF APO objective lens (NA = 1.49, 100X). A 638 nm laser (MM, 500mW, Omicron) was used for TIRF excitation via a laser clean-up filter (LL01-638, Semrock) and excitation dichroic (FF649-Di01, Semrock). The collected emission was filtered by a emission filter (BLP01-633R-25, Semrock) and relayed via a 1.5X tube lens (2D imaging) or 1X tube lens (3D imaging) to the emission port equipped with a cylindrical lens module (Nikon) and an Optosplit III module (Cairn Research). The emission dichroic (FF660-Di02, Semrock for 2 colour imaging and Di03-R660-t1, Semrock for 3 colour imaging) splitted the emission in a short channel and a long channel on a EMCCD (iXon 897 – Andor). See the Supplementary Note for details on the calibration. An additional emission filter (FF01-661/20-25, Semrock) was placed in channel 1. See Supplementary Figure 4.A.1 for the corresponding spectral characteristics of all the components.

PSF-model and 2-channel MLE fit

We modeled the PSF in each channel as a 2D Gaussian, a simplification of the model used in [24], where the intensity $\mu_{k,\lambda}$ at pixel location k for the respective channel λ is given by and with N_{ph} the total number of emitted photons, a the pixelsize, x_0 and y_0 the position of the molecule, x/y_{align} a possible subpixel alignment correction between the channels, σ the width of both Gaussian PSFs and $b_{1/2}$ the background in each channel. The log likelihood of the fit [9] is given by with $d_{k,\lambda}$ the observed value of pixel k in channel λ and σ_{noise} the read noise of the camera pixel, which we assume to be zero for the EMCCD. The two spots in channel 1 and 2 are fitted simultaneously, leading to 8 fit parameters ($\theta = x_0, y_0, x_{\text{align}}, y_{\text{align}}, \sigma, N_{\text{ph}}, b_1, b_2$) in total. In the case for astigmatic PSF a x- and y-directional width is fitted. See Supplementary Note on details of the fit algorithm.

Intensity calibration

The intensity fractions for each fluorophore is calibrated by imaging COS-7 cells stained for α-tubulin with a single fluorophore. The intensity in channel 2 is estimated with a regular 2D Gauss MLE fit which fits the x/y-position, width, intensity

and background. The intensity in channel 1 is difficult to estimate as these photon counts are extremely low compared to the background level. To overcome this calibration issue we fit each spot in channel 1 with a 2D Gauss with a fixed width, obtained from the estimated width of the high intensity spot in channel 2. Lastly, fits are classified as outlier and removed if the log likelihood is smaller than the average log likelihood minus 3 standard deviations or if the estimated photon count is below 3 (channel 1) or 100 (channel 2). The intensity fraction is then estimated from the estimated photon counts in each channel of all spots with a weighted least-squares linear fit, where the weight is taken as the square root of the total estimated photon count of each spot.

Sample preparation
Animals
In this study female pregnant Wistar rats were obtained from Janvier, and embryos (both genders) at E18 stage of development were used for primary cultures of hippocampal neurons. All experiments were approved by the DEC Dutch Animal Experiments Committee (Dier Experimenten Commissie), performed in line with institutional guidelines of University Utrecht, and conducted in agreement with Dutch law (Wet op de Dierproeven, 1996) and European regulations (Directive 2010/63/EU).

Cell culture
COS-7 and U2OS cells were grown in DMEM (Lonza, 12-604F) supplemented with 10% fetal calf serum (FCS, Sigma, F7524) at 37°C with 5% CO2. Dissociated hippocampal neuron cultures were prepared from rat pups at embryonic day 18 as described previously [25]. Briefly, cells were plated on 18-mm glass coverslips coated with laminin (1.25 mg/ml) and poly-L-lysine (37.5 mg/ml)(P8920 Sigma Aldrich) at a 50K/well density. Cells were maintained in Neurobasal medium (NB, Gibco, 21103-049) supplemented with 2% B27 (Gibco, 17504001), 0.5 mM glutamine (Gibco, 25030-032), 15.6 μM glutamic acid, and 1% penicillin/streptomycin (Sigma, P0781) at 37°°C in 5% CO2.

Plasmids and transfection
For visualizing the ER we overexpressed GFP-Sec61β (Addgene #15108), an ER membrane protein. For transfection, DNA (1 µg) was mixed with 3 µl Fugene6 (Roche, #11836145001) in 200 μl opti-MEM (Gibco, 31985-047) and added to the cells for 16 hours or until fixation at 37°C with 5% CO2.

Fixation
Depending on the different structures that were targeted, three different fixation protocols were used: pre-extraction protocol, glutaraldehyde fixation protocol and PFA fixation protocol. For samples to be labeled for Tubulin, Clathrin HC and Vimentin we used the pre-extraction protocol, for samples with Sec61b-GFP overexpression we used the glutaraldehyde fixation protocol and for the samples to be labeled for Cytochrome C we used the PFA fixation protocol. All are described below.

The pre-extraction protocol was used for most cytoskeletal structures to remove the cytosolic pool of monomers. Cells were pre-extracted for 1 minute in extraction buffer (0.3% Triton X-100 (Sigma X100), 0.1% glutaraldehyde (GA) (Sigma G7526) in MRB80 buffer (80 mM Pipes (Sigma P1851), 1 mM EGTA (Sigma E4378), 4 mM MgCl2, pH 6.8), pre-warmed at 37°C. Afterwards, cells were fixed for 10 minutes in 4% EM-grade parafor-maldehyde (PFA) (Electron Microscopy Science, 15710) and 4% sucrose in MRB80 buffer (pre-warmed at 37°C).

When targeting membrane bound structures the pre-extraction protocol cannot be used as this dissolves the membranes before fixation. We therefore used an alternative protocol that uses GA and PFA in cytoskeleton preserving buffer. Cells are fixed using 0.1% GA, 4% PFA and 4% sucrose in MRB80 buffer for 10 minutes (pre-warmed at 37°C). Unfortunately, not all antibodies are compatible with glutaraldehyde, which results in a loss of signal intensity. For Cytochrome C we therefore fixed cells using 4% PFA and 4% sucrose in MRB80 buffer for 10 minutes (pre-warmed at 37°C).

Immunostaining

After fixation cells were washed 3 times in PBS (1 quick wash, followed by 2 washes of 5 minute) and permeabilized for 10 minutes with 0.25% Triton-X in MRB80. After again washing 3 times with PBS samples were further incubated for 1 hour in blocking buffer (3% w/v BSA in MRB80 buffer) at room temperature. Next, samples were incubated overnight at 4°C in primary antibodies diluted in blocking buffer. To proceed cells were washed 3 times in PBS before incubating for 1 hour at room temperature with secondary antibodies diluted in blocking buffer. After incubation cells were once more washed 3 times in PBS and kept in PBS at 4°C or mounted for imaging.

Table 4.1: Primary antibodies.

Target protein	Species	Dilution	Suplier	Cat #	Clone	Lot #
clathrin heavy chain	mouse	1/500	Thermo fisher	MA1-065	X22	VL315162
α-tubulin	mouse	1/1000	Sigma	T5168	B-5-1-2	047M4760V
α-tubulin	rabbit	1/1000	Abcam	52866	EP1332Y	GR3241328-2
GFP	chicken	1/1000	Aves Lab	GFP1010	polyclonal	GFP3717982
vimentin	rabbit	1/300	Abcam	ab92547	EPR3776	GR3258719-5
tyrosinated tubulin	rat	1/250	Abcam	ab6160	YL1/2	GR3377281-5
acetylated tubulin	mouse	1/600	Sigma	T7451	6-11B-1	059M4812V
homer	rabbit	1/600	SySy	160 002	polyclonal	Gift from Hoogenraad lab
bassoon	mouse	1/600	Enzo	ADI-VAM-PS003-F	SAP7F407	06231712

Table 4.2: Secondary antibodies.

Host species	Target species	Fluorophore	Dilution	Supplier	Cat #	Lot #
goat	chicken	AF647	1/500	Life Technologies	A-21449	1883471
goat	mouse	CF680	1/500	Biotium	20065	14C0103
goat	rabbit	CF660	1/500	Bio-connect	20369	14C0106
goat	mouse	AF647	1/500	Thermo Fisher Scientific	A-21236	2326487
goat	rat	AF647	1/500	Life Technologies	A-21247	1611119
goat	mouse	CF660	1/500	Bio-connect	20368	14C0221

Imaging buffer and sample mounting

In this work we used two imaging buffers: a buffer with an oxygen scavenger (Glox-buffer) and a degassed buffer (N2-buffer). Glox-buffer was prepared as previously described [26]. Briefly, 1M stock solution of MEA (Sigma, 30070-10G, dissolved in 250 mM HCl) and glucose-oxidase plus catalase stock (70 mg/ml glucose-oxidase (Sigma, G2133-10KU, dissolved in Milli-Q), 4 mg/ml catalase (Sigma, C40-100MG) dissolved in Milli-Q) were prepared and stored at -80 ⊠. Just before imaging the final buffer was prepared by diluting MEA, glucose-oxidase plus catalase and glucose being in 50 mM Tris pH 8.0 (Final concentrations: 100mM MEA, 5% w/v glucose, 700 μg/ml glucose oxidase, 40 μg/ml catalase in 50mM Tris pH 8.0). The N2-buffer uses a different method to remove oxygen from the imaging buffer [27]. A solution of 100 mM MEA in 50 mM Tris pH 8.0 was deoxygenated by smooth bubbling with N2 gas for 30 minutes using volumes 200-500 μl of buffer. The buffer was used immediately after this treatment. Samples were mounted in closed off cavity slides (Sigma, BR475505) to prevent oxygen from entering the sample during imaging. The cavity slide was filled with approximately 90 μl of imaging buffer, after which the coverslip was flipped on top. Surplus buffer was removed from the sides of the coverslip using a vacuum pump to create a tight seal. Samples were used for up to an hour of imaging, because blinking behavior was compromised when imaging longer. Coverslip were removed and re-mounted in fresh buffer for a next round of imaging when necessary.

Single-molecule detection and localization

Acquisitions were processed using a temporal median filter to remove constant fluorescence background [28]. Afterwards images were analyzed using the custom ImageJ plugin called DoM (Detection of Molecules,github.com/ekatrukha/DoM_Utrecht), which has been described in detail before [26]. Briefly, each image was convoluted with a combination of a Gaussian and Mexican hat kernel. By thresholding the images spots could be detected, after which their sub-pixel localization could be determined using an unweighted non-linear 2D gaussian fit of the original images using Levenberg-Marquardt optimization. Localizations with a width larger than 130% of the set detection PSF size were regarded as false positives. Reconstructions were generated by plotting each localization as a 2D Gaussian distribution with standard deviations in each dimension equal to the localization error. Drift correction was performed by calculating the spatial cross-correlation function between two intermediate reconstructions.

4.A.2 Supplementary note

PSF-model and 2-channel MLE fit

The PSF in each channel is modelled as a 2D Gaussian where the intensity $\mu_{k,\lambda}$ at pixel location k for the respective channel λ is given by

$$\mu_{k,1} = \frac{\eta_1 N_{\text{ph}} a^2}{2\pi\sigma^2} \exp\left[-\frac{\left(x_k - \left(x_0 - x_{\text{align}}\right)\right)^2 + \left(y_k - \left(y_0 - y_{\text{align}}\right)\right)^2}{2\sigma^2}\right] + b_1 \quad (4.4)$$

and

$$\mu_{k,1} = \frac{\eta_2 N_{\text{ph}} a^2}{2\pi\sigma^2} \exp\left[-\frac{(x_k - x_0)^2 + (y_k - y_0)^2}{2\sigma^2}\right] + b_2 \quad (4.5)$$

with N_{ph} the total number of emitted photons, a the pixelsize, x_0 and y_0 the position of the molecule, x/y_{align} a possible subpixel alignment correction between the channels, σ the width of both Gaussian PSFs and $b_{1/2}$ the background in each channel. The two spots in channel 1 and 2 are fitted simultaneously, leading to 8 fit parameters ($\theta = x_0, y_0, x_{\text{align}}, y_{\text{align}}, \sigma, N_{\text{ph}}, b_1, b_2$). The derivatives needed for the MLE fit routine with respect to the position are given by

$$\frac{\partial \mu_{k,\lambda}}{\partial x_0} = \frac{(x_k - x_0)\,\eta_1 N_{\text{ph}} a^2}{2\pi\sigma^4} \exp\left[-\frac{(x_k - x_0)^2 + (y_k - y_0)^2}{2\sigma^2}\right] \quad (4.6)$$

and

$$\frac{\partial \mu_{k,\lambda}}{\partial y_0} = \frac{(y_k - y_0)\,\eta_1 N_{\text{ph}} a^2}{2\pi\sigma^4} \exp\left[-\frac{(x_k - x_0)^2 + (y_k - y_0)^2}{2\sigma^2}\right] \quad (4.7)$$

where we dropped the channel alignment term. The derivative to x_{align} and y_{align} are similar to these derivatives for the first channel but zero for the second channel. The others derivatives are

$$\frac{\partial \mu_{k,\lambda}}{\partial \sigma} = \eta_1 N_{\text{ph}} a^2 \frac{(x_k - x_0)^2 + (y_k - y_0)^2 - 2\sigma^2}{2\pi\sigma^5} \exp\left[-\frac{(x_k - x_0)^2 + (y_k - y_0)^2}{2\sigma^2}\right] \quad (4.8)$$

$$\frac{\partial \mu_{k,\lambda}}{\partial N_{\text{ph}}} = \frac{\eta_1 a^2}{2\pi\sigma^2} \exp\left[-\frac{(x_k - x_0)^2 + (y_k - y_0)^2}{2\sigma^2}\right] \quad (4.9)$$

and

$$\frac{\partial \mu_{k,\lambda}}{\partial b_1} = \begin{matrix} 1 & \text{for } \lambda = 1 \\ 0 & \text{for } \lambda = 2 \end{matrix} \quad (4.10)$$

$$\frac{\partial \mu_{k,\lambda}}{\partial b_1} = \begin{matrix} 0 & \text{for } \lambda = 1 \\ 1 & \text{for } \lambda = 2 \end{matrix} \quad (4.11)$$

The log likelihood of the fit is given by

$$\log L = \sum_{\lambda=1,2} \sum_{k=x,y} \left(d_{k,\lambda} + \sigma^2_{\text{noise}}\right) \log\left(\mu_{k,\lambda} + \sigma^2_{\text{noise}}\right) - \mu_{k,\lambda} + \sigma^2_{\text{noise}} - \log\Gamma\left(\mu_{k,\lambda} + \sigma^2_{\text{noise}} + 1\right) \quad (4.12)$$

with $d_(k,\lambda)$ the observed pixel value and σ_{noise} the read noise of the camera [9]. In our setup we assume that the read noise of the EMCCD camera is zero. We use a Levenberg-Marquardt optimization routine to effectively maximize the log likelihood, where the next estimated fit parameters for iteration n+1 are given by

$$\theta^{n+1} = \theta^n + (H + \gamma\,\text{diag}(H))^{-1} G \quad (4.13)$$

with γ the dampening factor tuned every iteration. The gradient G of the log likelihood is given by

$$G_i = \sum_{\lambda=1,2} \sum_{k=x,y} \frac{d_{k,\lambda} - \mu_{k,\lambda}}{\mu_{k,\lambda} + \sigma_{\text{noise}}} \frac{\partial \mu_{k,\lambda}}{\partial \theta_i} \quad (4.14)$$

and the Hessian H of the log likelihood is given by

$$H_{i,j} = \sum_{\lambda=1,2} \sum_{k=x,y} \frac{d_{k,\lambda} + \mu_{k,\lambda}}{\mu_{k,\lambda} + \sigma_{\text{noise}}} \frac{\partial \mu_{k,\lambda}}{\partial \theta_i} \frac{\partial \mu_{k,\lambda}}{\partial \theta_j} \quad (4.15)$$

where the second derivatives with respect to the fit parameters are neglected as these are small near the optimum.

In the case for astigmatic 3D encoding we model the PSF as an asymmetric Gaussian given by

$$\mu_{k,1} = \frac{\eta_1 N_{\text{ph}} a^2}{2\pi\sigma_x\sigma_y} \exp\left[-\frac{\left(x_k - \left(x_0 - x_{\text{align}}\right)\right)^2}{2\sigma_x^2} - \frac{\left(y_k - \left(y_0 - y_{\text{align}}\right)\right)^2}{2\sigma_y^2}\right] + b_1 \quad (4.16)$$

and

$$\mu_{k,2} = \frac{\eta_2 N_{\text{ph}} a^2}{2\pi\sigma_x\sigma_y} \exp\left[-\frac{\left(x_k - x_0\right)^2}{2\sigma_x^2} - \frac{\left(y_k - y_0\right)^2}{2\sigma_y^2}\right] + b_2 \quad (4.17)$$

The derivatives with respect to the position are given by (again ignoring the alignment term)

$$\frac{\partial \mu_{k,\lambda}}{\partial x_0} = \frac{\left(x_k - x_0\right)\eta_\lambda N_{\text{ph}} a^2}{2\pi\sigma_x^3\sigma_y} \exp\left[-\frac{\left(x_k - x_0\right)^2}{2\sigma_x^2} - \frac{\left(y_k - y_0\right)^2}{2\sigma_y^2}\right] \quad (4.18)$$

and

$$\frac{\partial \mu_{k,\lambda}}{\partial y_0} = \frac{\left(y_k - y_0\right)\eta_\lambda N_{\text{ph}} a^2}{2\pi\sigma_x\sigma_y^3} \exp\left[-\frac{\left(x_k - x_0\right)^2}{2\sigma_x^2} - \frac{\left(y_k - y_0\right)^2}{2\sigma_y^2}\right] \quad (4.19)$$

The derivatives with respect to the widths of the Gaussian are given by

$$\frac{\partial \mu_{k,\lambda}}{\partial \sigma_x} = \eta_\lambda N_{\text{ph}} a^2 \frac{(x_k - x_0)^2 - 2\sigma_x^2}{2\pi\sigma_x^4\sigma_y} \exp\left[-\frac{(x_k - x_0)^2}{2\sigma_x^2} - \frac{(y_k - y_0)^2}{2\sigma_y^2}\right] \tag{4.20}$$

and

$$\frac{\partial \mu_{k,\lambda}}{\partial \sigma_y} = \eta_\lambda N_{\text{ph}} a^2 \frac{(y_k - y_0)^2 - 2\sigma_y^2}{2\pi\sigma_x\sigma_y^4} \exp\left[-\frac{(x_k - x_0)^2}{2\sigma_x^2} - \frac{(y_k - y_0)^2}{2\sigma_y^2}\right] \tag{4.21}$$

The other derivatives remain similar to the symmetric Gaussian.

Good initial estimates for the fit parameters are essential for finding the global optimum. The background was estimated as the median of the rim pixels of the ROI, the intensity as the total intensity of the background subtracted ROI and the position and width of the spot as the first and second moment of the background subtracted ROI respectively. To ensure physical results, the fit parameters were constrained; x/y-positions to [-200, 200] nm from center, x/y_{align} -positions to [-107, 107] nm, width to [100, 200] nm (2D) and [100, 400] nm (3D), intensity to [1 1e6] and background levels to [0 1e3].

EM-CCD calibration

The EM-CCD was calibrated by imaging an out-of-focus knife-edge to create a smooth gradient over the FOV that covered the complete dynamic range of the camera. The gain and camera offset were then calibrated using the function *cal_readnoise* from the DIPlib library in Matlab (https://diplib.org/). The gain of the camera scaled with the variance of the signal as $\text{var}(S) = g\text{mean}(S) + \sigma_{\text{noise}}^2$ with S the signal in ADU, g the gain and σ_{noise} the read noise. The EM-CCD uses an electron multiplication process which drowns the read noise to zero ($\sigma_{\text{noise}} = 0$). However, this process introduces an additional noise called excess noise, which is indistinguishable from shot noise and effectively doubles it [29]. Therefore the true gain is overestimated by a factor of 2, but this allows the usage of a unmodified likelihood function (Equation 4.12).

4.A.3 Supplementary figures

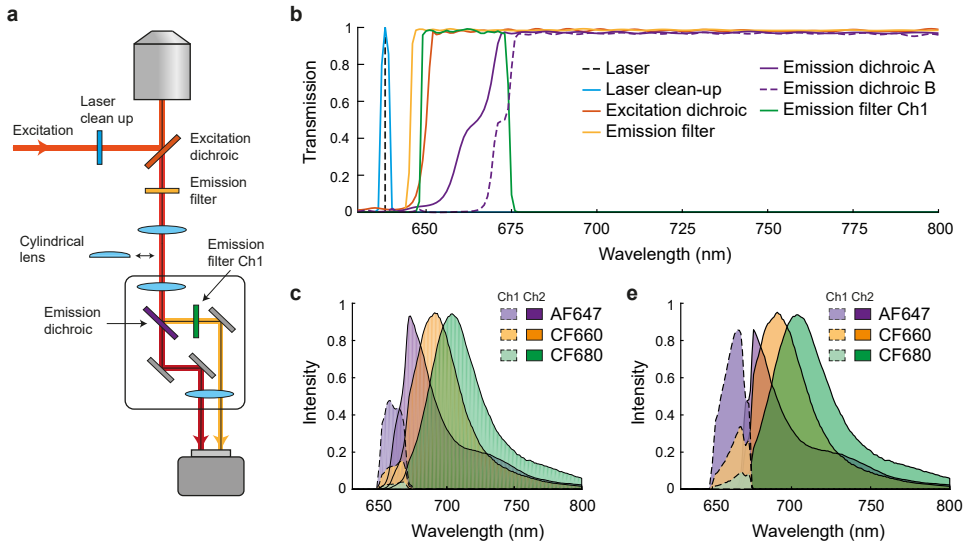

Figure 4.A.1: a) Diagram of the setup. b) Spectral characteristics of all components. Emission dichroic A is used for 2-colour imaging and emission dichroic B is used for 3-colour imaging. c) Theoretical emission intensity in channel 1 and 2 of AF47, CF660 and CF680 with emission dichroic A. d) Theoretical emission intensity in channel 1 and 2 of AF47, CF660 and CF680 with emission dichroic B.

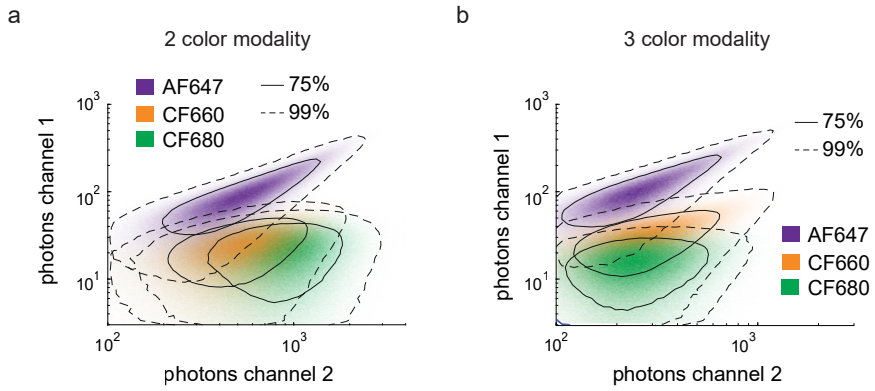

Figure 4.A.2: 2D histogram of the 'salvaged' and 'regular' fluorescence for 2-colour (a) and 3-colour (b) imaging for AF647, CF660 and CF680. Solid and dashed line indicate regions containing 75% and 99% of all events.

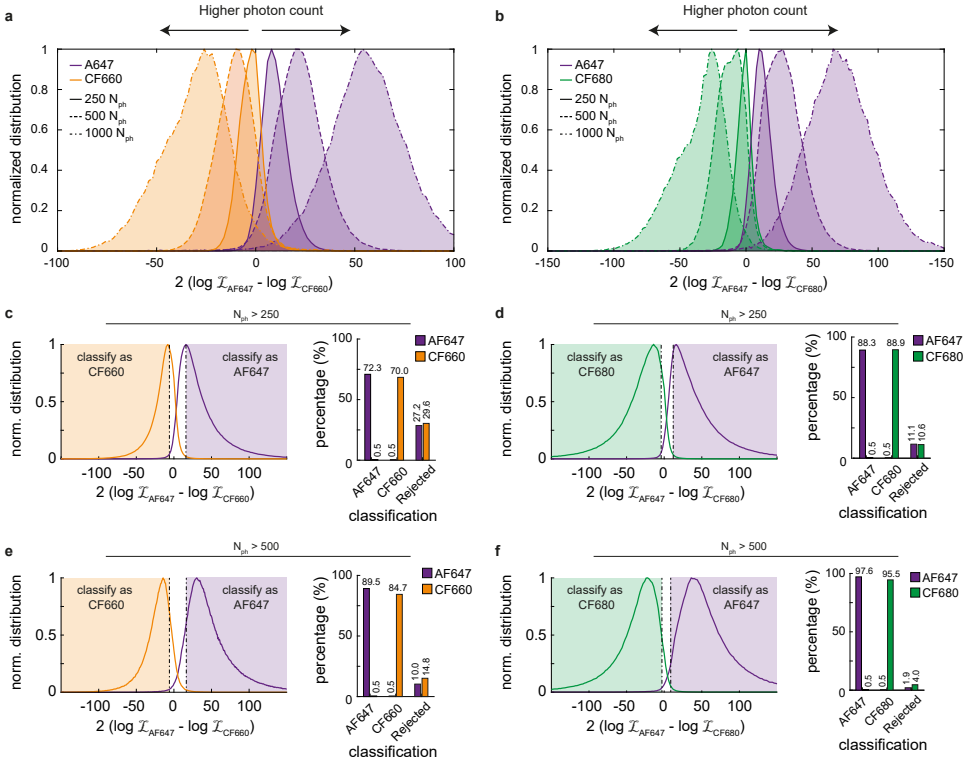

Figure 4.A.3: a&b) Normalized GLRT distribution for AF647 vs CF660 (a) and AF647 vs CF680 (b) binned for different photon counts. c&d) Normalized GLRT distribution (left) and classification rates (right) for all events with a total intensity of 250 or more. e&f) Normalized GLRT distribution (left) and classification rates (right) for all events with a total intensity of 500 or more.

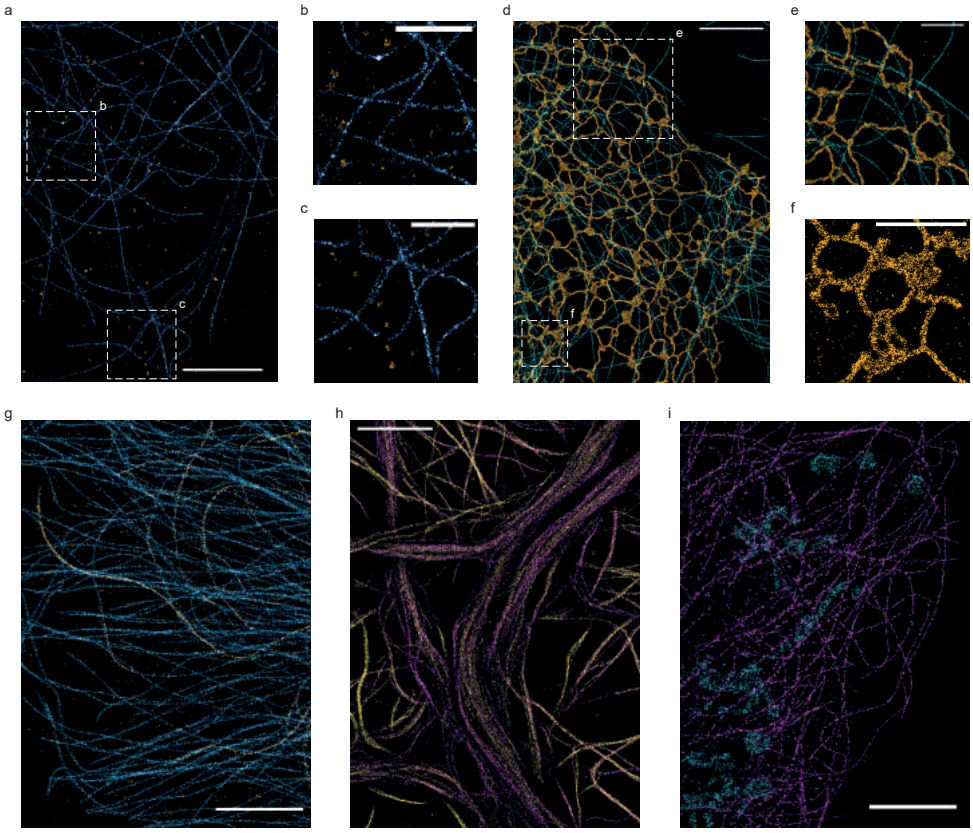

Figure 4.A.4: a) COS-7 cell stained for alpha-tubulin (AF647, cyan) and clathrin HC (CF660, orange). b&c) Zooms of a. d) COS-7 cells stained for ER (SEC61b-GFP overexpression, AF647, orange) and alpha-tubulin (CF680, cyan). e&f) Zooms of c. g) U2OS cells stained for tyrosinated tubulin (AF647, cyan) and acetylated tubulin (CF660, yellow). h) Div14 neuron stained for tyrosinated tubulin (AF647, magenta) and acetylated tubulin (CF660, yellow). j) COS-7 cell stained for alpha-tubulin (AF647, magenta) and cytochrome C (CF680, cyan). Scale bars indicate 5 μm (a,d,g,h,j) and 2 μm (b,c,e,f).

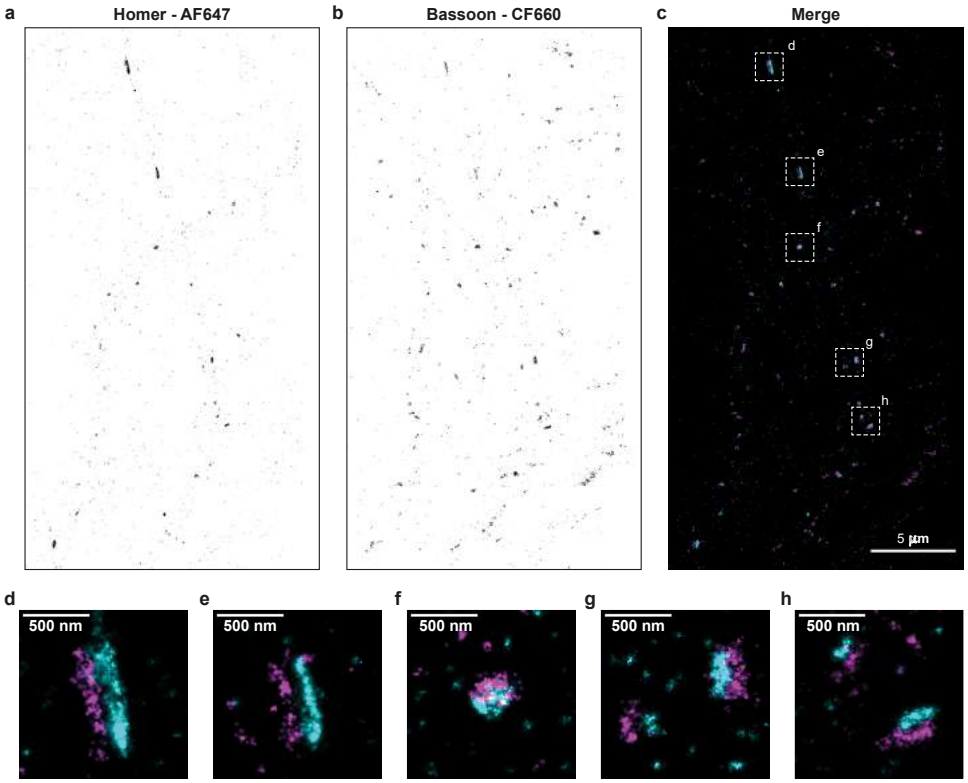

Figure 4.A.5: a) Reconstruction of Homer (magenta) stained with AF647. Insert shows widefield image. b) Reconstruction of Bassoon (cyan) stained with CF660. c) Merge reconstruction of a&b. d-h) Zooms of c.

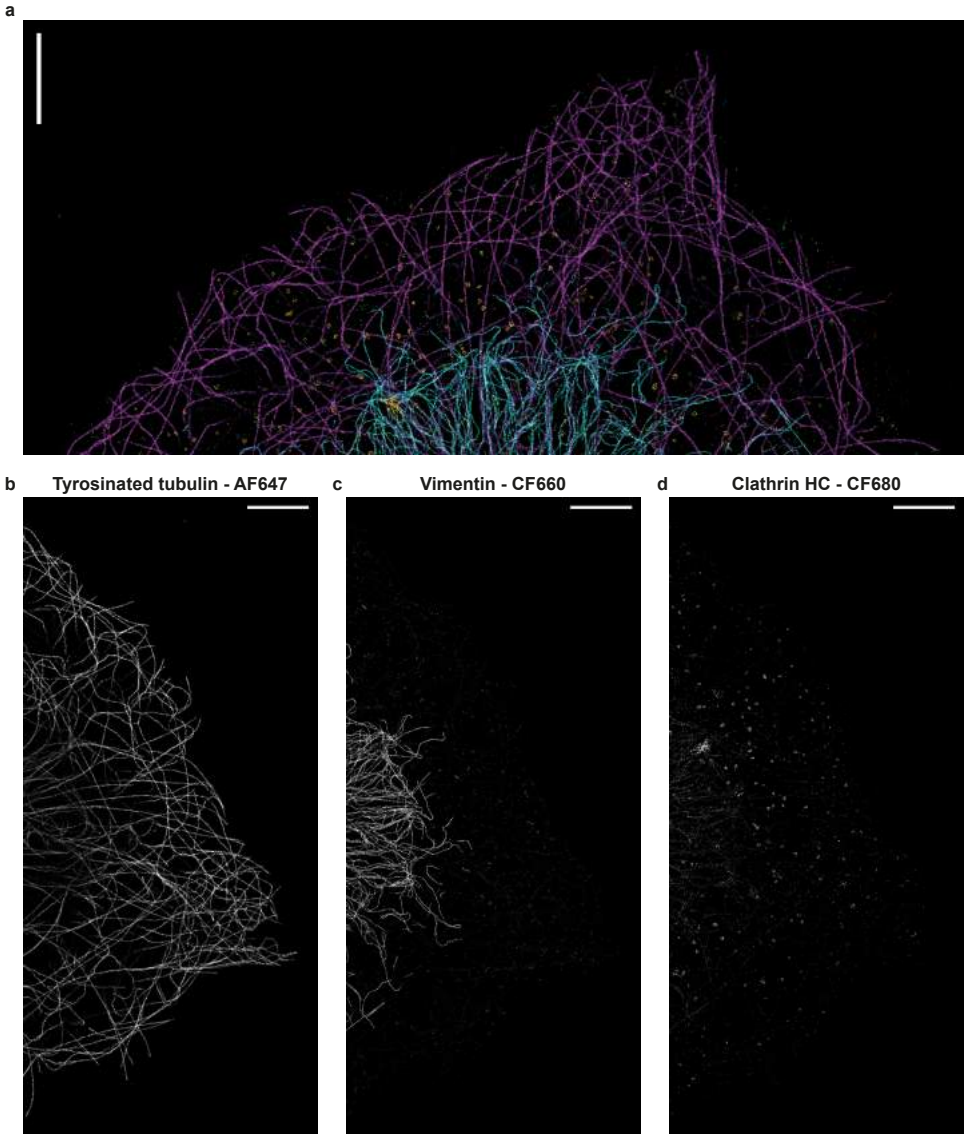

Figure 4.A.6: a-d) 3-colour PFC-dSTORM reconstruction of a COS7 cell stained for tyrosinated tubulin (AF647), vimentin (CF660) and Clathrin (CF680). a) Merge of all three channels. b-d) individual channels. All scale bars indicate 5 μm.

References

[1] M. J. Rust, M. Bates, and X. Zhuang, *Sub-diffraction-limit imaging by stochastic optical reconstruction microscopy (storm),* Nat Methods **3**, 793 (2006).

[2] E. Betzig, G. H. Patterson, R. Sougrat, O. W. Lindwasser, S. Olenych, J. S. Bonifacino, M. W. Davidson, J. Lippincott-Schwartz, and H. F. Hess, *Imaging intracellular fluorescent proteins at nanometer resolution,* Science **313**, 1642 (2006).

[3] S. T. Hess, T. P. Girirajan, and M. D. Mason, *Ultra-high resolution imaging by fluorescence photoactivation localization microscopy,* Biophys J **91**, 4258 (2006).

[4] S. van de Linde, A. Loschberger, T. Klein, M. Heidbreder, S. Wolter, M. Heilemann, and M. Sauer, *Direct stochastic optical reconstruction microscopy with standard fluorescent probes,* Nat Protoc **6**, 991 (2011).

[5] G. T. Dempsey, J. C. Vaughan, K. H. Chen, M. Bates, and X. Zhuang, *Evaluation of fluorophores for optimal performance in localization-based super-resolution imaging,* Nat Methods **8**, 1027 (2011).

[6] M. N. Bongiovanni, J. Godet, M. H. Horrocks, L. Tosatto, A. R. Carr, D. C. Wirthensohn, R. T. Ranasinghe, J. E. Lee, A. Ponjavic, J. V. Fritz, C. M. Dobson, D. Klenerman, and S. F. Lee, *Multi-dimensional super-resolution imaging enables surface hydrophobicity mapping,* Nat Commun **7**, 13544 (2016).

[7] M. J. Mlodzianoski, N. M. Curthoys, M. S. Gunewardene, S. Carter, and S. T. Hess, *Super-resolution imaging of molecular emission spectra and single molecule spectral fluctuations,* PLoS One **11**, e0147506 (2016).

[8] Z. Zhang, S. J. Kenny, M. Hauser, W. Li, and K. Xu, *Ultrahigh-throughput single-molecule spectroscopy and spectrally resolved super-resolution microscopy,* Nat Methods **12**, 935 (2015).

[9] C. Smith, M. Huisman, M. Siemons, D. Grunwald, and S. Stallinga, *Simultaneous measurement of emission color and 3d position of single molecules,* Opt Express **24**, 4996 (2016).

[10] D. Baddeley, D. Crossman, S. Rossberger, J. E. Cheyne, J. M. Montgomery, I. D. Jayasinghe, C. Cremer, M. B. Cannell, and C. Soeller, *4d super-resolution microscopy with conventional fluorophores and single wavelength excitation in optically thick cells and tissues,* PLoS One **6**, e20645 (2011).

[11] A. Lampe, V. Haucke, S. J. Sigrist, M. Heilemann, and J. Schmoranzer, *Multi-colour direct storm with red emitting carbocyanines,* Biol Cell **104**, 229 (2012).

[12] C. M. Winterflood, E. Platonova, D. Albrecht, and H. Ewers, *Dual-color 3d superresolution microscopy by combined spectral-demixing and biplane imaging,* Biophys J **109**, 3 (2015).

[13] Y. Zhang, L. K. Schroeder, M. D. Lessard, P. Kidd, J. Chung, Y. Song, L. Benedetti, Y. Li, J. Ries, J. B. Grimm, L. D. Lavis, P. De Camilli, J. E. Rothman, D. Baddeley, and J. Bewersdorf, *Nanoscale subcellular architecture revealed by multicolor three-dimensional salvaged fluorescence imaging,* Nat Methods **17**, 225 (2020).

[14] S. M. Kay, *Fundamentals of statistical signal processing*, Prentice Hall signal processing series (Prentice-Hall PTR, Englewood Cliffs, N.J., 1993).

[15] C. S. Smith, S. Stallinga, K. A. Lidke, B. Rieger, and D. Grunwald, *Probability-based particle detection that enables threshold-free and robust in vivo single-molecule tracking,* Molecular Biology of the Cell **26**, 4057 (2015).

[16] B. Huang, W. Wang, M. Bates, and X. Zhuang, *Three-dimensional super-resolution imaging by stochastic optical reconstruction microscopy,* Science **319**, 810 (2008).

[17] F. Huang, S. L. Schwartz, J. M. Byars, and K. A. Lidke, *Simultaneous multiple-emitter fitting for single molecule super-resolution imaging,* Biomed Opt Express **2**, 1377 (2011).

[18] M. Mikhaylova, B. M. Cloin, K. Finan, R. van den Berg, J. Teeuw, M. M. Kijanka, M. Sokolowski, E. A. Katrukha, M. Maidorn, F. Opazo, S. Moutel, M. Vantard, F. Perez, P. M. van Bergen en Henegouwen, C. C. Hoogenraad, H. Ewers, and L. C. Kapitein, *Resolving bundled microtubules using anti-tubulin nanobodies,* Nat Commun **6**, 7933 (2015).

[19] J. Nixon-Abell, C. J. Obara, A. V. Weigel, D. Li, W. R. Legant, C. S. Xu, H. A. Pasolli, K. Harvey, H. F. Hess, E. Betzig, C. Blackstone, and J. Lippincott-Schwartz, *Increased spatiotemporal resolution reveals highly dynamic dense tubular matrices in the peripheral er,* Science **354** (2016), 10.1126/science.aaf3928.

[20] Y. T. Guo, D. Li, S. W. Zhang, Y. R. Yang, J. J. Liu, X. Y. Wang, C. Liu, D. E. Milkie, R. P. Moore, U. S. Tulu, D. P. Kiehart, J. J. Hu, J. Lippincott-Schwartz, E. Betzig, and D. Li, *Visualizing intracellular organelle and cytoskeletal interactions at nanoscale resolution on millisecond timescales,* Cell **175**, 1430 (2018).

[21] R. Jungmann, M. S. Avendano, J. B. Woehrstein, M. Dai, W. M. Shih, and P. Yin, *Multiplexed 3d cellular super-resolution imaging with dna-paint and exchange-paint,* Nat Methods **11**, 313 (2014).

[22] K. H. Song, Y. Zhang, B. Brenner, C. Sun, and H. F. Zhang, *Symmetrically dispersed spectroscopic single-molecule localization microscopy,* Light Sci Appl **9**, 92 (2020).

[23] J. Jeffet, A. Ionescu, Y. Michaeli, D. Torchinsky, E. Perlson, T. Craggs, and Y. Ebenstein, *Multimodal single-molecule microscopy with continuously controlled spectral resolution,* Biophysical Reports **1** (2021), https://doi.org/10.1016/j.bpr.2021.100013.

[24] C. S. Smith, N. Joseph, B. Rieger, and K. A. Lidke, *Fast, single-molecule localization that achieves theoretically minimum uncertainty,* Nat Methods **7**, 373 (2010).

[25] C. G. Dotti, C. A. Sullivan, and G. A. Banker, *The establishment of polarity by hippocampal neurons in culture,* J Neurosci **8**, 1454 (1988).

[26] A. Chazeau, E. A. Katrukha, C. C. Hoogenraad, and L. C. Kapitein, *Studying neuronal microtubule organization and microtubule-associated proteins using single molecule localization microscopy,* Neuronal Cytoskeleton, Motor Proteins, and Organelle Trafficking in the Axon **131**, 127 (2016).

[27] A. Provost, C. Rousset, L. Bourdon, S. Mezhoud, E. Reungoat, C. Fourneaux, T. Bresson, M. Pauly, N. Beard, L. Possi-Tchouanlong, B. Grigorov, P. Bouvet, J. J. Diaz, C. Chamot, E. I. Pecheur, C. Ladaviere, M. T. Charreyre, A. Favier, C. Place, and K. Monier, *Innovative particle standards and long-lived imaging for 2d and 3d dstorm,* Sci Rep **9**, 17967 (2019).

[28] A. Jabermoradi, S. Yang, M. Gobes, J. P. van Duynhoven, and J. Hohlbein, *Enabling single-molecule localization microscopy in turbid food emulsions,* bioRxiv , 2021.03.03.433739 (2021).

[29] B. Rieger and S. Stallinga, *The lateral and axial localization uncertainty in super-resolution light microscopy,* Chemphyschem : a European journal of chemical physics and physical chemistry **15** (2014), 10.1002/cphc.201300711.

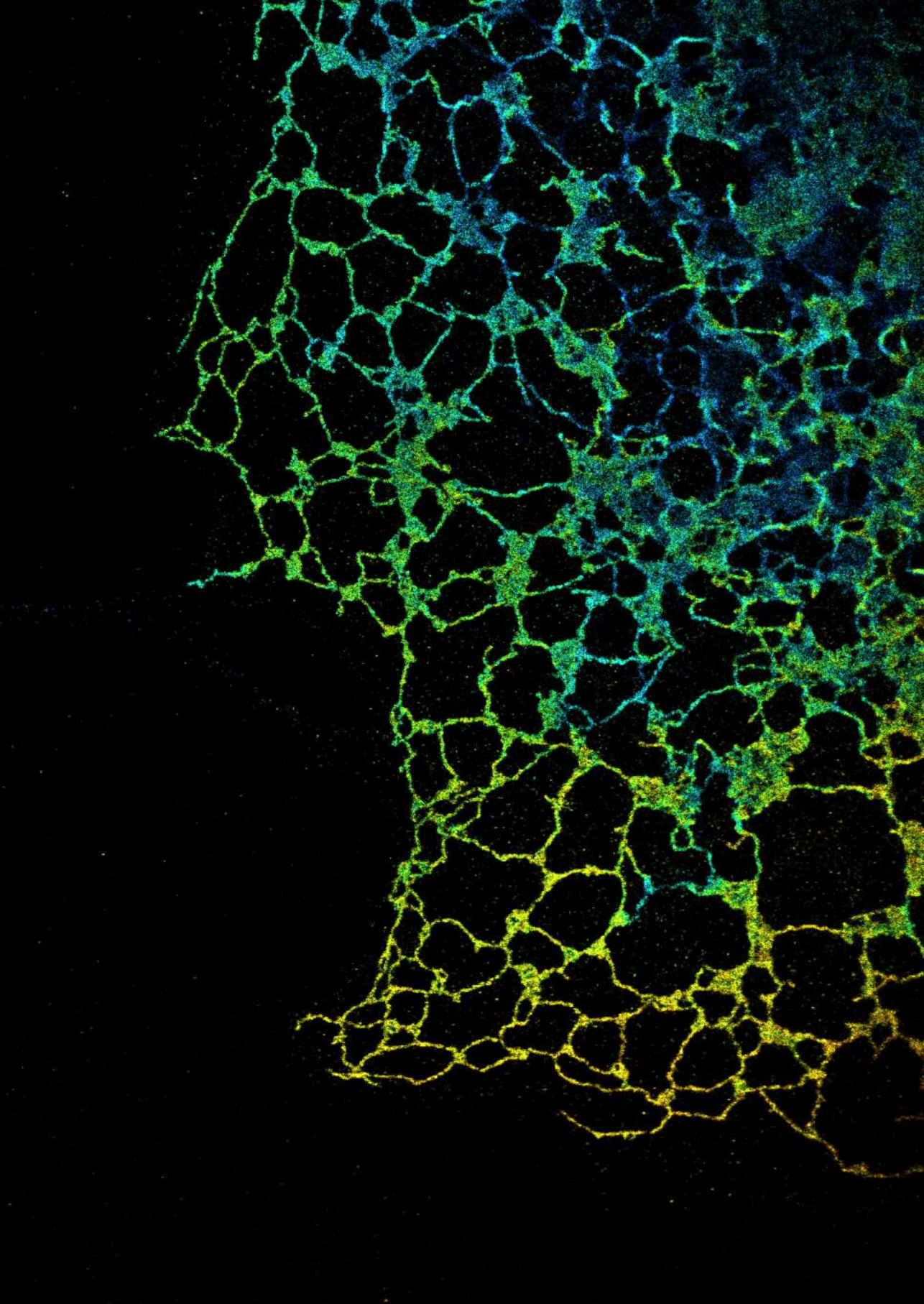

5

On the z-accuracy in 3D single-molecule localization microscopy

Single-molecule localization microscopy has developed into a widely used technique to overcome the diffraction limit and enables 3D localization of single-emitters with nanometer precision. A widely used method to enable 3D encoding is to use a cylindrical lens or a phase mask to engineer the Point Spread Function (PSF). The performance of these PSFs is often assessed by comparing the precision they achieve, ignoring accuracy. Nonetheless, accurate localization is required in many applications, such as multi-plane imaging, measuring and modelling of physical processes based on volumetric data and 3D particle averaging. However, in many applications there are PSF model mismatches due to how reference PSFs are obtained, Look-Up-Tables are created or spots are fitted. Currently there is little insight in how these model mismatches give rise to systematic axial localization errors, how large these errors are and how to mitigate these. In this theoretical and simulation work we use a vectorial PSF model, which incorporates Super-critical Angle Fluorescence (SAF) and the appropriate aplanatic correction factor, to analyse the errors in z-localization. We introduce theory for defining the focal plane in SAF conditions and analyse the predicted axial errors for an astigmatic PSF, Double Helix PSF and Saddle Point PSF. Finally, we discuss potential experimental methods to verify these findings and propose a workflow to mitigate these effects.

This chapter is currently being prepared for submission.

5.1 Introduction

Single-Molecule Localization Microscopy (SMLM) [1–3] is a super-resolution microscopy modality that overcomes the diffraction limit by localization of sparse emitting fluorophores. The lateral position of a single-molecule is estimated from a blinking event by fitting the spot with a 2D Gaussian which resembles an ideal unmodified Point Spread Function (PSF). More advanced SMLM implementations modify or engineer the PSF to encode for other parameters of interest, such as the z-position [4], wavelength [5] or orientation [6]. The most common way for z-encoding in 3D SMLM is the use of PSF engineering by a cylindrical lens for astigmatic z-encoding. Other popular engineered PSFs are the Double-Helix PSF (DH-PSF) [7–9] and TetraPod [10] or Saddle-Point PSF (SP-PSF) [11]. For 3D SMLM with PSF engineering, a calibration PSF is obtained by scanning a small fluorescent bead with a z-stage over a suitable range. This calibration PSF is then used to create a LUT [4], a cubic spline model [12], or used as input to create a PSF with a scalar model used for direct fitting [11] or for training a neural network [13].

However, the calibration PSF is obtained by acquiring a through focus scan of a small fiducial marker by moving the z-stage, instead of the PSF a fluorophore would exhibit with different z-positions inside the sample. This results in a different defocus aberration and therefore a different PSF. Moreover, often high NA TIRF objectives are used which captured the super-critical angle fluorescence (SAF) alongside the under-critical angle fluorescence (UAF). The SAF depends strongly on the absolute distance from the coverslip, resulting in a strong z-dependent apodization in the pupil. The calibration PSF therefore differs in SAF and defocus aberration from the 'true' PSF exhibited by an emitter. Current implementations using engineered PSFs either do not make such a distinction between calibration and emitter PSF or use PSF models which are scalar, don't include SAF or Fresnel reflections, don't use the correct aplanatic correction factor or even ignore more than one of these effects. Another method to estimate the z-position of the fluorophore is to measure the ratio between the UAF and SAF [14–16]. This method allows for accurate z-position estimation but can only be used close to the coverslip ($<$ 500 nm) and requires a complicated set-up. Therefore the currently most popular method for 3D localization is astigmatic PSF engineering, which can be easily implemented by inserting a cylindrical lens at the emission port of the microscope.

Most assessments of localization method performance focus on the best possible precision, as quantified by the Cramér-Rao lower bound, while little attention is paid to accuracy, the absence of bias in the parameter estimation. In some cases inaccurate 3D SMLM is sufficient to gain basic insight, but accurate z-localization is important in many biological cases and studies. It is crucial to have accurate 3D information when the super-resolution volume is used for the modelling of physical processes and forces, for instance in focal adhesion sites [17] or neuronal synapses [18]. This is especially the case when these 3D nano-organizations can be correlated to other measurable quantities, such as action potentials [19] or diffusion [20, 21]. Axial accuracy is also important for multi-plane SMLM [22, 23], where multiple focal planes have to be stitched together. Lastly, accurate localization is important in 3D particle averaging, where even small relative axial biases are noticeable, as

these methods can achieve resolutions down to 10 nm [24].

To date, z-accuracy in 3D SMLM has not been quantified or explored in great detail, but there have been attempts to address this issue. Recently proposed experimental calibration methods use a sample with fluorescent beads embedded in a gel or on top of polymer coating in order to create LUTs at different depths [25, 26]. However, the method by Li et al. [25] can only be applied for astigmatic PSFs and relates the LUTs with respect to the position when a bead is in focus by stage movement. There is therefore a mismatch between the LUT and the emitter PSF. The calibration method proposed by Petrov and Moerner [26] does not have these pitfalls as the imaging depth is well defined and arbitrary PSFs can be used. However, in that case the PSF is acquired by stage-movement, which again induces a mismatch between the calibration PSF and the true emitter PSF.

For that reason there is a need for accurate z-localization with PSF engineering and, in general, insight in how large these axial errors are. In this theoretical work we use a vectorial PSF model, which includes SAF and the appropriate aplanatic correction factor, to analyse the accuracy in z-localization. We introduce theory for defining the plane of best focus in SAF conditions and analyse the predicted axial errors for an astigmatic PSF, DH-PSF and SD-PSF. Finally we discuss potential experimental methods to verify these findings and propose a workflow to mitigate these effect.

5.2 Theory

5.2.1 Vector PSF model

A vector PSF model that includes Fresnel coefficients has been described in earlier work [27]. In short, the rotation matrix $\mathbf{R}(\rho_x, \rho_y)$ describes how the x, y, and z-component of the emitted electric field $\mathbf{E}^{\text{object}}$ in the object plane are transferred by the objective lens (see Figure 5.2.1a) to the electric field in the pupil plane $\mathbf{E}^{\text{pupil}}$

$$\mathbf{E}^{\text{pupil}} = \mathbf{R}(\rho_x, \rho_y)\mathbf{E}^{\text{object}} \tag{5.1}$$

with ρ_x and ρ_y the normalized pupil coordinates. The z-component of the electric field in the pupil is ignored, as this component gives a contribution to the spot focused by the tube lens on the camera that scales with the square of the (low) NA of the tube lens, which can therefore be neglected. The 6 components of the electric field at the pupil with (additional) phase aberration $W(\rho_x, \rho_y)$ are given by

$$\begin{aligned} E_{l,j}^{\text{pupil}}(W) &= \frac{1}{w_n} A q_{l,j} \exp\left[iW\rho_x, \rho_y)\right] \\ &= \frac{1}{w_n} A q_{l,j} \exp\left[iW_{\text{eng}}(\rho_x, \rho_y) + i(dk_z^1 - z_{\text{stage}}k_z^3 - z_{\text{pos}}k_z^\alpha)\right] \end{aligned} \tag{5.2}$$

with $W_{\text{eng}}(\rho_x, \rho_y)$ the phase corresponding to the engineered PSF, $q_{l,j}$ the polarization vector component that includes the Fresnel-coefficients for the interfaces between the different media (sample, cover slip, immersion oil) and $\vec{k}$ the wavevector with $k_{x/y} = 2\pi \text{NA}\rho_{x/y}/\lambda$ and $k_z^\alpha = 2\pi\sqrt{n_\alpha^2 - \text{NA}^2\rho^2}/\lambda$, with $\alpha = 1$ for

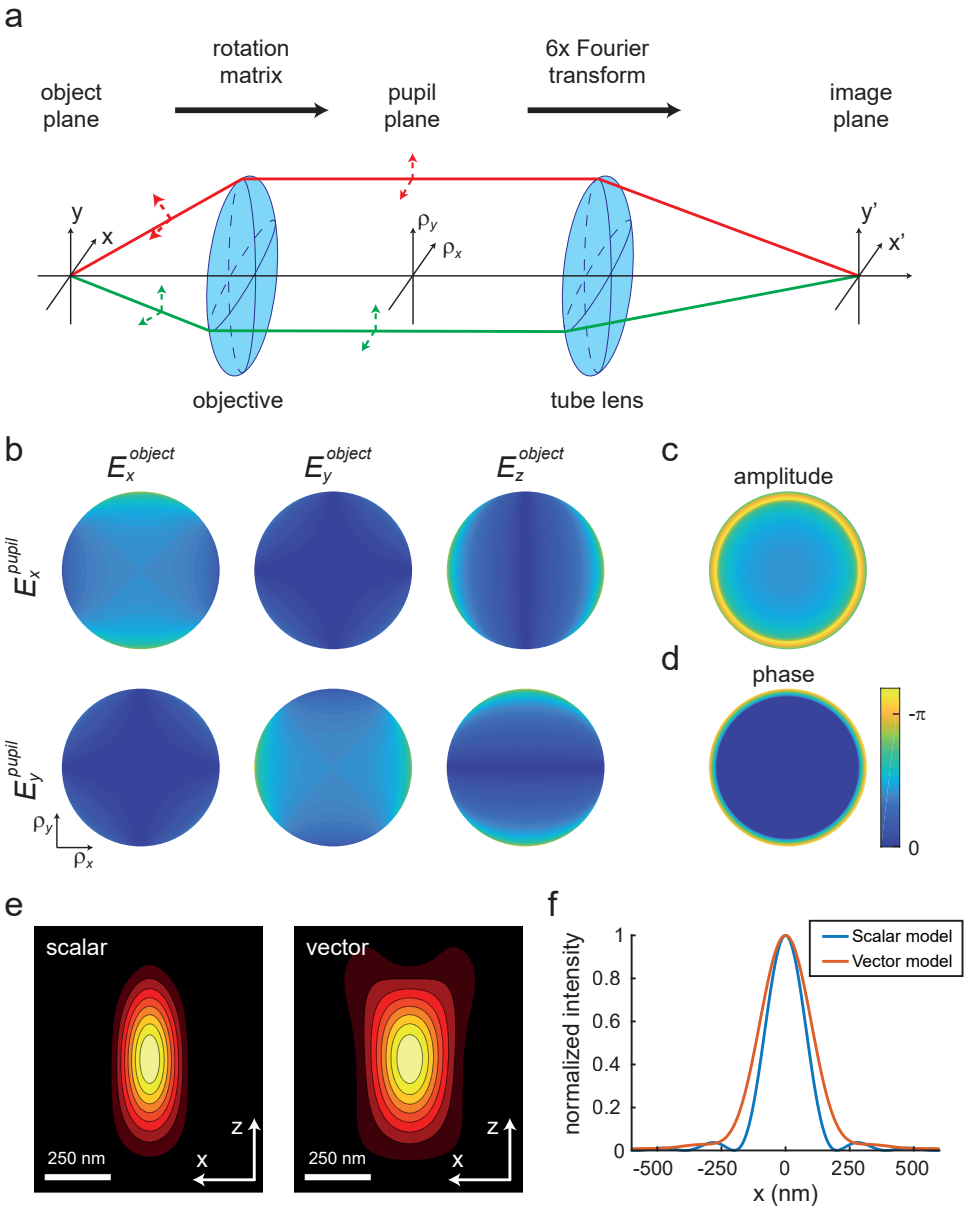

Figure 5.2.1: Illustration of the vectorial PSF model and the difference with a scalar PSF model. a) The electric field emitted at the object plane is rotated by the objective lens to the pupil plane, resulting in 6 electric field components in the pupil plane. The electric field in the image plane is computed by a Fourier transform. b) The amplitude of the 6 components of the electric field for an emitter at the coverslip with a TIRF objective (1.49 NA) (phase not shown). c&d) The amplitude (c) and phase (d) of the electric field in the case of a scalar model. e) Scalar and vectorial PSF of the models shown in (b) and (c&d) with stage movement. f) Comparison of the scalar and vectorial PSF model in focus.

the mounting medium and $\alpha = 3$ for the immersion oil. d is the distance between the coverslip and the focal plane inside the sample, z_{stage} denotes the corresponding z-stage position with that focal plane, and z_{pos} is the difference of the emitter with respect to the focal plane either by movement of the stage ($k_z^\alpha = k_z^3$) or movement inside the mounting medium ($k_z^\alpha = k_z^1$) and w_n is a normalized factor defined elsewhere. In the case of movement inside the mounting medium, z_{pos} needs to be smaller than the imaging depth d to have a physically meaningful result. A is a correction factor for imaging with a refractive index medium mismatch and is given by

$$A = \sqrt{\frac{n_{\text{imm}} \cos\left(\theta_{\text{imm}}\right)}{n_{\text{med}} \cos\left(\theta_{\text{med}}\right)}} \frac{1}{\sqrt{n_{\text{med}} \cos\left(\theta_{\text{med}}\right)}} = \frac{\left(n_{\text{imm}}^2 - \text{NA}^2 \rho^2\right)^{1/4}}{\left(n_{\text{med}}^2 - \text{NA}^2 \rho^2\right)^{1/2}} \tag{5.3}$$

where the first part corrects for the wave compression between the mounting medium – glass – immersion oil interface and the second is the aplanatic amplitude correction factor. The incoherent PSF H , arising from electric dipole emission of a fast rotating dipole, is then computed by quadratically adding the 6 Fourier transforms of the electric field components in the pupil

$$H(x,y) = \frac{N}{3} \sum_{l=x,y} \sum_{j=x,y,z} \left| \int_{|\rho^2|<1} E_{l,j}^{\text{pupil}} \exp\left[-i(k_x x + k_y y)\right] d^2\rho \right|^2 \tag{5.4}$$

with N the number of photons emitted. To illustrate the effects of high NA imaging on the PSF we compared this to a scalar model (see appendix for details of this scalar model). This scalar model has the same correction factor A and includes Fresnel-coefficients in order to include the SAF (see Figure 5.2.1c&d for the amplitude and the phase of the electric field). The comparison of the two models (see Figure 5.2.1e&f) shows that the scalar model significantly deviates from the vector model and exhibits more interference fringes. The vector PSF does not resemble an Airy disk, but is more akin to a Gaussian with a shoulder

5.2.2 The focal plane in SAF conditions

The plane of best focus of an imaging system is commonly defined as the plane where the root-mean-square wave-front distortion W_{rms} is minimal. However, when imaging in a condition with a strong apodization in the pupil plane, not all aberrations contribute equally to the PSF. To incorporate both the amplitude and phase variations across the pupil, we propose an optimization metric based on the Strehl-ratio to find the nominal focus plane. The optimal z-stage position corresponding to a focal plane with an imaging depth d from the coverslip (see Figure 5.2.2a) according to this metric can be found by

$$\max_{z_{\text{stage}}} S\left(W_{\text{eng}} + dk_z^1 - z_{\text{stage}} k_z^3 | W_{\text{eng}}\right) \tag{5.5}$$

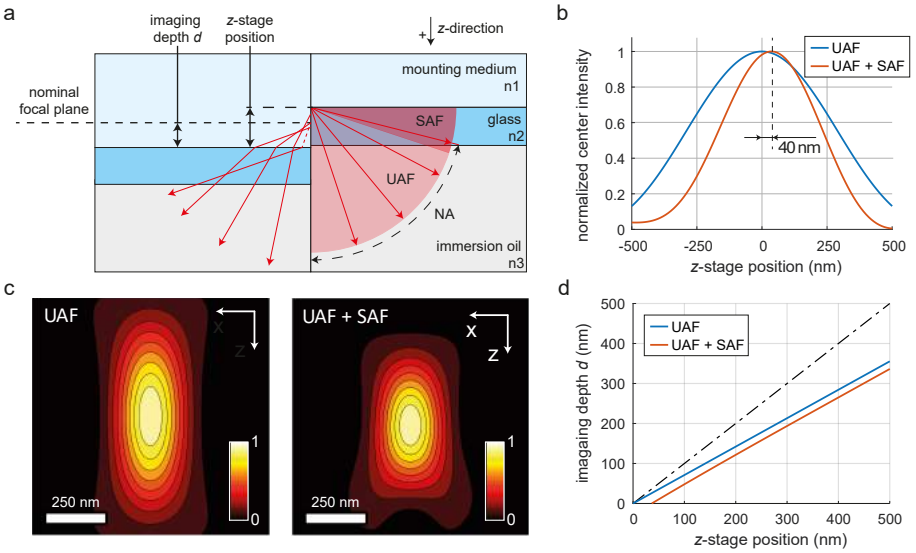

Figure 5.2.2: Effect of Super-critical Angle Fluorescence (SAF) on the focal plane. a) Illustration of the definitions in this work. The dotted line illustrates the complex wave-vector of the evanescent wave. b) The maximum intensity occurs at a z-stage position of 40 nm when the SAF is included. c) comparison between the PSF with only under-critical angle fluorescence (UAF) and in the case of UAF and SAF. The latter exhibits a more compact PSF and is axially asymmetric. d) the imaging depth d as function of the z-stage position.

where we define the relative Strehl-ratio $S(W_1|W_2)$ as

$$S\left(W_1|W_2\right) = \frac{\sum_{l=x,yj=x,y,z} \left| \int_{\rho^2<1} d^2\rho E_{l,j}^{\text{pupil}}(W_1) \right|^2}{\sum_{l=x,yj=x,y,z} \left| \int_{\rho^2<1} d^2\rho E_{l,j}^{\text{pupil}}(W_2) \right|^2} \tag{5.6}$$

We implemented this optimization scheme by computing this ratio over a range of z-positions near an initial estimated value ($z_{\text{stage}} = dn_3/n_1$). The optimum is found by fitting a second order polynomial around the maximum value. The results of this procedure are shown in Figure 2b.

This analysis reveals that for focussing an isotropically emitting dipole at the coverslip, the optimal z-stage position deviates 40 nm from zero. To illustrate that this effect is purely caused by the SAF we simulated a PSF with z-stage movement with only under-critical angle fluorescence UAF (NA = 1.33) and UAF + SAF (NA = 1.49) as shown in Figure 5.2.2. The UAF PSF is symmetric around the focal plane, whereas the focal plane for the SAF + UAF PSF is shifted and the PSF appears asymmetric. Therefore, the z-stage needs to be adjusted to reduce the phase difference between the SAF and the UAF for optimal focussing. As expected, the difference between the SAF+UAF and UAF nominal focus planes reduces when focussing deeper into the sample as shown in Figure 5.2.2d.

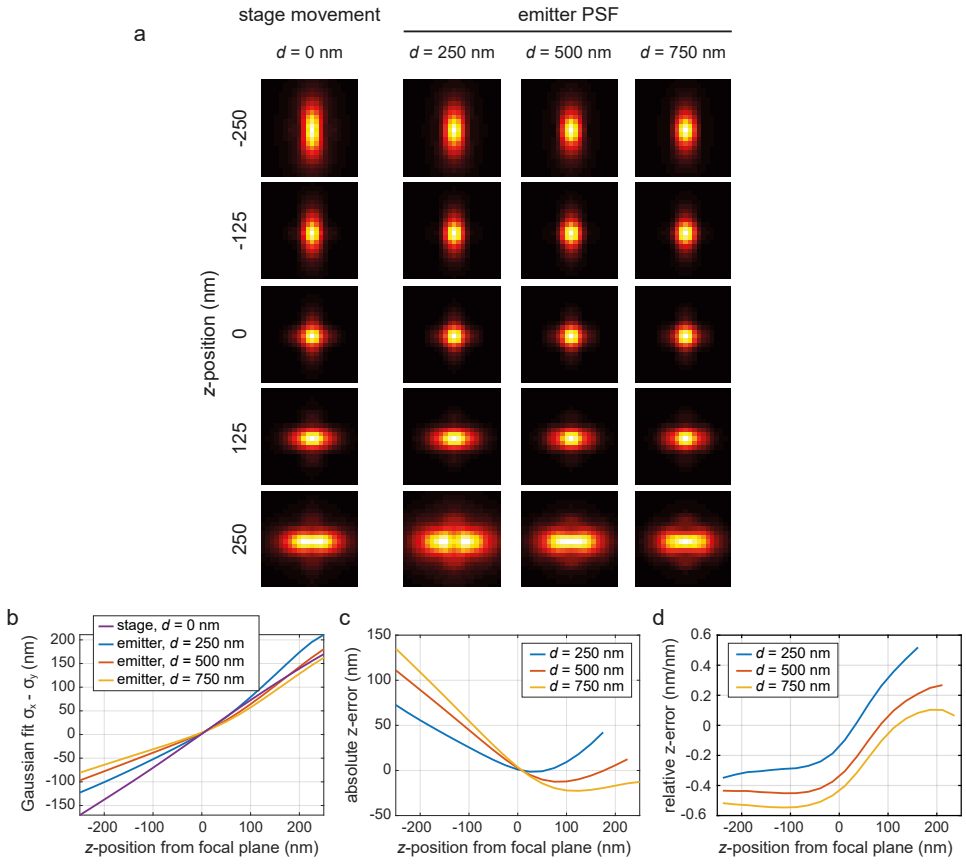

Figure 5.2.3: a) Astigmatic PSF with A22 = 60 nm (rms amplitude) with stage-movement at an imaging depth of 0 nm (left) and different axial position with respect to the focal plane for imaging depths of 250, 500 and 750 nm (right). b) LUTs of the PSFs of (a) by Gaussian fitting. c) absolute z-error when using a LUT of the stage movement PSF for estimating the z-position at different imaging depths. d) Relative axial error of (c) in nm error per nm distance.

It turns out that optimizing the Strehl ratio for finding the nominal focus plane only works when the phase for PSF engineering is small compared to the wavelength ($W_{\text{rms}} < 0.1\lambda$) and does not contain a phase singularity in the centre. Therefore this methods can find the correct focal plane in the case of an astigmatic PSF, but fails to find the focal plane in the case for a Saddle-Point and Double-Helix PSF. To find the focal plane in these cases the PSF engineering phase should be disregarded during the optimization, except modes which affect the focal plane position (i.e. Zernike modes with azimuthal order of 0 such as Z_2^0, Z_4^0, etc).

5.3 Simulation Results

We next explored the effect of the SAF and spherical aberration on z-encoding for three types of engineered PSFs: an astigmatic PSF, a Saddle-Point PSF (SP-PSF) and a Double-Helix PSF (DH-PSF). So far we examined the PSF when the z-stage is moved. However, when performing SMLM the z-stage remains fixed, while emitters have a different position with respect to the focal plane. This change is position has a different associated z-component of the wave-vector as well as a z-position dependent apodization due to the SAF. The calibration PSF acquired by moving the z-stage is therefore inherently different than the true PSF that represents the 3D position inside the mounting medium. In the following we term the PSF obtained by movement of the z-stage at zero imaging depth 'stage-movement PSF' and the true emitter PSF representing 3D position inside the mounting medium 'emitter PSF'. This corresponds to a multiplication of the z-position with the z-component of the wave-vector in either immersion oil (k_z^3) or mounting medium (k_z^1) respectively (Eq. 5.2). All simulations are, unless specified differently, performed with the following parameters: λ = 550 nm, pixel size = 100 nm, NA = 1.49, n_{med} = 1.33 and n_{imm} = 1.52. We have simulated the error in the estimated z-position when not correcting for these differences in axial wave-vector components.

5.3.1 Astigmatic z-encoding

For the case of astigmatic z-encoding we simulated a calibration PSF by simulating a small bead on the coverslip (imaging depth = 0 nm) with stage-movement and compared this to the emitter PSFs at three imaging depths (250, 500 and 750 nm), see Figure 5.2.3. The stage-movement PSF has an almost axially symmetric ellipticity (Figure 5.2.3a), resulting a linear Look-Up-Table (LUT) as shown in Figure 5.2.3b. In contrast, the emitter PSF with an imaging depth of 250 nm exhibits large deviations from a 2D Gaussian function near the coverslip. This effect reduces for larger imaging depths (500 & 750 nm), but deviations from the LUT now occur away from the coverslip (negative z-positions) caused by spherical aberration and the reduction of the effective NA caused by the diminishing SAF. Using the calibration LUT for z-localization of the estimated width ratios result in underestimation of the true z-position up to 140 nm (56%). Furthermore, the relative axial errors range between 0.3 nm and 0.5 nm per nm distance over a range of hundreds of nanometers, see Figure 5.2.3d. This implies that medium sized structures of 100 nm can already accumulate up to 50% of relative axial error.

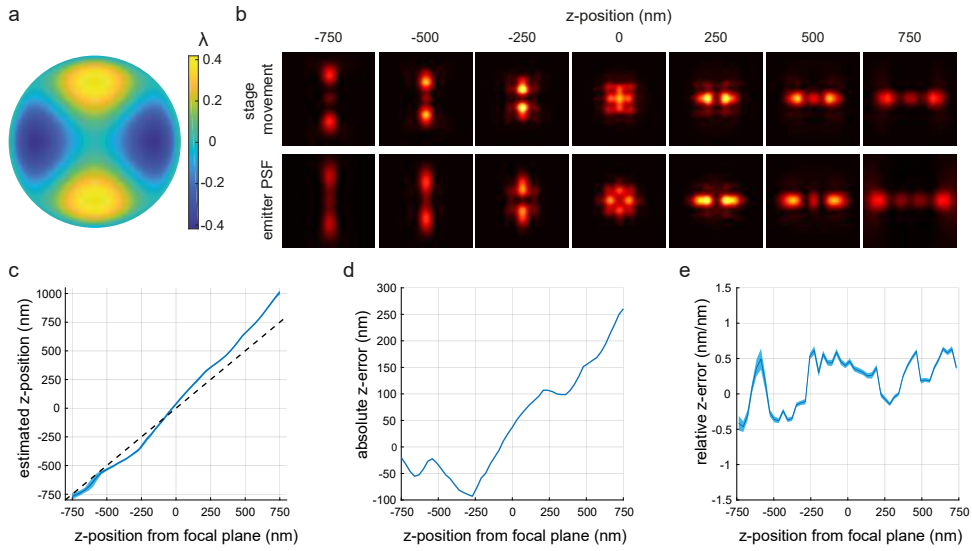

Figure 5.3.1: a) Phase profile of the Saddle-point PSF. b) Stage-movement PSF at an imaging depth of 0 nm (top) and emitter PSF (bottom) at an imaging depth of 750 nm. Z-position denotes either the movement with the stage or position inside the mounting medium. Pixel size = 10 nm . c) Estimated z-position for the saddle-point PSF using the stage-movement PSF model to fit the true emitter PSF. Colored region indicates standard deviation of the estimated positions. d) Absolute axial error of (c). e) Relative axial error of (c). Shaded region indicates standard error of the mean.

5.3.2 Saddle Point and Double Helix PSF

We performed a similar analyses for the Saddle Point and Double Helix PSFs, optimized for an axial range of 1500 nm. We simulated the stage-movement PSF and compared this to the emitter PSF with an imaging depth of 750 nm and z-range of ±750 nm. We will first discuss the Saddle-Point PSF.

We engineered the SD-PSF with Zernike modes Z_2^2 and Z_4^2 with amplitude 150 mλ and -148 mλ respectively (rms amplitude), values that were obtained by CRLB optimization. The phase of this SD-PSF is shown in Figure 5.3.1a. The stage-movement PSF deviates visually strikingly from the emitter PSF as shown in Figure 5.3.1b. The emitter PSF exhibits a different pattern in the focal plane and has differently structured lobes in the extreme z-positions. To quantify the axial accuracy we simulated N = 100 noisy emitter PSFs per z-position with 2500 signal photon counts and 10 background photon counts per pixel and fitted these with the calibration PSF model. Figure 5.3.1c shows the fitted z-position as function of the true axial position. The z-accuracy appears to be non-linear over the axial range and deviates strongly close to the coverslip (<500nm). Strikingly, this analyse predicts absolute z-errors of more than 250 nm. Around focus, the relative error is about 0.5 nm/nm over a 500 nm range, which would result in a 250 nm sized structured to be overestimated by 125 nm.

We next explored the accuracy for the Double Helix PSF. There are two popular ways to construct this PSF; using Gaussian-Laguerre modes [7] or using rings of

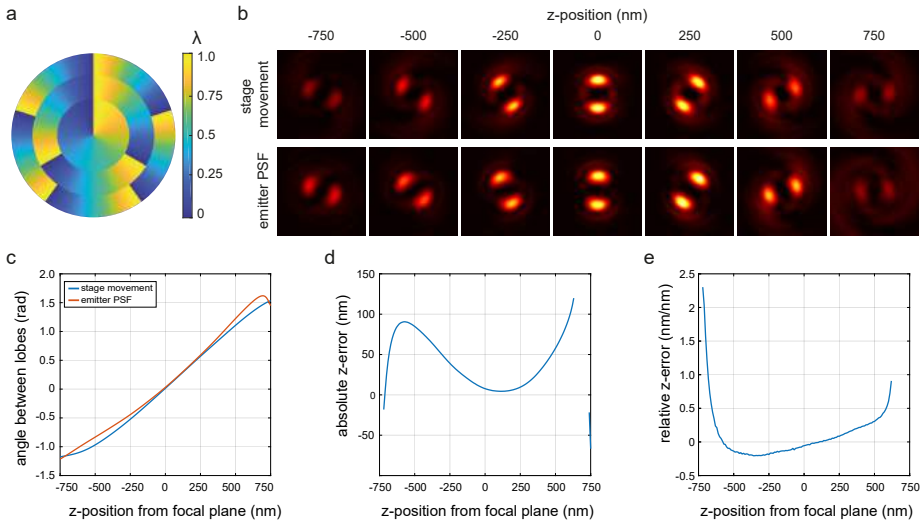

Figure 5.3.2: a) Phase profile of the Double-Helix PSF. b) Stage-movement PSF at an imaging depth of 0 nm (top) and emitter PSF (bottom) at an imaging depth of 750 nm. Z-position denotes either the movement with the stage or position inside the mounting medium. Pixel size = 10 nm . c) Angle between the two lobes for the stage-movement and emitter PSF. d) Absolute axial error of (c). e) Relative axial error.

azimuthal ramps [8, 9]. Here we engineered the DH-PSF with 3 rings of azimuthal ramps with increasing slope with a ring radius ratio α of $4/5$ resulting in a 2π rotation in 1500 nm. The phase of this PSF is shown in Figure 5.3.2a.

In the case of the DH-PSF there were no striking visual differences when comparing the stage-movement PSF and emitter PSF (see Figure 5.3.2b), but there was a noticeable difference in the angle between the lobes. We measured the axial accuracy by analysing the angle between the position of the maximum intensity of the two lobes as function of the z-position. Figure 5.3.2c shows that the angle of the emitter PSF deviates from the stage movement PSF and even rotates outside the calibration range near the coverslip. The largest measured absolute axial error is 120 nm, which is similar to the astigmatic PSF, but this axial error is accumulated over a larger z-range. The relative error for this DH-PSF is small compared to both the astigmatic PSF and SD-PSF, especially near the focus plane (±250 nm). The DH-PSF is therefore the most accurate form of PSF engineering out of these three PSFs.

5.4 Discussion

Despite the clear need for accurate axial localization to extend the useability of 3D SMLM, this topic has not yet been studied in great detail. The simulations performed in this work show that using the calibration PSF acquired by stage movement results in significant biases in the estimated z-position when performing 3D SMLM. These biases result from apodization in the pupil due to super-critical angle fluorescence and spherical aberration induced by the mismatch between immersion

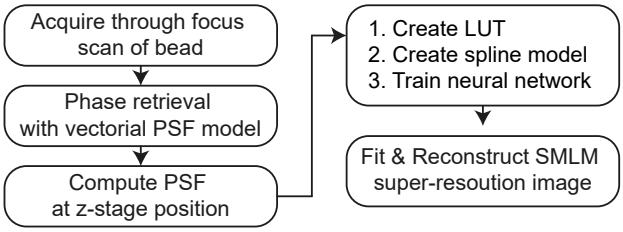

Figure 5.4.1: Proposed workflow for accurate 3D single-molecule localization microscopy with PSF engineering.

oil and the mounting medium. This leads to sizeable inaccuracies in z, which can amount to absolute z-errors of more than 140 nm in the case of an astigmatic PSF, 250 nm in the case of SD-PSF and 120 nm in the case of DH-PSF. The relative z-errors with an astigmatic PSF and SP-PSF differ across the z-range but can be as large as 50% over ranges of tenths to hundreds of nanometers. Therefore, relative axial errors can accumulate to 50 nm or more. These simulation furthermore indicate that the DH-PSF has the best axial accuracy, especially in a ±250 nm range around the focal plane. This is in line with other work analysing aberration sensitivity [28, 29].

The substantial biases predicted by this model can be experimentally verified in a number of ways. One option is to use a large coated spherical surface, where the axial position can be derived from the lateral position [30]. It is important that the refractive index of the bead matches with the mounting medium in order to reduce aberrations introduced by the bead. Polystyrene beads with a high refractive index (n = 1.7) will therefore likely introduce aberrations as the fluorescence Is collected partially through the bead. Another verification method is to use a setup which uses the ratio of the UAF and UAF + SAF to accurately measure the axial position while simultaneously measure the engineered PSF in a third channel. A downside of this method that it only works close to the coverslip. Nonetheless, with such an approach it would be possible to verify a substantial part of the predictions in this work.

If these findings are indeed experimentally verified, all these effects can in principle be mitigated by fitting the spots directly with this vector PSF model. However, due to the complexity of this model, this is slow compared to other fitting algorithms. We therefore propose to use the following work flow (see Figure 5.4.1). First a calibration PSF is acquired using a bead on the coverslip in the sample. Next a vectorial PSF based phase retrieval algorithm is used to estimate the aberrations precisely and accurately. This phase is then used to compute the emitter PSF for a certain z-stage position. This emitter PSF can then be used to create a LUT, a cubic spline model or train a neural network for fitting. We hope that this work will contribute to improve axial accuracy in SMLM to improve 3D reconstructions and gain better insight into biological processes.

5.A Appendix

5.A.1 Scalar PSF model

The scalar PSF model H_{scalar} uses normalized pupil coordinates $\rho_{x/y}$ for imaging an (isotropic) emitter inside a mounting medium (n_1), though a cover glass (n_2) and immersion oil (n_3) and is given by

$$H_{\text{scalar}}(x,y) = \left| \frac{1}{\pi} \int_{|\rho^2|<1} d^2\rho E\left(\rho_x, \rho_y\right) \exp\left[-ik_x x + k_y y\right] \right|^2 \tag{5.7}$$

with $E(\rho_x, \rho_y)$ the electric field in the pupil given by

$$E\left(\rho_x, \rho_y\right) = A\sqrt{T} \exp\left[\frac{2\pi i W(\rho_x, \rho_y)}{\lambda} + i\left(dk_z^1 - z_{\text{stage}} k_z^3 - z_{\text{pos}} k_z^\alpha\right) \right] \tag{5.8}$$

Here $W_{\text{eng}}(\rho_x, \rho_y)$ is the phase corresponding to the engineered PSF, $\vec{k}$ is the wavevector with $k_{x/y} = 2\pi \text{NA} \rho_{x/y}/\lambda$ and $k_z^\alpha = 2\pi\sqrt{n_\alpha^2 - \text{NA}\rho^2}/\lambda$, d is the distance between the coverslip and the focal plane inside the sample, z_{stage} the corresponding z-stage position with that focal plane, and z_pos the difference of the emitter w.r.t. the focal plane either by movement of the stage ($k_z^\alpha = k_z^3$) or movement inside the mounting medium ($k_z^\alpha = k_z^1$). A is a correction factor for imaging with a refractive index medium mismatch and is the same as equation 5.3. The intensity transmission T governed by the Fresnel-coefficients is given by

$$T = \frac{1}{2} t_{s,1\to2}^2 t_{s,2\to3}^2 + \frac{1}{2} t_{p,1\to2}^2 t_{p,2\to3}^2 \tag{5.9}$$

with $t_{s,i\to j}$ the Fresnel-coefficient for s-polarization between interface $n_i \to n_j$

$$t_{s,i\to j} = \frac{2n_i \cos\left(\theta_i\right)}{n_j \cos\left(\theta_j\right) + n_i \cos\left(\theta_i\right)} \tag{5.10}$$

and $t_{p,i\to j}$ the Fresnel-coefficient for p-polarization between interface $n_i \to n_j$

$$t_{p,i\to j} = \frac{2n_i \cos\left(\theta_i\right)}{n_j \cos\left(\theta_i\right) + n_i \cos\left(\theta_j\right)} \tag{5.11}$$

References

[1] E. Betzig, G. H. Patterson, R. Sougrat, O. W. Lindwasser, S. Olenych, J. S. Bonifacino, M. W. Davidson, J. Lippincott-Schwartz, and H. F. Hess, *Imaging intracellular fluorescent proteins at nanometer resolution,* Science **313**, 1642 (2006).

[2] S. T. Hess, T. P. Girirajan, and M. D. Mason, *Ultra-high resolution imaging by fluorescence photoactivation localization microscopy,* Biophys J **91**, 4258 (2006).

[3] M. J. Rust, M. Bates, and X. Zhuang, *Sub-diffraction-limit imaging by stochastic optical reconstruction microscopy (storm),* Nat Methods **3**, 793 (2006).

[4] B. Huang, W. Wang, M. Bates, and X. Zhuang, *Three-dimensional super-resolution imaging by stochastic optical reconstruction microscopy,* Science **319**, 810 (2008).

[5] C. Smith, M. Huisman, M. Siemons, D. Grunwald, and S. Stallinga, *Simultaneous measurement of emission color and 3d position of single molecules,* Opt Express **24**, 4996 (2016).

[6] C. N. Hulleman, R. O. Thorsen, E. Kim, C. Dekker, S. Stallinga, and B. Rieger, *Simultaneous orientation and 3d localization microscopy with a vortex point spread function,* Nat Commun **12**, 5934 (2021).

[7] M. P. Backlund, M. D. Lew, A. S. Backer, S. J. Sahl, G. Grover, A. Agrawal, R. Piestun, and W. E. Moerner, *The double-helix point spread function enables precise and accurate measurement of 3d single-molecule localization and orientation,* Proc SPIE Int Soc Opt Eng **8590**, 85900 (2013).

[8] S. Prasad, *Rotating point spread function via pupil-phase engineering,* Opt. Lett. **38**, 585 (2013).

[9] C. Roider, A. Jesacher, S. Bernet, and M. Ritsch-Marte, *Axial super-localisation using rotating point spread functions shaped by polarisation-dependent phase modulation,* Opt. Express **22**, 4029 (2014).

[10] Y. Shechtman, S. J. Sahl, A. S. Backer, and W. E. Moerner, *Optimal point spread function design for 3d imaging,* Phys Rev Lett **113**, 133902 (2014).

[11] A. Aristov, B. Lelandais, E. Rensen, and C. Zimmer, *Zola-3d allows flexible 3d localization microscopy over an adjustable axial range,* Nat Commun **9**, 2409 (2018).

[12] Y. Li, M. Mund, P. Hoess, J. Deschamps, U. Matti, B. Nijmeijer, V. J. Sabinina, J. Ellenberg, I. Schoen, and J. Ries, *Real-time 3D single-molecule localization using experimental point spread functions,* Nat Methods **15**, 367 (2018).

[13] E. Nehme, D. Freedman, R. Gordon, B. Ferdman, L. E. Weiss, O. Alalouf, T. Naor, R. Orange, T. Michaeli, and Y. Shechtman, *DeepSTORM3D: dense*

3D localization microscopy and PSF design by deep learning, Nat Methods **17**, 734 (2020).

[14] N. Bourg, C. Mayet, G. Dupuis, T. Barroca, P. Bon, S. Lécart, E. Fort, and S. Lévêque-Fort, *Direct optical nanoscopy with axially localized detection,* Nature Photonics **9**, 587 (2015).

[15] C. Cabriel, N. Bourg, P. Jouchet, G. Dupuis, C. Leterrier, A. Baron, M. A. Badet-Denisot, B. Vauzeilles, E. Fort, and S. Lévêque-Fort, *Combining 3D single molecule localization strategies for reproducible bioimaging,* Nat Commun **10**, 1980 (2019).

[16] J. Deschamps, M. Mund, and J. Ries, *3d superresolution microscopy by supercritical angle detection,* Opt Express **22**, 29081 (2014).

[17] P. Kanchanawong, G. Shtengel, A. M. Pasapera, E. B. Ramko, M. W. Davidson, H. F. Hess, and C. M. Waterman, *Nanoscale architecture of integrin-based cell adhesions,* Nature **468**, 580 (2010).

[18] N. Scheefhals and H. D. MacGillavry, *Functional organization of postsynaptic glutamate receptors,* Mol Cell Neurosci **91**, 82 (2018).

[19] M. E. Siemons, N. A. K. Hanemaaijer, M. H. P. Kole, and L. C. Kapitein, *Robust adaptive optics for localization microscopy deep in complex tissue,* Nat Commun **12**, 3407 (2021).

[20] M. A. Thompson, M. D. Lew, M. Badieirostami, and W. E. Moerner, *Localizing and tracking single nanoscale emitters in three dimensions with high spatiotemporal resolution using a double-helix point spread function,* Nano Lett **10**, 211 (2010).

[21] D. Fu, J. J. E. Maris, K. Stanciakova, N. Nikolopoulos, O. van der Heijden, L. D. B. Mandemaker, M. E. Siemons, D. Salas Pastene, L. C. Kapitein, F. T. Rabouw, F. Meirer, and B. M. Weckhuysen, *Unravelling Channel Structure-Diffusivity Relationships in Zeolite ZSM-5 at the Single-Molecule Level,* Angew Chem Int Ed Engl **61**, e202114388 (2022).

[22] B. Huang, S. A. Jones, B. Brandenburg, and X. Zhuang, *Whole-cell 3d storm reveals interactions between cellular structures with nanometer-scale resolution,* Nat Methods **5**, 1047 (2008).

[23] M. J. Mlodzianoski, P. J. Cheng-Hathaway, S. M. Bemiller, T. J. McCray, S. Liu, D. A. Miller, B. T. Lamb, G. E. Landreth, and F. Huang, *Active psf shaping and adaptive optics enable volumetric localization microscopy through brain sections,* Nat Methods **15**, 583 (2018).

[24] H. Heydarian, M. Joosten, A. Przybylski, F. Schueder, R. Jungmann, B. V. Werkhoven, J. Keller-Findeisen, J. Ries, S. Stallinga, M. Bates, and B. Rieger, *3d particle averaging and detection of macromolecular symmetry in localization microscopy,* Nat Commun **12**, 2847 (2021).

[25] Y. Li, Y. L. Wu, P. Hoess, M. Mund, and J. Ries, *Depth-dependent psf calibration and aberration correction for 3d single-molecule localization,* Biomed Opt Express **10**, 2708 (2019).

[26] P. N. Petrov and W. E. Moerner, *Addressing systematic errors in axial distance measurements in single-emitter localization microscopy,* Opt Express **28**, 18616 (2020).

[27] S. Stallinga and B. Rieger, *Accuracy of the gaussian point spread function model in 2d localization microscopy,* Opt Express **18**, 24461 (2010).

[28] R. Berlich and S. Stallinga, *High-order-helix point spread functions for monocular three-dimensional imaging with superior aberration robustness,* Opt Express **26**, 4873 (2018).

[29] S. Ghosh and C. Preza, *Characterization of a three-dimensional double-helix point-spread function for fluorescence microscopy in the presence of spherical aberration,* J Biomed Opt **18**, 036010 (2013).

[30] C. Cabriel, N. Bourg, G. Dupuis, and S. Leveque-Fort, *Aberration-accounting calibration for 3d single-molecule localization microscopy,* Opt Lett **43**, 174 (2018).

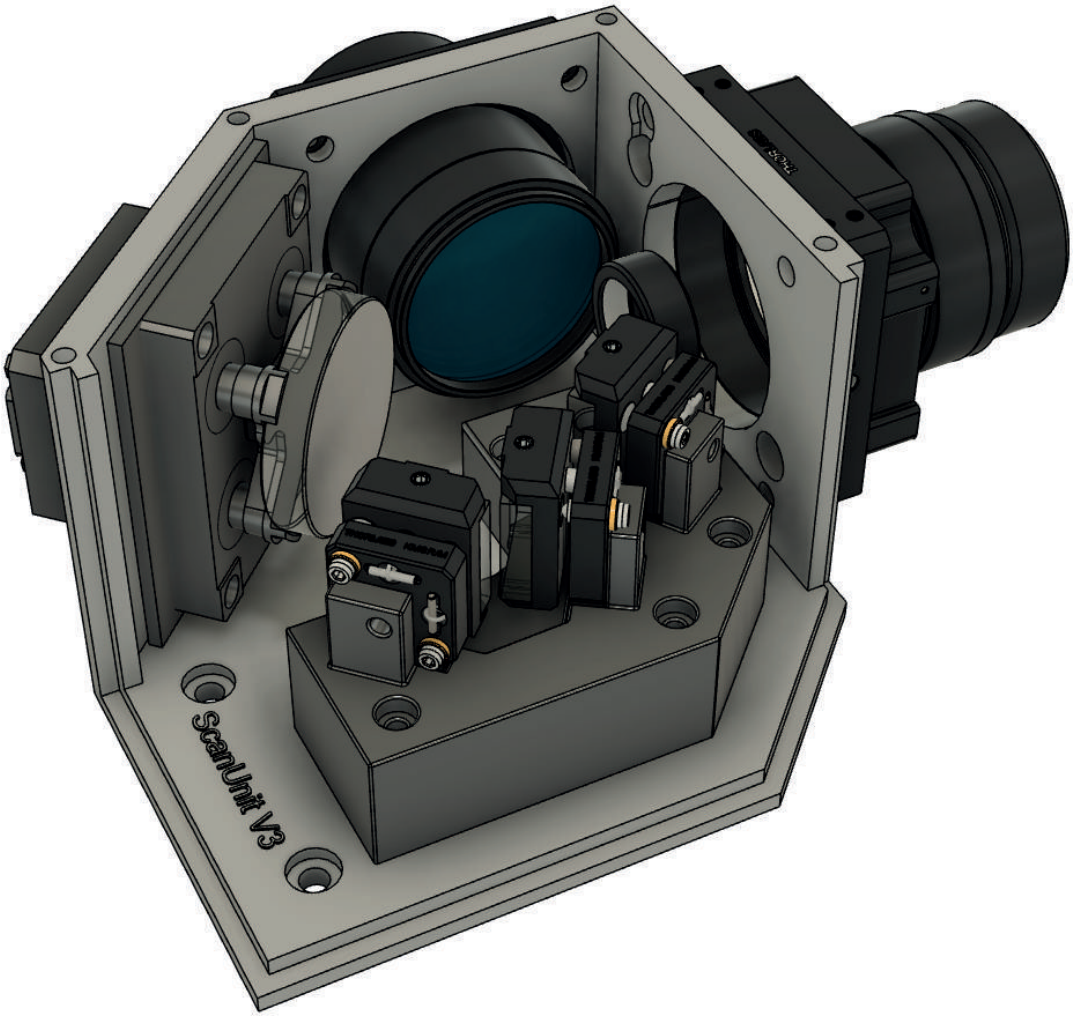
ScanUnit V3

6

Discussion and outlook

6.1 Introduction

In order to understand the cellular mechanisms that underlie the complexity of life, imaging is required to resolve nanoscale interactions and structures. During my PhD, I developed several methods to increase the applicability of Single-Molecule Localization Microscopy (SMLM), an imaging technique that can overcome the diffraction limit. In Chapter 2 and 3 I demonstrated how Adaptive Optics improves imaging inside watery samples and complex tissue such as brain sections. In Chapter 4 I presented an improved implementation for multi-colour SMLM that is easy to implement, insensitive to channel misalignment and photon efficient. Finally, in Chapter 5 I analysed and modelled axial localization accuracy when using PSF engineering for 3D localization.

In this chapter I discuss the work presented in this thesis and present an outlook for SMLM. We first discuss Chapter 2 and 3 on the improvement of Adaptive Optics for SMLM in tissue. We present an alternative method for correcting sample-induced aberrations without AO and discuss whether the signal-to-noise ratio can be improved by reducing the NA of the objective.

6.2 Correcting sample-induced aberrations

Like many microscopy techniques, the performance of SMLM is reduced when imaging inside complex samples and tissue, due to sample-induced aberrations. Sample-induced aberrations can be decomposed into three distinct parts: 1) spherical aberration caused by the general refractive index mismatch between the sample and immersion, 2) complex aberrations caused by mm to μm sized features inside the sample with different refractive indices and 3) scattering caused by structures with a size close to the wavelength of light. To prevent confusion in discussing aberrations and aberration types, we term any form of rotational symmetric aberration that can be described as linear combination of Zernike modes with azimuthal order 0 (Z_2^0, Z_4^0, Z_6^0, etc.) as spherical aberration. We refer to the specific Zernike modes Z_4^0 and Z_6^0 as primary and secondary spherical aberration respectively.

In this thesis we used a deformable mirror to address and compensate aberration causes 1 and 2. In Chapter 2 we compared imaging with AO and without AO in watery samples with a low level of coarse features inside the sample. Therefore the aberration mostly comprised of index mismatched induced spherical aberration. In the absence of AO, this spherical aberration leads to a dramatic loss of astigmatic-induced ellipticy disrupting 3D localization to a point it is no longer useful. AO can reduce the level of spherical aberration, which partially rescues the 3D encoding ellipticy, but requires a tunable astigmatism level to fully restore the astigmatic z-encoding.

In Chapter 3 we developed a method for aberration correction that does not require a fiducial marker, but instead uses the acquisitions of the single-molecules themselves to estimate the aberration. We analysed the performance of previously proposed SMLM AO-methods, both experimentally and with simulations, and concluded that none of these methods resulted in significant or robust correction. By analysing why these correction methods often fail, we developed a new method

termed REALM (Robust and Effective Adaptive optics for Localization Microscopy) that was able to robustly correct sample-induced aberration based on the single-molecule acquisitions.

In order to improve imaging, we mounted the tissue samples in a glycerol-based *d*STORM buffer. This reduced the aberration level in two ways. First, the difference in refractive index between the oil and mounting buffer was reduced, which minimized the refractive index mismatch induced spherical aberration (cause 1). Second, it decreased the amount of scattering because the refractive index difference between subcellular components and the mounting medium was reduced (cause 3). Using REALM and this sample preparation, we were able to perform SMLM through 80 μm slices (sandwich assay) and in 300μm thick stained slices at an imaging depth up to 50 μm. The increase in imaging depth over previous methods allowed us to visualize the membrane periodic scaffold in a functionally identified pyramidal neuron. This demonstrates the feasibility of directly correlating electrophysiological studies to nanoscopic organizations in tissue.

In the case of the sandwich assay, the depth-limiting factor was the working distance of the objective that physically prevented focusing deeper into the sample. When imaging inside stained brain sections, the increase in background level was the depth limiting factor. Therefore both these aspects need to be addressed in order to extend the imaging depth of SMLM.

While both approaches presented in Chapter 2 and 3 appeared to be fruitful, there are other correction or additional methods to improve imaging. First, AO devices are in general difficult to use as they require precise calibration and alignment, and are temperature sensitive. A method for correcting sample-induced aberration that does not require expert knowledge to operate would increase the usability of SMLM in tissue. Second, imaging depth in stained tissue can be enhanced if the signal to background ratio is improved.

6.2.1 Spherical aberration correction by sensor displacement

A deformable mirror is a versatile device capable of correcting primary and secondary spherical aberration and other Zernike modes typically up to the fourth or fifth radial order. AO devices are however difficult to use and require to be flattened upon start-up before every usage. This requires users to have a some knowledge on adaptive optics to use microscopes equipped with AO. In Chapter 3 we observed that spherical aberration is the main aberration when imaging inside tissue. Therefore, if (primary) spherical aberration can be corrected, the imaging performance can be restored to a large extent. As alternative correction approach, spherical aberration can also be introduced by sensor displacement. Such a method would not require any active optical element and does not need be extensively calibrated and characterized. Instead, the sensor position would change accordingly when imaging inside the sample.

The key insight here is that out-of-focus sample planes are imaged by the microscope at different image-planes but with substantial amounts of spherical aberration [1]. This aberration appears because the axial magnification is much larger than the lateral magnification ($M_{\text{axial}} = M^2_{\text{lateral}}/n_{\text{imm}}$). The object is therefore axially

stretched in image space resulting in spherical aberration. However, this spherical aberration can also be used to correct the aberration induced by the refractive index mismatch. In this case, the sensor and objective need to be positioned such that the aberration profile is minimized at a certain imaging depth.

Here we perform an analysis to assess whether such a strategy is feasible and to which extent refractive index mismatch-induced spherical aberration can be corrected. The aberration profile W can be described in normalized pupil coordinates 4ρ as

$$W(\rho) = z_{\text{depth}}\sqrt{n_{\text{med}}^2 - \text{NA}^2\rho^2} + z_{\text{obj}}\sqrt{n_{\text{imm}}^2 - \text{NA}^2\rho^2} + z_{\text{sensor}}\frac{\text{NA}^2\rho^2}{2M^2} \tag{6.1}$$

with z_{depth} the imaging depth from the coverslip, z_{obj} the z-position of the objective, z_{sensor} the sensor displacement, $n_{\text{med/imm}}$ the refractive index of the medium or immersion oil.

For a given imaging depth z_{depth} we need to find the objective position and sensor displacement that together minimize the RMS of the wavefront. Here we adopted the analyses and notation presented in Chapter 5 of the dissertation of Dr. Shakeri [2] and introduced the sensor displacement as optimization parameter. The aberration profile can be compactly notated as

$$W(\rho) = \sum_{i=1}^{3} z_i f_i(\rho) \tag{6.2}$$

with $z_1 = z_{\text{depth}}$ the imaging depth from the coverslip, $z_2 = z_{\text{obj}}$ the objective position and $z_3 = z_{\text{sensor}}$ the sensor displacement and

$$f_1(\rho) = \sqrt{n_{\text{med}}^2 - \text{NA}^2\rho^2} \tag{6.3}$$

$$f_2(\rho) = \sqrt{n_{\text{imm}}^2 - \text{NA}^2\rho^2} \tag{6.4}$$

$$f_3(\rho) = \frac{\text{NA}^2\rho^2}{2M^2} \tag{6.5}$$

The optimal axial positions can be found by minimizing the RMS value of the aberration, which is given by

$$W_{\text{rms}}^2 = \sum_{j,l=1}^{3} g_{j,l} z_j z_l \tag{6.6}$$

with

$$g_{j,l} = \left\langle f_j(\rho) f_l(\rho) \right\rangle - \left\langle f_j(\rho) \right\rangle \left\langle f_l(\rho) \right\rangle \tag{6.7}$$

where the angular brackets denote the averaging over the pupil. The optimal combination of objective and sensor position can be found by solving

$$\frac{dW_{\text{rms}}^2}{dz_2} = 0 \tag{6.8}$$

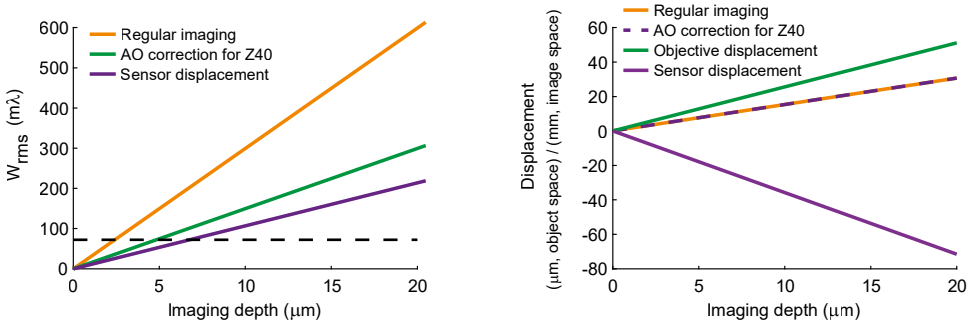

Figure 6.2.1: a) Simulated aberration level (W_{rms}) induced by refractive index mismatch as function of imaging depth for regular imaging, AO correction for Z_4^0 and correction by sensor displacement. Simulation parameters: NA = 1.3, $\lambda = 700$ nm, $n_{\text{med}} = 1.33$, $n_{\text{imm}} = 1.5$ and M = 60X. b) position of the objective in object space and sensor position in image space of (a). Dashed line indicates diffraction limited imaging (72 mλ).

and

$$\frac{dW_{\text{rms}}^2}{dz_3} = 0 \tag{6.9}$$

This system of equations results after some algebraic manipulation in

$$z_2 = \frac{g_{13}g_{23} - g_{12}g_{33}}{g_{22}g_{33} - g_{23}^2} z_1 \tag{6.10}$$

and

$$z_3 = \frac{g_{12}g_{23} - g_{12}g_{22}}{g_{22}g_{33} - g_{23}^2} z_1 \tag{6.11}$$

A similar analysis can be performed to find optimal combinations of objective position and induced primary spherical aberration. This is achieved by using

$$f_3(\rho) = Z_6^0(\rho) = \sqrt{5}\,(6\rho^4 - 6\rho^2 + 1) \tag{6.12}$$

In this case z_3 denotes the optimal amplitude of primary spherical aberration induced by the AO device.

Figure 6.2.1a shows the optimal objective and sensor positions in the case of regular imaging, imaging with AO correcting primary spherical aberration and aberration correction by sensor displacement. For the parameters chosen in this simulation ($n_{\text{imm}} = 1.5$, $n_{\text{med}} = 1.33$, NA $= 1.3$, $\lambda = 700$ nm, M = 60X) the movement of the sensor in image space is 3 orders of magnitude larger than the movement in object space. This analyses reveals that the sensor needs to be displaced by 7 cm to image at a depth of 20 μm, which is a feasible amount that can be physically achieved.

Strikingly, the aberration level as function of imaging depth using over-focusing and sensor displacement is a factor 2 lower than regular imaging and even outperforms AO in correcting primary spherical aberration (see Figure 6.2.1b). This simple, yet effective method is therefore able to substantially correct the main aberration without any active optical element.

This analysis shows that sensor displacement is a feasible approach that is able to effectively reduce refractive index mismatch induced spherical aberration. However this method also suffers from loss of ellipticy as discussed in Chapter 2 when performing 3D astigmatic SMLM, but lacks the capability to adaptively change the astigmatism level. Therefore this method is a potential cheap and convenient solution for 2D SMLM in tissue or other complex samples. Alternatively, this approach can be used in combination with a double-helix PSF for 3D encoding, as this PSF appears to be relatively insensitive to spherical aberration as discussed in Chapter 5 and in more detail by Ghosh et al. [3].

6.2.2 Contrast enhancement by NA reduction

In Chapter 3 we were able to perform SMLM through 80 μm thick brain slices and were limited by the working distance of the objective to image through thicker slices. In these sandwich assays we imaged COS-7 cells stained for microtubules through the unstained aberrating tissue. This effectively mimics some form of optical sectioning. However, when imaging inside 300 μm thick rat brain sections stained for β4-spectrin, we found that we were able to perform SMLM up to a depth of 50 μm. Beyond this depth we observed a significant increase in background level that prevented us from performing SMLM and AO. This is striking because β4-spectrin is not an abundant protein in the tissue. There is therefore a need to reduce the background level or enhance the contrast, especially for staining's with more abundant proteins. An important aspect here is scattering.

In the DNA-PAINT experiments and simulations on the performance of AO in Chapter 3 we neglected scattering components in the wave-front as these cannot be corrected by a deformable mirror. However, when imaging deep inside complex tissue, scattering will cause an non-homogeneous attenuation over the pupil. Light collected with large angles has a longer Optical Path Length (OPL) through the tissue and will therefore have a higher chance to scatter. The increase in signal level when using a high collection NA might therefore not be as significant as theoretically expected. However, a high NA objective does collect more background from auto-fluorescence and out of focus fluorophores. To assess whether there is indeed a trade-off between background and signal level, we performed a simulation to model the scattering and pupil attenuation. The path length l through the sample depends on the collection angle θ inside the sample and is given by

$$l(\theta) = \frac{d}{\cos(\theta)} \tag{6.13}$$

with d the imaging depth. Lambert–Beer law states that the scattering causes an exponential decay in intensity. Therefore the intensity as function of pupil coordinate $\rho = n_{\text{imm}} \sin(\theta)$ is given by

$$\frac{I(\rho)}{I_0} = A^2 \exp\left(-\frac{l(\rho)}{L_{\text{scatter}}}\right) \tag{6.14}$$

with $I(\rho))/I_0$ the normalized intensity and $A = 1/\left(1 - \rho^2/n_{\text{imm}}^2\right)^{1/4}$ the aplanatic

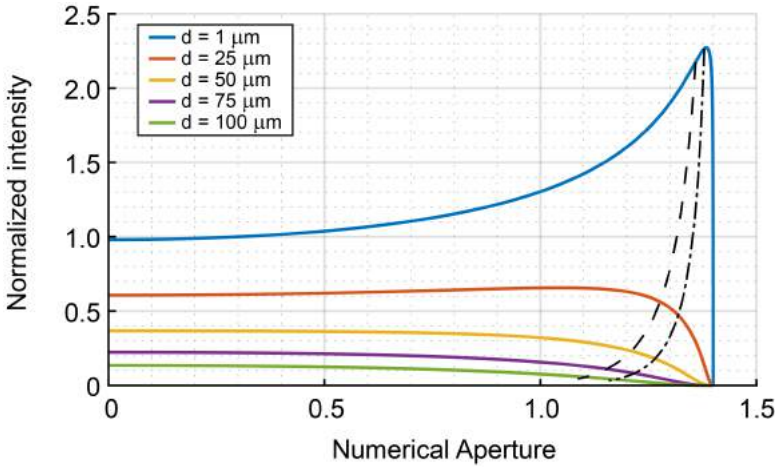

Figure 6.2.2: Pupil apodization for different imaging depths d. Dashed and dash-dotted line indicate NA that contains 90% and 95% of the captured fluorescence at each depth. Simulation parameters: n_{med} = 1.4 and n_{imm} = 1.5.

intensity correction factor. Here we neglected any Fresnel reflection. L_{scatter} is the typical scattering length, which is about 50 μm in brain tissue [4] for blue light.

Figure 6.2.2 shows the apodization in the pupil for different imaging depths. The NA at which 90% or 95% of the fluorescence is collected (dashed and dash-dotted line resp. of Figure 6.2.2) strongly depends on the imaging depth and ranges between 1.35 and 1.1. This simple model estimates a substantial amount of attenuation, which effectively reduces the useful NA. The useful NA is further decreased by the fact that the high NA rays are severely aberrated (ΔOPL > λ) as shown in Chapter 2, Figure 2.3 and will not constructively interfere at the focus.

This analysis reveals that collecting light with angles beyond 1.3 NA will only marginally improve the signal of the single-molecule spot. This is important because high NA objective do have limitations and pitfalls. First, high NA objectives have a shorter working distance that physically prevents imaging deep into the sample. Second, without optical sectioning, a large amount of out-of-focus fluorescence is collected with a high NA objective, which increases the background level. Assuming that the background level scales with the collected light flux ($\sim$ NA^2) [5], increasing the NA from 1.2 to 1.4 leads to a 36% increase in background level while only collecting 10% more signal photons at an imaging depth of 50 μm. We therefore come to the counter-intuitive conclusion that reducing the NA will improve contrast when imaging deep inside tissue.

The optimal NA for imaging inside tissue will likely differ because the background level depends on the sample, imaging depth and staining. A potential method to find this optimum is to use a 4F system at the emission port with an iris placed in the pupil plane. Such a setup would allow to assess the Signal-to-Background Ratio (SBR) for different collection NA's.

6.2.3 Other improvements for SMLM in tissue

Apart from the methods discussed above, there are other possibilities to improve SMLM in tissue. Another approach to reduce the background level is to use light-sheet excitation. An oblique light-sheet with a single-objective would be preferred as a conventional 2 objective light-sheet microscope would not be suited for many sample types. Recent unpublished work from the group of Carlas Smith showed that such an approach improves SBR in thick samples such as monolayers of epithelial cells. To further improve SBR in other tissues, such as brain sections, it is likely that AO is required to shape the light-sheet correctly.

Another potential improvement for SMLM in tissue is the method by which the aberration is obtained. Chapter 3 shows that the aberration level that can be corrected using the acquisition of the blinking molecules themselves is limited to about 1-1.5 rad RMS. Therefore different approaches to measure the aberration are required to image deeper inside tissue. Two alternative methods for this are to create artificial guide stars similar to 2-photon microscopy [6] or use back-scattered light [7]. This would enable a direct measurement of the aberration with either a wave-front sensor or interferometry. This might improve the accuracy of the aberration estimation and increases the aberration level that can be corrected, provided the deformable mirror is able to modulate these higher modes. Based on the explorative imaging we performed inside tissue and the improvements that can still be made, we expect that it is possible to perform SMLM up to depths of 100 μm.

6.3 Multi-color SMLM

Imaging multiple colours or targets is an essential tool for any fluorescence microscopy technique. The multi-colour implementablity of SMLM has been limited for a number of reasons. The fluorophore Alexa647 is one of the best blinking dyes, but spectrally complementary dyes in the green or red channel do not blink as well as Alexa647 [8]. Multiplexed DNA-PAINT can take hours for a single reconstruction and requires components with a short shelf-lifetime [9]. Spectroscopic SMLM [10–13] enables the use of spectrally similar dyes (CF660, CF680 or AF700) but suffers from a reduced signal-to-background ratio and an increase in sparsity constraint. Finally, previous ratio-metric implementations using spectrally similar fluorophores require precise channel registration [14–16] and struggle when using three colors [17].

In Chapter 4 we presented an improved experimental implementation of the Salvaged Fluorescence (SF) concept [18], which is implementable on conversional microscopes. Inspired by the work from Zhang et al. [18] we split the emission using a selection of dichroic mirrors in a short and long wavelength channel but now imaged on a single camera at the emission port. Because the long wavelength channel captures the majority of the emission (>85%) this configuration enables uncompromised detection and localization and does not suffer from chromatic aberrations. We furthermore proposed a new classification algorithm based on a Generalized Likelihood Ratio Test (GLRT) termed Probability-based Fluorophore Classification (PFC) and compared the performance of this method to SF classification and traditional ratio-metric unmixing.

We found that this implementation of the GLRT outperformed traditional ratiometric unmixing, but not the Salvaged Fluorescence approach. This is striking because the Neyman-Pearson lemma states that the GLRT should theoretically be the most powerful level-α test. In this context, the SF classification can also be regarded as a level-α test and therefore PFC should theoretically outperform SF. An explanation for why this is not the case might be that the maximum likelihood estimator (MLE) fit algorithm does not converge properly. However, the GLRT compares the log likelihood of the fit and not the values of the fit parameters. This effect is therefore likely to be small, as long as the obtained local minimum has a value close to the global minimum.

Another explanation for the performance discrepancy between PFC and SF is that the SF algorithm corrects for the background level based on the median pixel value from many acquisitions over a certain time-window. It therefore uses additional information that is not incorporated by PFC. We therefore hypothesize that including background estimation, based on the additional acquisitions, can improve PFC performance.

An alternative test statistic T that uses a separate (pixel wise) background estimate $\hat{\mathrm{bg}}_k$ is given by

$$T = 2\left(\max_{\theta_A} \log L\left\{\theta_A, \eta_1^A, \hat{\mathrm{bg}}_k | d_k\right\} - \max_{\theta_B} \log L\left\{\theta_B, \eta_1^B, \hat{\mathrm{bg}}_k | d_k\right\}\right) \tag{6.15}$$

where $\max_{\theta_A} \log L\left\{\theta_A, \eta_1^A, \hat{\mathrm{bg}}_k | d_k\right\}$ denotes the maximum log likelihood obtained by a 2-channel MLE fit of pixel data d_k with fit parameters θ and fixed intensity fraction η_1 and pixel-wise background estimate $\hat{\mathrm{bg}}_k$. In this implementation the 2-channel MLE algorithm fits 2 Gaussians on top of the (fixed) estimated background. This reduces the number of fit parameters by 2. Additionally, the cross channel alignment and width of the Gaussian can also be removed as fit parameter to improve convergence, leading to a total of 3 fit parameters (x_{pos}, y_{pos}, N_{ph}). Similar to SF, the background can be estimated based on other acquisitions within a certain time window. The temporal median value seems an appropriate estimator assuming blinking is sufficiently sparse.

To test whether this alternative GLRT outperforms SF classification, we performed a simulation study. We modelled the PSF as a 2D Gaussian in each channel with a fixed total number of photons (N_{ph} = 250) and expected channel fractions η_A = 13% and η_B = 3%. Variation in the intensity ratio between spots is incorporated as follows. For each photon we select a random number r that is uniformly distributed between 0 and 1. If $r < \eta$ the photon is assigned to channel 1 and otherwise to channel 2. Together, these random numbers r define the intensities in each channel for this particular spot. Next background is added to the spots ($\mathrm{bg}_{\mathrm{ch1}} = 5$ and $\mathrm{bg}_{\mathrm{ch2}} = 20$) and Poisson noise is added to model shot noise.

In this simulation it is not possible to estimate the background based on other acquisitions. We therefore used the ground truth background level as estimate ($\hat{\mathrm{bg}}_{\mathrm{ch}\lambda} = \mathrm{bg}_{\mathrm{ch}\lambda}$) for both SF and PFC. Additionally we tested if, in the absence of

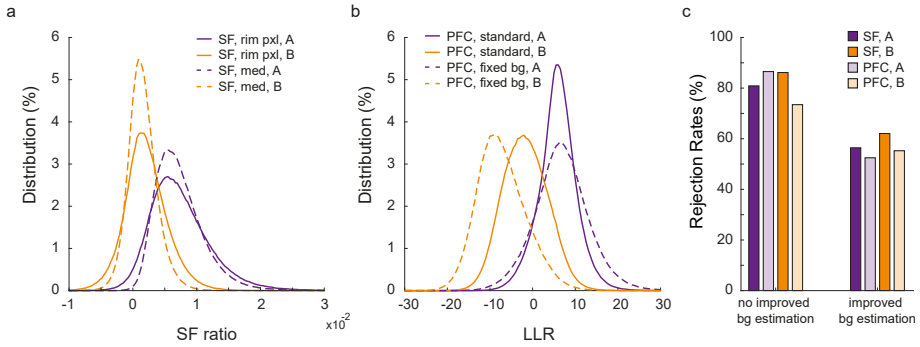

Figure 6.3.1: Comparison between SF and PFC for 1 million simulated spots with a total photon count of 250 and intensity fractions of 13% (fluorophore A) and 3% (fluorophore B). a) Distribution of the SF ratio. SF rim pxl denotes SF with background estimation based on the median of the rim pixels of the spot and SF med denotes SF classification where the ground truth background level is known. b) Distributions of the log likelihood ratio (LLR) test statistic for PFC standard implementation and PFC with fixed background. c) Rejection rates for the distributions of a&b for a false-positive rate of 1%.

the additional acquisitions, SF is able to outperform PFC. In this case a suitable background estimator for SF is the median value of the rim pixels of the region of interest of the spot in channel 1. We therefore test two situations: one where there is no additional information regarding the background and one where it is possible to estimate the background using additional acquisitions. In both cases, PFC should theoretically outperform SF.

We simulated 1 million spots and compared the rejection rates for a 1% false-positive rate for SF with rim pixel and ground truth background correction and PFC as implemented in chapter 4 and this alternative implementation. The results of this simulation are shown in Figure 6.3.1. As expected, the distribution of the SF ratio is less confined when using the rim pixels as background estimation. Interestingly, the LLR distributions are not less confined for the alternative implementation, but seem to shift and become symmetrical around 0. For these particular challenging simulation settings, SF achieves a combined rejection rate of 84% (rim pxl estimate) and 59% (ground truth correction), while PFC achieves a combined rejection rate of 80% and 54% respectively. This simulation reveals that PFC is indeed able to outperform SF when the same amount of information is available. Further analyses on experimental data is needed to support this finding. Nonetheless, in these simulations PFC offered only a minor improvement over SF, indicating that the SF classification algorithm is an effective and suitable classification algorithm.

The experimental implementation as presented in Chapter 4 can be further improved by optimizing the cut-off wavelength of the emission dichroic mirror. There is a significant rejection rate for CF660 and CF680 in the case for 3 colour imaging that hampers reconstruction. A dichroic with a red-shifted cut-off wavelength will introduce a larger intensity ratio difference between CF660 and CF680, which will improve classification. This reduces the intensity available for localization, especially for AF647, but this might be an acceptable compromise. Alternatively, if the

channel-alignment is performed precisely, the intensity in the short wavelength channel can be incorporated into the fitting routine. Finally, PFC is a complementary technique and can be combined with PSF engineering, as shown in Chapter 4, Figure 4.2.3 or other techniques such as SIMFLUX [19] that improve localization precision. For these reason we expect that this experimental implementation combined with PFC or SF classification will become a widely used multi-colour SMLM technique.

6.4 Accurate single-molecule localization

3D localization accuracy is a widely understudied aspect of SMLM, but accurate axial localization is important in many applications. These include multi-plane imaging [20, 21], 3D particle averaging [22], or when the reconstructed volume is used for correlating or modelling of physical forces [23] and processes such as diffusion in neuronal synapses [25]. However, experimental verification is difficult, both laterally and axially, because experimental ground truth data is non-trivial. Therefore, accuracy is often analysed with simulations with extensive PSF models [26, 27]. In the case of axial localization with PSF engineering another complication arises as there is a mismatch between the calibration PSF and the true PSF exhibited by an emitter. The calibration PSF is obtained by acquiring a z-stack of a bead on the coverslip by stage-movement. This movement however imposes a different defocus aberration compared to an emitter with a different position in the mounting medium. Moreover, high NA TIRF objectives capture the Super-critical Angle Fluorescence (SAF), which depends strongly on the absolute distance from the coverslip. This results in a strong z-dependent apodization in the pupil that is not reflected in the calibration PSF.

In Chapter 5 we performed simulations with a vector PSF model to analyse the size of these axial errors caused by model mismatch. These simulations show that using the calibration PSF for localization, results in absolute axial biases of up to 250 nm and relative biases up to 50% over ranges of tenths to hundreds of nanometres. We showed that these biases result from apodization in the pupil due to super-critical angle fluorescence and spherical aberration induced by the mismatch between immersion oil and the mounting medium. To verify the substantial biased predicted by this model, one could use a sample where the axial position can be derived from the lateral position [28]. Alternatively, the axial position can be derived from the ratio between the Under-critical Angle Fluorescence (UAF) and the UAF + SAF [29, 30], while simultaneously recording the engineered PSF in a third channel.

If these findings are indeed experimentally verified, all these effects can in principle be mitigated by fitting the spots directly with this vector PSF model. In other work [31, 32] this vector PSF model showed excellent resemblance with the experimental PSF. This indicates that this model captures indeed most, if not all, aspects of high NA imaging. We hope that this work will contribute to improved 3D SMLM reconstructions and result in improved quantifiable insight into biological processes.

6.5 Outlook

15 years after its invention, Single-Molecule Localization Microscopy has become a reliable and widely used technique to overcome the diffraction limit. In this thesis we addressed several challenges for SMLM to enlarge its applicability domain to tissue and improve multi-colour imaging. Nonetheless, there are still many improvements to be made in the field of SMLM.

6.5.1 Localization precision

Recent developments in SMLM are able to improve the localization precision by shaping the illumination either globally (SIMFLUX) [19, 33–35] or by scanning (MINFLUX) [36]. Here the illumination is correlated to the photons of a blinking event in order to improve the localization precision. These methods can achieve a localization precision as small as 1 nm. While these endeavours are exciting, the biological impact is currently relatively small due to the linkage error in immunostaining. The use of primary and secondary antibodies (AB) in the staining process introduces a significant distance between the targeted epitope and the fluorophore as each AB is roughly 13 nm in size. Combined with the fact that fluorophores can already be routinely localized with a precision below 10 nm this indicates that the impact of SIMFLUX is small for regular SMLM with immunostaining. Therefore SIMFLUX is best applied in combination with dim fluorophores used in (f)PALM [37] often used to track single-molecules in live-cell conditions. Therefore, these setups would require incubators to facilitate live-cell imaging. I furthermore do not expect that the MINFLUX will be a disruptive technology, due to its limited FOV and extreme imaging time, but will be used to aid biological research in specific research questions.

In general, the advancement in SMLM, or other super-resolution microscopy, has come to a point where the linkage error is the limiting factor for the resolution. I expect that there will be a major drive to make nanobodies and other small probes such as aptamers and affimers widely available for research and imaging [38, 39].

6.5.2 Volumetric imaging

Single-Molecule localization microscopy overcomes the diffraction limit by spatial and temporal separation. The individual molecules have to be localized in different frames which restricts the imaging time for a single image plane. Even with PSF engineering, the largest usable z-range per image plane for SMLM is in the order of 2 μm [40]. In order to perform true volumetric imaging, multiple planes have to be imaged and stitched [20, 21]. This requires accurate z-localization, as well as dyes that can blink for a prolonged period of time or use optical sectioning to selectively excite fluorophores. This problem is inherent to SMLM. New techniques might be able to solve this to some extent, but I expect this to remain a pitfall of SMLM. Therefore other 3D super-resolution techniques are more suitable for large volumetric super-resolution imaging, such as Expansion Microscopy (ExM) [41].

Ever since the invention of the microscope, researchers have tried to improve the details that can be resolved inside a sample by improving the optical setup. In 2015 the group of Edward Boyden introduced a new method for super-resolution called

Expansion Microscopy (ExM) [41]. In ExM the sample is stained with fluorescent molecules, which are then embedded in and cross-linked to a swellable hydrogel, after which the cell and its content is digested. The gel is subsequently isotropically expanded, which maintains the relative positions of the fluorophores. Therefore these fluorophores represent the original structure but the distance between them is physically enlarged. It is hard to overstate the elegance of this technique. Expansion Microscopy, sample expansion instead of resolution enhancement, is a paradigm shift after 200 years of microscopy development.

Recent work shows that a 10-fold expansion factor can be reliable achieved [42–44], resulting in a resolution of 25 nm. The gel can also be flipped to combat the non-isotropic resolution of a confocal or STED microscope used to image the gel [45]. ExM can also be combined with SMLM as shown by other recent work [46], which might prove to be a technique with a similar resolution of MINFLUX, but with a higher throughput. Nonetheless, ExM also suffers from the linkage error as a fundamental resolution limit and has other downsides as well. For instance, finding regions of interest is incredibly challenging in these gigantic samples and signal levels are drastically reduced due to the expansion. We expect that ExM will become the go-to microscopy for volumetric super-resolution imaging, but that SMLM and other super-resolution techniques such as STED will remain a reliable and widely used modality.

References

[1] E. J. Botcherby, R. Jvakaitis, M. J. Booth, and T. Wilson, *An optical technique for remote focusing in microscopy,* Optics Communications **281**, 880 (2008).

[2] S. Shakeri, *Whole slide imaging systems for digital pathology*, Ph.D. thesis, Delft University of Technology (2017).

[3] S. Ghosh and C. Preza, *Characterization of a three-dimensional double-helix point-spread function for fluorescence microscopy in the presence of spherical aberration,* J Biomed Opt **18**, 036010 (2013).

[4] G. Yona, N. Meitav, I. Kahn, and S. Shoham, *Realistic numerical and analytical modeling of light scattering in brain tissue for optogenetic applications(1,2,3),* eNeuro **3** (2016), 10.1523/ENEURO.0059-15.2015.

[5] U. Kubitscheck, *Fluorescence microscopy : from principles to biological applications*, second edition. ed., p. 1 online resource (507 pages).

[6] R. Aviles-Espinosa, J. Andilla, R. Porcar-Guezenec, O. E. Olarte, M. Nieto, X. Levecq, D. Artigas, and P. Loza-Alvarez, *Measurement and correction of in vivo sample aberrations employing a nonlinear guide-star in two-photon excited fluorescence microscopy,* Biomed. Opt. Express **2**, 3135 (2011).

[7] S. Park, Y. Jo, M. Kang, J. H. Hong, S. Ko, S. Kim, S. Park, H.-C. Park, S.-H. Shim, and W. Choi, *Restoring single-molecule localizations with wavefront*

sensing adaptive optics for deep-tissue super-resolution imaging, bioRxiv (2021), 10.1101/2021.11.18.469175, .

[8] G. T. Dempsey, J. C. Vaughan, K. H. Chen, M. Bates, and X. Zhuang, *Evaluation of fluorophores for optimal performance in localization-based super-resolution imaging,* Nat Methods **8**, 1027 (2011).

[9] R. Jungmann, M. S. Avendano, J. B. Woehrstein, M. Dai, W. M. Shih, and P. Yin, *Multiplexed 3d cellular super-resolution imaging with dna-paint and exchange-paint,* Nat Methods **11**, 313 (2014).

[10] M. N. Bongiovanni, J. Godet, M. H. Horrocks, L. Tosatto, A. R. Carr, D. C. Wirthensohn, R. T. Ranasinghe, J. E. Lee, A. Ponjavic, J. V. Fritz, C. M. Dobson, D. Klenerman, and S. F. Lee, *Multi-dimensional super-resolution imaging enables surface hydrophobicity mapping,* Nat Commun **7**, 13544 (2016).

[11] M. J. Mlodzianoski, N. M. Curthoys, M. S. Gunewardene, S. Carter, and S. T. Hess, *Super-resolution imaging of molecular emission spectra and single molecule spectral fluctuations,* PLoS One **11**, e0147506 (2016).

[12] Z. Zhang, S. J. Kenny, M. Hauser, W. Li, and K. Xu, *Ultrahigh-throughput single-molecule spectroscopy and spectrally resolved super-resolution microscopy,* Nat Methods **12**, 935 (2015).

[13] C. Smith, M. Huisman, M. Siemons, D. Grunwald, and S. Stallinga, *Simultaneous measurement of emission color and 3d position of single molecules,* Opt Express **24**, 4996 (2016).

[14] D. Baddeley, D. Crossman, S. Rossberger, J. E. Cheyne, J. M. Montgomery, I. D. Jayasinghe, C. Cremer, M. B. Cannell, and C. Soeller, *4d super-resolution microscopy with conventional fluorophores and single wavelength excitation in optically thick cells and tissues,* PLoS One **6**, e20645 (2011).

[15] A. Lampe, V. Haucke, S. J. Sigrist, M. Heilemann, and J. Schmoranzer, *Multi-colour direct storm with red emitting carbocyanines,* Biol Cell **104**, 229 (2012).

[16] C. M. Winterflood, E. Platonova, D. Albrecht, and H. Ewers, *Dual-color 3d superresolution microscopy by combined spectral-demixing and biplane imaging,* Biophys J **109**, 3 (2015).

[17] E. Favuzzi, A. Marques-Smith, R. Deogracias, C. M. Winterflood, A. Sanchez-Aguilera, L. Mantoan, P. Maeso, C. Fernandes, H. Ewers, and B. Rico, *Activity-dependent gating of parvalbumin interneuron function by the perineuronal net protein brevican,* Neuron **95**, 639 (2017).

[18] Y. Zhang, L. K. Schroeder, M. D. Lessard, P. Kidd, J. Chung, Y. Song, L. Benedetti, Y. Li, J. Ries, J. B. Grimm, L. D. Lavis, P. De Camilli, J. E. Rothman, D. Baddeley, and J. Bewersdorf, *Nanoscale subcellular architecture revealed by multicolor three-dimensional salvaged fluorescence imaging,* Nat Methods **17**, 225 (2020).

[19] J. Cnossen, T. Hinsdale, R. O. Thorsen, M. Siemons, F. Schueder, R. Jungmann, C. S. Smith, B. Rieger, and S. Stallinga, *Localization microscopy at doubled precision with patterned illumination,* Nat Methods **17**, 59 (2020).

[20] B. Huang, S. A. Jones, B. Brandenburg, and X. Zhuang, *Whole-cell 3d storm reveals interactions between cellular structures with nanometer-scale resolution,* Nat Methods **5**, 1047 (2008).

[21] M. J. Mlodzianoski, P. J. Cheng-Hathaway, S. M. Bemiller, T. J. McCray, S. Liu, D. A. Miller, B. T. Lamb, G. E. Landreth, and F. Huang, *Active psf shaping and adaptive optics enable volumetric localization microscopy through brain sections,* Nat Methods **15**, 583 (2018).

[22] H. Heydarian, M. Joosten, A. Przybylski, F. Schueder, R. Jungmann, B. V. Werkhoven, J. Keller-Findeisen, J. Ries, S. Stallinga, M. Bates, and B. Rieger, *3d particle averaging and detection of macromolecular symmetry in localization microscopy,* Nat Commun **12**, 2847 (2021).

[23] P. Kanchanawong, G. Shtengel, A. M. Pasapera, E. B. Ramko, M. W. Davidson, H. F. Hess, and C. M. Waterman, *Nanoscale architecture of integrin-based cell adhesions,* Nature **468**, 580 (2010).

[24] M. E. Siemons, N. A. K. Hanemaaijer, M. H. P. Kole, and L. C. Kapitein, *Robust adaptive optics for localization microscopy deep in complex tissue,* Nat Commun **12**, 3407 (2021).

[25] N. Scheefhals and H. D. MacGillavry, *Functional organization of postsynaptic glutamate receptors,* Mol Cell Neurosci **91**, 82 (2018).

[26] S. Stallinga and B. Rieger, *Accuracy of the gaussian point spread function model in 2d localization microscopy,* Opt Express **18**, 24461 (2010).

[27] M. P. Backlund, M. D. Lew, A. S. Backer, S. J. Sahl, G. Grover, A. Agrawal, R. Piestun, and W. E. Moerner, *The double-helix point spread function enables precise and accurate measurement of 3d single-molecule localization and orientation,* Proc SPIE Int Soc Opt Eng **8590**, 85900 (2013).

[28] C. Cabriel, N. Bourg, G. Dupuis, and S. Leveque-Fort, *Aberration-accounting calibration for 3d single-molecule localization microscopy,* Opt Lett **43**, 174 (2018).

[29] J. Deschamps, M. Mund, and J. Ries, *3d superresolution microscopy by supercritical angle detection,* Opt Express **22**, 29081 (2014).

[30] N. Bourg, C. Mayet, G. Dupuis, T. Barroca, P. Bon, S. Lécart, E. Fort, and S. Lévêque-Fort, *Direct optical nanoscopy with axially localized detection,* Nature Photonics **9**, 587 (2015).

[31] M. Siemons, C. N. Hulleman, R. O. Thorsen, C. S. Smith, and S. Stallinga, *High precision wavefront control in point spread function engineering for single emitter localization,* Opt Express **26**, 8397 (2018).

[32] C. N. Hulleman, R. O. Thorsen, E. Kim, C. Dekker, S. Stallinga, and B. Rieger, *Simultaneous orientation and 3d localization microscopy with a vortex point spread function,* Nat Commun **12**, 5934 (2021).

[33] L. Reymond, J. Ziegler, C. Knapp, F. C. Wang, T. Huser, V. Ruprecht, and S. Wieser, *Simple: Structured illumination based point localization estimator with enhanced precision,* Opt Express **27**, 24578 (2019).

[34] L. Gu, Y. Li, S. Zhang, Y. Xue, W. Li, D. Li, T. Xu, and W. Ji, *Molecular resolution imaging by repetitive optical selective exposure,* Nat Methods **16**, 1114 (2019).

[35] P. Jouchet, C. Cabriel, N. Bourg, M. Bardou, C. Poüs, E. Fort, and S. Lévêque-Fort, *Nanometric axial localization of single fluorescent molecules with modulated excitation,* Nature Photonics **15**, 297 (2021).

[36] F. Balzarotti, Y. Eilers, K. C. Gwosch, A. H. Gynna, V. Westphal, F. D. Stefani, J. Elf, and S. W. Hell, *Nanometer resolution imaging and tracking of fluorescent molecules with minimal photon fluxes,* Science **355**, 606 (2017).

[37] S. T. Hess, T. P. Girirajan, and M. D. Mason, *Ultra-high resolution imaging by fluorescence photoactivation localization microscopy,* Biophys J **91**, 4258 (2006).

[38] M. Mikhaylova, B. M. Cloin, K. Finan, R. van den Berg, J. Teeuw, M. M. Kijanka, M. Sokolowski, E. A. Katrukha, M. Maidorn, F. Opazo, S. Moutel, M. Vantard, F. Perez, P. M. van Bergen en Henegouwen, C. C. Hoogenraad, H. Ewers, and L. C. Kapitein, *Resolving bundled microtubules using anti-tubulin nanobodies,* Nat Commun **6**, 7933 (2015).

[39] S. Liu, P. Hoess, and J. Ries, *Super-Resolution Microscopy for Structural Cell Biology,* Annu Rev Biophys (2022).

[40] A. Aristov, B. Lelandais, E. Rensen, and C. Zimmer, *Zola-3d allows flexible 3d localization microscopy over an adjustable axial range,* Nat Commun **9**, 2409 (2018).

[41] F. Chen, P. W. Tillberg, and E. S. Boyden, *Optical imaging. expansion microscopy,* Science **347**, 543 (2015).

[42] S. Truckenbrodt, M. Maidorn, D. Crzan, H. Wildhagen, S. Kabatas, and S. O. Rizzoli, *X10 expansion microscopy enables 25-nm resolution on conventional microscopes,* EMBO Rep **19** (2018), 10.15252/embr.201845836.

[43] S. Truckenbrodt, C. Sommer, S. O. Rizzoli, and J. G. Danzl, *A practical guide to optimization in x10 expansion microscopy,* Nat Protoc **14**, 832 (2019).

[44] H. G. Damstra, B. Mohar, M. Eddison, A. Akhmanova, L. C. Kapitein, and P. W. Tillberg, *Visualizing cellular and tissue ultrastructure using ten-fold robust expansion microscopy (trex),* bioRxiv , 2021.02.03.428837 (2021).

[45] E. A. Katrukha, D. Jurriens, D. M. Salas Pastene, and L. C. Kapitein, *Quantitative mapping of dense microtubule arrays in mammalian neurons,* Elife **10** (2021), 10.7554/eLife.67925.

[46] F. U. Zwettler, S. Reinhard, D. Gambarotto, T. D. M. Bell, V. Hamel, P. Guichard, and M. Sauer, *Molecular resolution imaging by post-labeling expansion single-molecule localization microscopy (ex-smlm),* Nat Commun **11**, 3388 (2020).

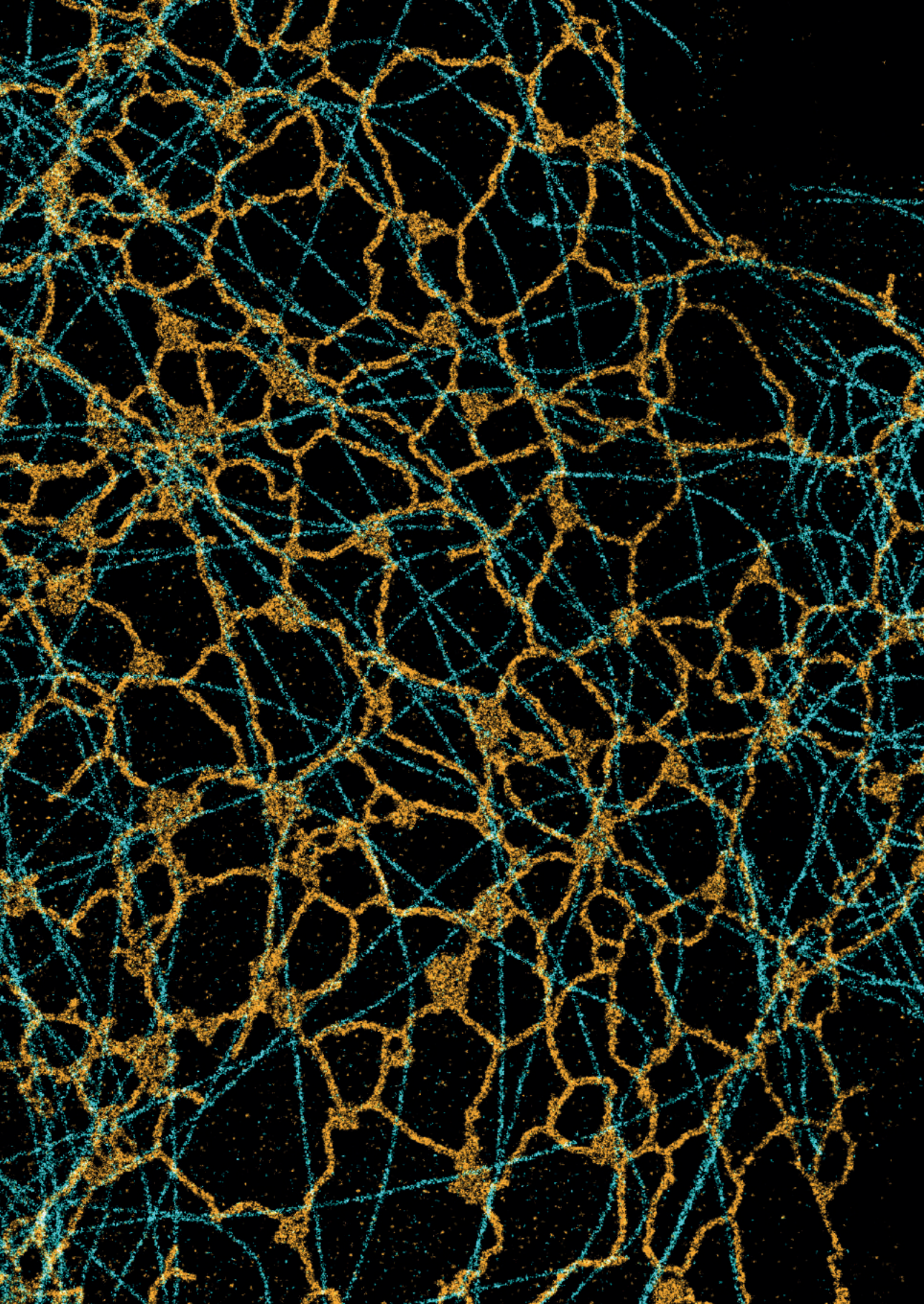

Samenvatting

Lichtmicroscopie is een veelgebruikte techniek om de cellulaire bouwstenen van het leven te ontrafelen. De details die te onderscheiden zijn met standaardtechnieken zijn echter gelimiteerd door diffractie. Hierdoor kan de onderliggende organisatie van een cel, op de schaal van eiwitten, niet worden gevisualiseerd. Lokalisatiemicroscopie is een techniek waarbij de positie van individuele moleculen met een precisie van enkele nanometers kan worden bepaald. Deze methode is afhankelijk van het laten knipperen van individuele fluorescente moleculen. Door deze knipperingen te filmen en samen te voegen tot een enkel beeld, kunnen kleinere structuren worden onderscheiden dan mogelijk is met standaard fluorescentiemicroscopie.

Deze recente ontwikkelde techniek heeft geleid tot verschillende doorbraken in het celbiologisch onderzoek, maar kan niet direct worden toegepast in weefsel of andere dikkere preparaten. Dit komt doordat het uitgezonden licht wordt verstoord door het weefsel, wat de detectie en lokalisatie verslechtert. Deze optische verstoring kan worden gecorrigeerd door gebruik te maken van adaptieve optica. Hierbij wordt een vervormbare spiegel in het collectiepad van de microscoop geplaatst. Door vervolgens de spiegel op de juiste manier te vervormen, kan de verstoring gedeeltelijk worden gecorrigeerd. Hiervoor moet wel eerst de verstoring worden achterhaald. Hiervoor zijn verschillende methodes ontwikkeld, maar het is nog onduidelijk wat de beste correctiemethode voor lokalisatiemicroscopie is en onder welke condities deze methodes werken. In dit proefschrift vergelijk ik verschillende adaptieve optica methodes en onderzoek ik welke mate van verbetering haalbaar is met adaptieve optica.

Om de verbetering van adaptieve optica te analyseren, vergelijken we in hoofdstuk 2 de behaalde lokalisatieprecisie met het gebruik van een waterimmersie objectief en een olie-immersie objectief, met en zonder adaptieve optica. Deze analyse laat zien dat het gebruik van olie-immersie in combinatie met adaptieve optica een verbetering in lokalisatieprecisie oplevert in vergelijking met het gebruik van een waterimmersie objectief. Daarnaast vonden we dat de axiale lokalisatie verstoord wordt bij het gebruik van een olie-immersie objectief in waterige preparaten, zoals een gel of een enkele laag cellen. Door gebruik te maken van adaptieve optica kan dit hersteld worden.

De eenvoudigste manier om de optische verstoring te achterhalen is door gebruik te maken van een referentiekraal, een klein plastic fluorescerend balletje. Het plaatsen van een referentiekraal is echter niet mogelijk in complexere preparaten zoals hersencoupes van proefdieren. Een oplossing hiervoor is om de verstoring te achterhalen door middel van de afbeeldingen van de knipperende individuele moleculen. Dit is echter lastig omdat deze afbeeldingen veel ruis bevatten en snel wisselen in intensiteit. Hierdoor zijn traditionele correctie-algoritmes voor adap-

tieve optica in microscopie niet bruikbaar. In hoofdstuk 3 vergelijken we systematisch verschillende voorgestelde algoritmes voor lokalisatiemicroscopie en laten we zien dat deze nauwelijks of geen robuuste verbetering geven. Op basis van de analyse van deze verschillende methodes stellen we een nieuwe correctiemethode voor. We laten experimenteel en met simulaties zien dat deze methode in staat is om verstoringen op een robuuste manier te corrigeren en voor welke signaal-ruisverhoudingen dit het geval is. We demonstreren deze techniek door in gekleurde hersencoupes van ratten het axon initieel segment te visualiseren op een diepte van 50 μm.

Een andere uitdaging voor lokalisatiemicroscopie is de bruikbaarheid voor verschillende kleuren. Veel fluorescente moleculen, welke goed zijn te scheiden op basis van kleur, zijn niet geschikt voor de meest gebruikte techniek van lokalisatiemicroscopie. De moleculen met de juiste knippereigenschappen hebben een vergelijkbare kleur en zijn daarom lastig te scheiden. In hoofdstuk 4 demonstreren we een verbeterde implementatie van een recent voorgestelde scheidingsmethode, die beter implementeerbaar is op conventionele microscopen. Daarnaast vergelijken we verschillende classificatie-algoritmes met een nieuw algoritme gebaseerd op fotonenstatistiek en bespreken we verschillende aspecten om deze classificatie methode te verbeteren.

Een veelgebruikte manier op de axiale (3D) positie van moleculen te schatten is door de puntspreidingsfunctie (PSF) aan te passen. Deze functie beschrijft de vorm van het spotje op de camera van een enkel molecuul. Door de vorm sterk afhankelijk te maken van axiale positie kan de 3D positie van het molecuul worden geschat. De prestatie van verschillende PSFs wordt vaak vergeleken op basis van de lokalisatie precisie die ze behalen. De accuraatheid van de lokalisaties is echter een aspect waar weinig over bekend is. In hoofdstuk 5 simuleren we de fouten die worden gemaakt in gebruikelijke lokalisatie methodes voor verschillende 3D PSFs, door gebruik te maken van een uitgebreid PSF model. Hiervoor introduceren we een theorie waarmee het brandvlak goed kan worden gedefinieerd in gevallen waarbij het nabije elektrisch veld van de fluorescente moleculen interacteert met het dekglaasje. Deze simulaties wijzen op fouten in de axiale positie die kunnen oplopen tot honderden nanometers als hier niet goed of onvoldoende voor wordt gecorrigeerd.

Samenvattend, het onderzoek in dit proefschrift vergroot de bruikbaarheid van lokalisatiemicroscopie in weefselpreparaten en verbetert de mogelijkheid om meerdere structuren te visualiseren met deze techniek.

Curriculum Vitæ

Marijn Siemons was born in November 15, 1992 in Enschede. He obtained his Gymnasium and Technasium high school diploma at the Bonhoeffer College Bruggertstraat in 2010. He then started his bachelor degree in Applied Physics at the Delft University of Technology. He obtained his Propaedeutic Cum Laude in 2011 and subsequently followed the bachelor Honours Track. He did a minor in sailing boat design and concluded his bachelor with a thesis on anisotropic resolution in localization microscopy in 2014. Afterwards, he continued in Delft to obtain his master degree in applied physics. During this time, Marijn specialized in Imaging Physics and Fluid Dynamics. He performed his master project in the Quantitative Imaging group under supervision of Sjoerd Stallinga on point spread function engineering for localization microscopy. He obtained his master degree Cum Laude in 2017 and then started his PhD in Utrecht at the Department of Biology. Here he worked on adaptive optics for single-molecule localization microscopy and oblique-plane light-sheet microscopy. Starting March 2022, he works as an optical instrument scientist at the Netherlands Institute for Space Research (SRON) in Leiden.

List of Publications

7. **M.E. Siemons**, N.A.K. Hanemaaijer, M.H.P. Kole and L.C. Kapitein, "*Robust adaptive optics for localization microscopy deep in complex tissue,*" Nat Commun **12**, 3407 (2021).

6. D. Fu, J.J.E. Maris, K. Stanciakova ,N. Nikolopoulos,O. van der Heijden, L.D.B. Mandemaker, **M.E. Siemons**, D.M Salas, L.C. Kapitein, F.T. Rabouw, F. Meirer, B.M. Weckhuysen, "*Unravelling Channel Structure-Diffusivity Relationships in Zeolite ZSM-5 at the Single-Molecule Level,*" Angew Chem Int Ed Engl. (2021)

5. J. Cnossen, T. Hinsdale, R.Ø.Thorsen, **M.E. Siemons**, F. Schueder, R. Jungmann, C.S. Smith, B. Rieger and S. Stallinga. "*Localization microscopy at doubled precision with patterned illumination.*" Nat Methods **17**, 59–63 (2020)

4. **M.E. Siemons**, B.M.C. Cloin, D.M. Salas, W. Nijenhuis, E.A. Katrukha, and L.C. Kapitein, "*Comparing strategies for deep astigmatism-based single-molecule localization microscopy,*" Biomed. Opt. Express **11**, 735-751 (2020)

3. A. Nagarajan, L.P. Stoevelaar, F. Silvestri, **M.E. Siemons**, V.G. Achanta, S.M.B. Bäumer, and G. Gerini, "*Reflection confocal nanoscopy using a super-oscillatory lens,*" Opt. Express **27**, 20012-20027 (2019)

2. **M.E. Siemons**, C. N. Hulleman, R. Ø. Thorsen, C. S. Smith, and S. Stallinga, "*High precision wavefront control in point spread function engineering for single emitter localization,*" Opt. Express **26**, 8397-8416 (2018)

1. C. Smith, M. Huisman, **M.E. Siemons**, D. Grünwald, and S. Stallinga, "*Simultaneous measurement of emission color and 3D position of single molecules,*" Opt. Express **24**, 4996-5013 (2016)

Dankwoord

De afgelopen 5 jaren waren een goede achtbaan rit. Als enigszins naïeve natuurkundige stapte ik een biologisch avontuur. Hoewel dit kwam met de nodige uitdagingen, ben ik ontzettend dankbaar voor het warme welkom dat ik heb gekregen van iedereen in het departement. Ik heb zo een bijzonder kijkje in cellulair biologisch onderzoek gekregen, iets wat weinig niet-biologen kunnen meemaken. Hier wil ik graag alle mensen bedanken die mijn promotie zo'n gedenkwaardige tijd hebben gemaakt.

Allereerst: Lukas, dankjewel voor de afgelopen jaren. De vrijheid van jouw begeleiding gaf mij mogelijkheid om mijn tijd en energie op mijn eigen manier in te delen en de uitdagingen op te zoeken waar ik ze zag. Jouw lab is een bijzondere mix van techniek ontwikkeling en biologisch onderzoek en je hebt een goede neus voor nieuwe technieken. Ik hoop van harte dat er weer een natuurkundige in jouw lab mag werken aan de nieuwste microscopie technieken. Deze unieke ervaring gun ik iedereen.

Ook wil ik graag iedereen van het Kapitein-lab bedanken voor de leuke en inspirerende tijd. Desiree, thank you for adopting me the first year of my PhD! Your help in the first years getting me started was a joy! Eugene, thank you for your willingness to discuss mathy stuff, programming issues and more. It has been a tremendous help! Roderick, dankjewel alle gezelligheid. Onze legendarische stapavond zal ik nooit vergeten! Anne, jouw rust in de onzekere wetenschappelijke wereld is bewonderenswaardig. Wilco en Klara, dank jullie wel voor het uitleggen van de meest basale biologische zaken en de wederzijdse interesse in mijn problemen! Hugo, dankjewel voor al onze filosofische discussies. Mithila, it was a joy having you as an office mate in the years. Your dedication and perseverance are an inspiration to me! Florian, thank you for picking up to microscopy coarse with such dedication! Fred, thank you for our small whiskey tasting and good luck starting your new lab! Wendy, dankjewel voor alle gezelligheid. Het Kapitein-lab mag blij zijn met zo'n enthousiaste technician. Giel, Emma, Josiah, Marielle and Malina, thank you for all the gezellige mini-borrels, during borrel-deprived times, at your office!

Dan mijn paranimfen Daphne and Jey. Daphne, als mede-lokalisatiemicroscopiefan heb ik de afgelopen paar jaar met heel veel plezier met je gewerkt. Samen hebben we STORM weer volledig op de kaart weten te zetten als super-resolutie techniek! Onze zoektocht naar de perfecte kleuringen en buffers was lang, maar absoluut de moeite waard. Janine, or Jey, as office-mates I've come to know you quickly as an enthousiastic outgoing person who just keeps organizing stuff! I love our boardgame days and I hope we can continue these, even after your move to Delft.

The general openness of the department was incredibly welcoming. I had a

great time during the lunch breaks and other activities such as the lab-outings and parties. Robbelien, Sybren, Dennis, Robin, Nicky, Lisa, Manon, Anna, Wouter, Arthur and everybody else from the department, thank you for this great time! Daarnaast wil ik ook graag Phebe en Bart bedanken voor hun geweldige ondersteuning. Phebe, dankjewel voor het regelen van al mijn bestellingen en het luisteren naar mijn ICT-orderfrustratie. Bart, dankjewel voor je droge humor. Jouw kwaliteit van woordgrap-emails is iets wat ik ten volle aspireer!

Another highlight of my PhD was the NeuroPhotonics consortium. I had so much fun during the scientific parts of our meetings as well as the non-science parts. Corette, Maarten, Harold, Ivo, Allard and Hans, thank you all for the great time and discussions. Lotte, Pegah, Giulia, Jelmer, and Naomi: I thoroughly enjoyed our time together, discussing the PhD live and more. Naomi, ik heb ontzettend genoten van onze samenwerking. Bedankt voor je geweldige inzet, je bereidheid om altijd meer samples te maken en de gezellige tijd achter de microscoop.

I also thoroughly enjoyed the other collaborations during my PhD. Carlas, Jelmer, Shih-Te, Donglong, Erik and Taylor, thank you for the nice discussions, microscopy time and experience sharing! Ook wil ik graag Sjoerd bedanken. Als bachelor en master thesis begeleider heb je een grote invloed gehad op mijn wetenschappelijke denken en carrière. Ook gedurende mijn promotie hadden we regelmatig contact voor puntspreidingsfunctie-advies en ik ben je ontzettend dankbaar dat je deze tijd voor mij vrij hebt kunnen maken.

Graag bedank ik ook een aantal vrienden die mij hebben bijgestaan gedurende mijn promotie. Ava, samen vertrokken we richting Utrecht voor een nieuwe baan en zochten een huis om te delen. Ik heb je zo goed leren kennen en ik heb ontzettend genoten van jouw kookkunsten, datingavonturen en gezelschap. Bij jou is de wereld nooit saai! Leon, jouw doorzettingsvermogen gedurende jouw promotie traject is bewonderingswaardig en o-zo knap dat je het afgemaakt hebt. Ik hoop van harte dat je een leuke baan in Duitsland kan vinden! Peter, jouw PhD-frustraties waren een prachtige nuancering voor mijn eigen problemen. Ook ík hoop dat we onze natuurwetenschappelijke 2-persoonsboekenclub voortzetten! Daarnaast wil ik graag Jelle, Christiaan, Robert en Ellen bedanken. Jullie hebben het gebrek aan natuurkunde- en andere hoge kwaliteitsgrappen ruimschoots weten te compenseren!

Als laatste wil ik graag mijn familie bedanken. Lieve Anneke en Roland, dank jullie wel voor alle steun en vertrouwen om mijn eigen pad uit te zetten. Sebastiaan en Carlijn, dank jullie wel voor de interesse, steun en medeleven. En als laatste, Merle. Jouw haast onuitputtelijke bereidheid om naar mijn problemen te luisteren was een geweldige ondersteuning. Dankjewel dat je mij hebt willen vergezellen in deze achtbaanrit. Nu op naar het volgende avontuur!

Marijn Siemons
Utrecht, april 2022